Surface eddy mixing in the global subtropics

Julius Johannes Marian Busecke

Submitted in partial fulfillment of the
requirements for the degree of
Doctor of Philosophy
in the Graduate School of Arts and Sciences

COLUMBIA UNIVERSITY

2017

ABSTRACT

Surface eddy mixing in the global subtropics

Julius J.M. Busecke

The salinity of the ocean is inherently linked to the global hydrological cycle by net evaporation. The surface salinity, however does not just act like a 'rain gauge', ocean dynamics are vital in shaping the sea surface salinity (SSS) distribution. Here I investigate the effect of unsteady motions on scales of several hundred km and smaller - mesoscale eddies - on the water masses in the saltiest regions of the surface oceans. These water masses are eventually subducted equatorward and contribute to the shallow overturning circulation by transporting surface signals from the subtropics to the tropics, making them important components of the variable climate system.

Towed CTD measurements in March/April 2013 (a component of the NASA SPURS process study) within the North Atlantic SSS maximum (SSS-max) reveal several relatively fresh and warm anomalies, which deviate strongly from climatological conditions. These features introduce a large amount of freshwater into the subtropical region, exceeding the amount introduced by local rain events. The scales and evolution of the features strongly suggest a connection to mesoscale dynamics. This is supported by high-resolution regional model output, which produces an abundance of features that are similar in scale and structure to those observed, confirming the importance of eddy mixing for the near surface salinity budget of the North Atlantic

SSS-max.

Observations from the Aquarius satellite and the Argo array in the global SSS-max revealed marked differences in the mean shape and variability of the SSS-maxima. These results motivated an investigation of the role of eddy mixing in setting the regional characteristics of SSS maxima.

Observed surface velocities from altimetry are used to stir salinity fields in high-resolution idealized model experiments. Using a water mass framework (salinity coordinates) temporal variability in eddy mixing can be quantified, using diagnostics for the total diffusive flux into the SSS-maxima (transformation rate; TFR) as well as the estimated cross-contour diffusivity(effective diffusivity, K_{eff}). Both diagnostics reveal distinct variability in the different ocean basins. In the North Atlantic, both TFR and K_{eff} are dominated by changes in the velocity field while the North Pacific shows high sensitivity of the temporal variability in eddy mixing with respect to the initial conditions used, which represent seasonal/interannual change of the SSS-max shape and position.

This implies that temporal variability of eddy mixing and diffusivities must be taken into account when constructing salinity budgets in these regions. Furthermore, the translation of results from one SSS-max region to the other might not be possible, particularly when considering a changing climate, which might influence the mechanisms responsible for temporal variability differently.

Lastly evidence is presented for large scale diffusivity variability (particularly in the Pacific), connected to large scale climate fluctuations (ENSO). The evidence presented here suggests a significant modulation of surface diffusivities by climate variability, which represents a feedback mechanism not commonly recognized nor included in modern climate simulations.

Contents

List of Figures

Page

List of Tables

Page

ACKNOWLEDGMENTS

This dissertation in many ways presents the culmination of a truly extraordinary phase of my life, none of which would have been possible without my friends, family and colleagues during my time at Lamont/Columbia and in Germany. First and foremost, my unlimited gratitude goes to Arnold Gordon for years of excellent mentorship, patience, generosity and great humor along the way. Without Arnold I would have never come to Columbia in the first place and my approach to scientific research, teaching and making Martinis with sea ice will always be influenced by him. I thank Ryan Abernathey for the tremendous insight into scientific problems and the unwaivering motivation he provided me throughout the later part of my graduate studies. I am indebted to Andreas Thurnherr and Hsien Wang Ou for their insight on my research as members of my advisory committee.

I had a phenomenal time at Lamont, mostly due to the amazing people who I met here: To Sloan, Jesse, Guleed, Sjoerd, Ale, Etienne, Sophia, Laura, Claudia, Bruce, Phil, thank you for the shared coffees, beers, laughs, surfs and much more! You made this adventure of a PhD a wonderful journey.

I owe special thanks to my dear friend Dimitri Galon, who first introduced the word 'oceanography' to me, and thus has to be credited as the origin of my career as a scientist.

I am beyond grateful to my mother and her success in raising me as a single mother, despite the sometimes challenging circumstances. Her lifelong commitment to social causes will forever be an example for me to not only strive for academic achievements but also be a kind, helpful member of the society I live in.

Lastly, and most importantly, thanks to my wife Katharina. I can still not believe we actually made it to this point and I thank you from the bottom of my heart for your support, love and exceptional patience during the last 7 years no matter if in Brooklyn or across the Atlantic Ocean. None of this would have been possible without you!

For Katharina

Chapter 1

Introduction

1.1 Motivation - Sea surface salinity and the global hydrological cycle

Salinity determines, together with pressure and temperature, the density of seawater, thus making it a crucial variable to observe and understand in the global oceans. Historically, compared to the temperature, ocean salinity has remained a vastly undersampled quantity in the global ocean. Figure 1.1) shows the spatial distribution of historical shipboard salinity measurements. Autonomous profiling floats from the Argo program (Roemmich et al., 1999) and recent satellite observations of SSS (Font et al., 2010; Lagerloef et al., 2008; Entekhabi et al., 2010) have significantly increased the global upper ocean salinity observations, also reducing the strong northern hemisphere bias of historical measurements. A comparison of Argo data to historic measurements (roughly corresponding to Figure 1.1) is shown in Figure 1.2.

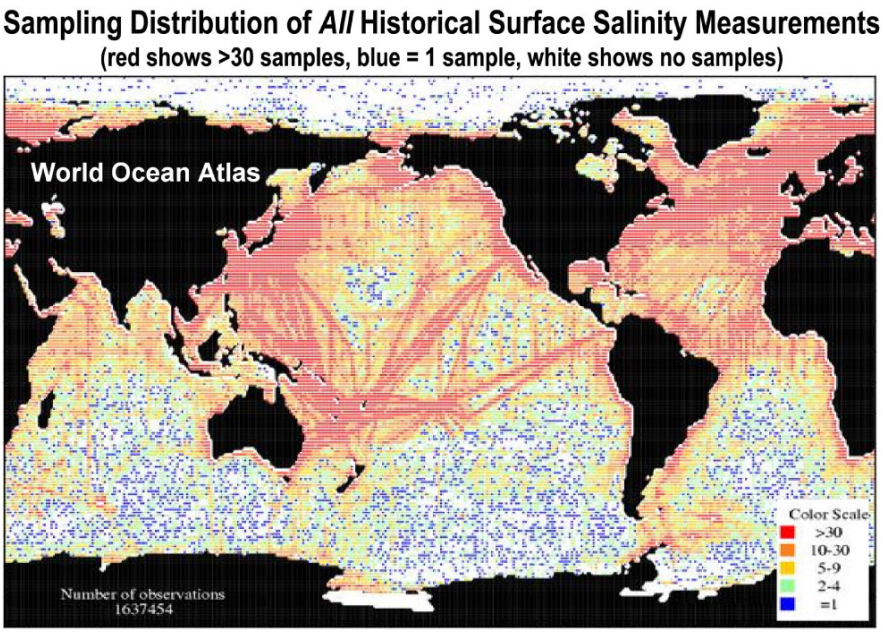

Figure 1.1: This map shows the sampling distribution of historical surface salinity measurements from ships, buoys, etc. Red dots indicate areas that have over 30 measurements, mostly along shipping lanes. Blue dots shows surface areas where only one surface measurement had been taken and white indicates regions with no historical surface salinity measurements. Credit: World Ocean Atlas. Reproduced from `https://aquarius.umaine.edu/cgi/gal_images.htm?id=9`

There are no significant sources of salt in the interior of the ocean, and the total salt content of the global ocean is approximately conserved. No salt leaves the ocean surface, hence local salinity can only be changed by freshwater fluxes at the surface or local convergence of oceanic salinity fluxes. The full full salinity equation can be written as follows:

$$\frac{\partial S}{\partial t} = -\nabla(\mathbf{u}S + \mathbf{D_S}) + F_S \tag{1.1}$$

Here S is the local salinity, $\mathbf{u}$ the full velocity vector and D_S indicates a diffusive (due to molecular diffusion) salt flux vector. The surface salinity

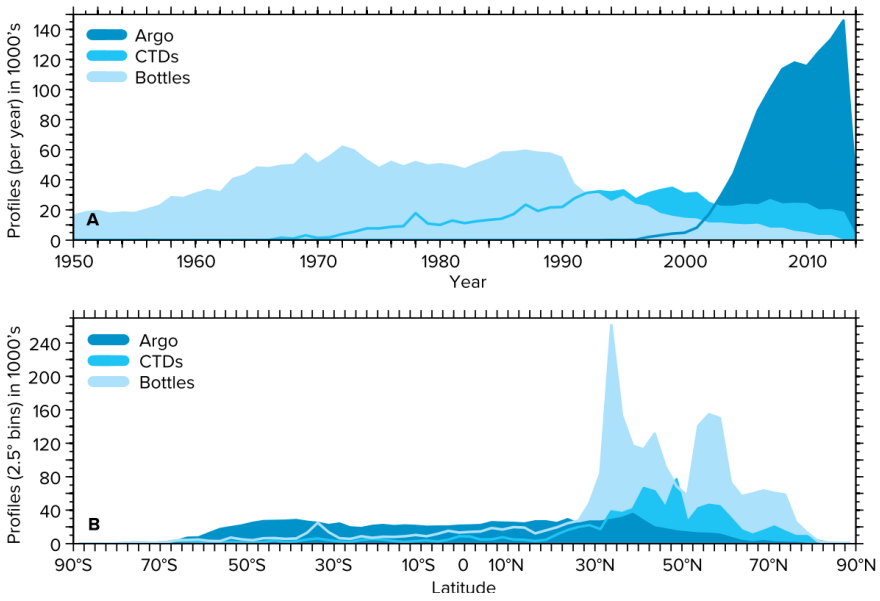

Figure 1.2: Ocean profile data from salinity observing platforms that comprise the World Ocean Database 2013, updated to 2014. Platform type for (A) per year (1950?2014) and (B) in 2.5 deg zonal (latitude) bins for the period 1950?2014. The global nature of Argo program observations is evident in the even distribution of profiles across hemispheres. There is a clear Northern Hemisphere bias in the historical archive comprised of data derived from samples collected in Nansen bottles and by CTDs (instruments that measure conductivity, temperature, and depth). Reproduced from (Durack, 2015)

forcing term F_S arises from the physical constraint of a vanishing salt transport through the air-sea interface. In a surface water parcel, the vertical velocity w at the surface is given by the flux of freshwater

$$w = E - P \tag{1.2}$$

where E is the local Evaporation and P local Precipitation. Near coastal areas (polar regions) river runoff (ice melt) can also be a significant source of freshwater, but since this thesis focuses on open ocean phenomena these terms are assumed to be minor for the rest of the manuscript. Using natural

boundary conditions Huang (1993) at the surface the following condition has to be satisfied:

$$wS - k_s \frac{\partial S}{\partial z} = 0 \tag{1.3}$$

The second term on the left hand side of the equation is a turbulent salinity flux with the vertical diffusivity k_s. Using Equation 1.2 this can be interpreted as a salinity forcing at the surface F_S.

$$F_S = k_s \frac{\partial S}{\partial z} = (E - P)S \tag{1.4}$$

Local maxima in ocean salinity can only be strengthened by F_S. Advection can only redistribute water masses and any diffusive process will act to attenuate local extrema (for a more formal discussion see Section 3.1.1). Ultimately even the surface forcing acting upon the ocean surface is an expression of a redistribution of freshwater, when the atmosphere, cryoshpere and land are considered as a whole. The global exchange between the various reservoirs of water is called the global hydrological cycle and it is very clearly dominated by the ocean. The global ocean contains about 98% of the water in the cycle and 77% of precipitation and 85% of evaporation globally happen over the ocean (Durack, 2015).

Changes in the global precipitation patterns or amounts, associated with climate change (Pachauri et al., 2014), could have profound impacts on agri-

culture, public health and natural disasters (e.g. floods and drought). It is suggested that in order to understand changes in the global hydrological cycle, including the terrestrial part, understanding of the oceanic branch, and the associated changes, is critical (Schmitt, 2008; Durack, 2015).

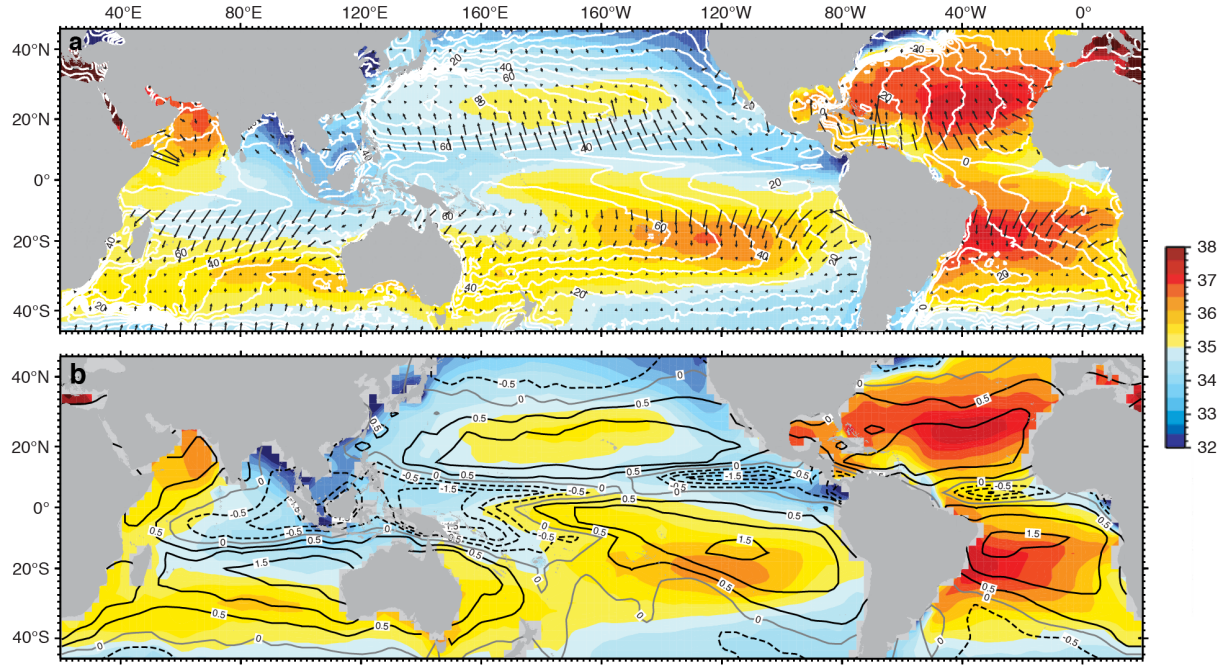

Figure 1.3: (a) Annual average sea surface salinity (SSS) climatology from the Monthly Isopycnal Mixed Layer Ocean Climatology (Schmidtko et al. (2013)) data in color. The white contours show the mean dynamic topography (Maximenko et al., 2009) with a contour interval of 10 cm. The arrows represent the Ekman transport in Sverdrups ($Sv = 10^6 m^3 s^{-1}$), computed using ERA-40 wind stress data (Uppala et al., 2005). (b) Years 2012–2013 mean SSS from Aquarius v3.0 Level 3 bias adjusted data (available via the NASA PO.DAAC portal) in color and evaporation minus precipitation ($E - P$) in m/yr as contours, only plotting the -1.5 to 1.5 range, every 0.5 m/yr, $E > P$ with solid lines. Evaporation data from the WHOI OAFlux Project (`http://oaflux.whoi.edu`) and precipitation from the GPCP v2.2 combined observations and satellite data (NASA's GPCP project at `http://precip.gsfc.nasa.gov`.) Taken from Gordon et al. (2015).

Direct observational estimates of surface fluxes have sparse coverage and global datasets of surface fluxes needed for an estimate of the net evaporation

show large differences, even in the globally integrated values as Schanze et al. (2010) describes. To address these discrepancies the idea of salinity as an 'ocean rain gauge' has been proposed. Schmitt (2008) argues that surface salinity should be used as a primary indicator or changes in E-P rather than relying on the difference between two large terms, each of which has large uncertainties when estimated over the global ocean. He furthermore argues that the impending potential for improved salinity measurements and the remaining uncertainties, especially in evaporation estimates, which rely on sparse observations, would support this idea.

The relationship between SSS maxima (SSS-max) and the freshwater surface fluxes has been pointed out as early as Wüst (1936). And changes of the surface fluxes as a possible mechanism for changes in the surface/subsurface salinity as early as Worthington (1976), who proposed changes in the wind field as explanation for anomalous observations in the near surface salinity. Indeed the sea surface salinity (SSS) distribution seems to align with the field of surface fluxes, where areas of large E-P are roughly collocated with local maxima of SSS and areas of excess precipitation with minima of SSS (Figure 1.3). Despite the overall agreement of zones of high E-P with high salinity, upon closer inspection of the fields, specifically in the subtropics, the peaks of E-P and SSS are not aligned. The SSS-max is generally found polewards of the E-P maximum, pointed out by many studies as evidence for the role of ocean dynamics in shaping the SSS fields (Schmitt, 2008; Gordon

et al., 2015). The poleward shift is usually argued to be caused by the Ekman drift prevalent in all subtropical basins (see Figure 1.3a and Sec. 1.3). This is just one seemingly obvious example of the role ocean circulation plays in shaping the SSS fields. Only when the ocean would be motionless (leaving only molecular diffusion as a balancing mechanism for non-zero E-P), one should expect the SSS-max to align perfectly with the E-P maximum due to the integrating character of the surface salinity. And only then the SSS can be used as a straight forward 'rain gauge'. In reality a detailed knowledge of the ocean dynamics is required if one hopes to recover the net evaporation from the surface SSS at most time scales. Certainly on very short time scales, characteristic for strong rain events, salinity is tightly associated with the precipitation (Boutin et al., 2016). Some studies have also linked multi-decadal changes in SSS trends to an intensification of the water cycle (Durack and Wijffels, 2010; Durack, 2015) but pointed out inconsistencies with climate models about the scaling of an intensification of the water cycle with a global temperature increase. It is suggested that the intensity of the water cycle scales with as the Clausius-Clapeyron (CC) relation, which describes the saturation vapor pressure as a strongly nonlinear function of air temperature. (Durack and Wijffels, 2010) noted, that the amplification diagnosed from observations was stronger than the counterpart from global climate models. A recent study however finds a rate of water cycle intensification, slower than predicted by CC, by investigating the widening of the full

depth salinity distribution (Skliris et al., 2016). This result is in agreement with aforementioned model projections. This emphasizes the importance of considering 3D salinities, or in other words, the importance of ocean dynamics for the ocean salinity, particularly near the surface.

1.1.1 NASA SPURS campaign

The SPURS (Salinity Processes in the Upper Ocean Study, `http://spurs.jpl.nasa.gov`) was a process-oriented measurement campaign in the subtropical North Atlantic (with a second phase being currently carried out in the tropical eastern Pacific). Various in situ measurements were augmented by remote sensing products and regional modeling efforts to investigate processes that affect SSS across a large range of time and space scales. SPURS provided the initial motivation for this thesis and Chapter 2 is mostly based on measurements taken during a cruise as part of SPURS. Other studies from the campaign are summarized in (Lindstrom et al., 2015).

1.1.2 Differences among subtropical surface salinity patterns

Note: The following is a summary of a manuscript published in *Oceanography* (2015), Vol. 28(1), pp. 1–30, `http://dx.doi.org/10.5670/oceanog.2015.02` [1]

[1] AUTHORS: Arnold L.Gordon [a]*, Claudia M. Giulivi [a], Julius Busecke [a], Frederick M. Bingham [b]

[a] Department of Earth and Environmental Sciences and Lamont-Doherty Earth Observatory of Columbia University, 61 Route 9W, Palisades, NY 10964, USA
[b] Center for Marine Science, University of North Carolina Wilmington, Wilmington, North Carolina, USA

* corresponding author: A.G. agordon@ldeo.columbia.edu

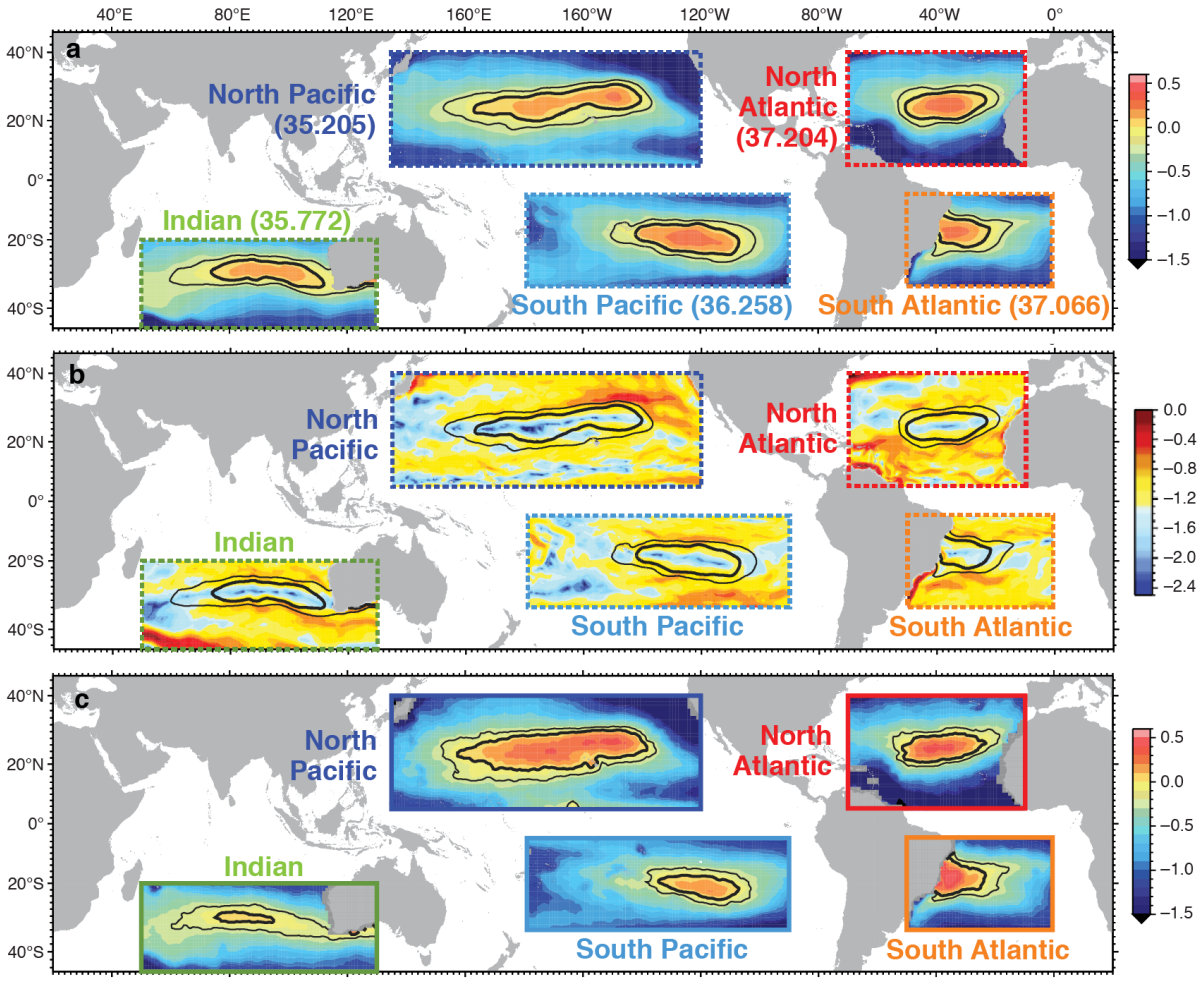

Figure 1.4: Subtropical surface salinity maximum (SSS-max) patterns. (a) Color patterns show the MIMOC climatological SSS anomalies within the five SSS-max subtropical regions. The anomalies are relative to a reference SSS indicated in parenthesis for each of the subtropical regions. The thin and thick contours denote the reference salinity (S-ref) and the –0.2 deviation from it. (b) Magnitude of the MIMOC SSS horizontal gradients (log10). The contours as shown in (a) are included. (c) Aquarius v3.0 Level 3 bias adjusted SSS anomalies for 2012-2013 in color. The contours are the same as in (a) but shown for the Aquarius data. Taken from Gordon et al. (2015).

The subtropical ocean SSS maxima of the North and South Atlantic, the North and South Pacific, and the southern Indian Oceans constitute inte-

grated responses to excess evaporative air-sea freshwater flux and convergence of freshwater by ocean circulation and mixing processes, and they display similarities and differences. The five subtropical regimes all have slightly different "personalities" that likely are consequences of specific land/ocean regional geometries that affect SSS, such as E–P, mean circulation, and vertical and horizontal mixing processes (Vinogradova and Ponte, 2013; Busecke et al., 2014; Gordon and Giulivi, 2014). Figure 1.4 reveals the relative strength and shape of the global SSS-maxima by subtracting a constant reference salinity in each basin.

- North Atlantic: the North Atlantic Ocean is the saltiest of the five subtropical regions. Dry air blowing off the Sahara Desert leads to large freshwater fluxes out of the surface (Schanze et al., 2010) and thus high SSS values. The trade winds export the resultant water vapor across Central America into the tropical Pacific (Zaucker and Broecker, 1992). An additional factor, though not unrelated to the net water vapor export, is the Atlantic Meridional Overturning Circulation (AMOC). Relatively salty water from the South Atlantic is injected into the North Atlantic as a component of the upper limb of the AMOC. The North Atlantic subtropical eastern boundary current, the Canary Current, is notably saltier than those of the other basins because the eastern limb of the North Atlantic subtropical gyre does not advect low-salinity subpolar water toward the equator as occurs in the North-South Pacific and

South Atlantic. Rather, the subpolar region feeds into the lower limb of the AMOC.

- South Atlantic: The South Atlantic SSS-max is located at the western sector of the subtropical belt. This feature is likely a consequence of the AMOC. Most of the South Equatorial Current feeds into the cross-equatorial transport via the North Brazil Current, rather than turning southward into the South Atlantic subtropical western boundary Brazil current, becoming more concentrated in the regional salty subtropical water. The Benguela Current, the eastern boundary current of the South Atlantic subtropics, is fed by Indian Ocean subtropical water, with some inclusion of South Atlantic Current water (Gordon et al., 1992). A mixture of lower salinity Indian Ocean water, the Agulhas leakage, and subpolar water as parts of the South Atlantic Current curl into the Benguela Current (Beal et al., 2011). The SEC advects this water within a broad sweep toward the northwest, feeding into the cross-equatorial flow of the AMOC, "washing away" the SSS-max within the central and eastern subtropical sectors of the South Atlantic.

- North Pacific: It is the freshest of the five SSS-max. The North Pacific has negative E-P due to input of water vapor from the Atlantic across Central America, and Southern Hemisphere water vapor into the ITCZ, near 10N. Low SSS subpolar water is mainly injected into subtropical

latitudes in the eastern boundary California Current, as export into the Arctic via Bering Strait is small $< 1Sv$ (Roach et al., 1995), with the primary export of low salinity North Pacific water into the Indian Ocean within the Indonesian Throughflow.

- South Pacific: Bingham et al. (2014), using ship-based, TAO/TRITON mooring, and Argo data, inspect the seasonality of the North and South Pacific SSS from 60N to 40S. They find that the within the western tropical South Pacific near 15S, the maximum SSS occurs in August/September, whereas more variable timing of the SSS-max occurs in the eastern South Pacific. This is likely a result of the details of the seasonal variability of the precipitation. The South Pacific is the only ocean basin with this kind of variable phase in the relevant latitude band (Bingham et al., 2012).

- Southern Indian: The SSS-max exhibits a broad zonal band and is furthest from the equator. Similar to the western South Pacific, the Australia-Asian monsoon shifts the rainy ITCZ into the Southern Hemisphere during the boreal winter (Wallace and Hobbs, 2006). In addition, low salinity waters of the high precipitation Indonesian seas are injected into the eastern Indian Ocean near 12S with the Indonesian Throughflow (Gordon, 1986); there is also low SSS advected into the region by the South Java Current, drawing water from the Bay of Bengal. The

low SSS water spreads westward within the zonal-flowing South Equatorial Current, forcing the subtropical SSS-max water to reside well to the south of the high E-P band that lies slightly north of 20S. The eastern boundary is relatively salty as low SSS subpolar water is not funneled northward by Australia, blocked by the southward-flowing Leeuwin Current. Additionally, Tasman leakage allows salty subtropical water from the Great Australian Bight to spread into the Indian Ocean (Sebille et al., 2014). The western boundary Agulhas Current injects salty water from the evaporative western Indian Ocean into the southern subtropical belt.

This thesis will investigate one specific mechanism that can influence the SSS and potentially contribute to the observed regional differences - mixing by mesoscale eddies. I will furthermore explore the influence of this process on water masses that are subducted to the subsurface in the shallow overturning circulation.

1.2 Eddy Mixing

Fox-Kemper et al. (2013) provides an excellent review of mesoscale eddy transport in the ocean. I will summarize the most important concepts for this thesis here. Following their terminology, all fluctuations from the mean circulation with time scales of weeks and length scales of several hundred

kilometers (i.e. mesoscale) will be referred to as "eddies."

Eddies play a major role in the global ocean circulation (e.g. Marshall and Speer (2012); Marshall et al. (2017), water mass formation (Groeskamp et al., 2016) and transports of tracers like heat,salt and anthropogenic carbon, in the ocean(Stammer, 1998; McCann et al., 1994; Tréguier et al., 2014; Gnanadesikan et al., 2015). In this thesis I will focus on the effect of eddies on tracer transports in the surface ocean

Unsteady motions in the ocean can be examined by decomposing the Navier-Stokes equation into a mean state and the fluctuations from it $v = \overline{v} + v'$ The primes indicate a deviation from the average (in time, space or both) represented by the over bar. The averaging procedure has to be a Reynolds operator, i.e. the following conditions need to be fulfilled for two random variables Φ and Ψ):

1. $\overline{\overline{(\Phi)}} = \overline{(\Phi)}$
2. $\overline{(\Phi)'} = 0$
3. $\overline{\overline{(\Phi)}(\Psi)} = \overline{(\Phi)}\,\overline{(\Psi)}$

This so called Reynolds decomposition introduces 'Reynolds fluxes' into the tracer conservation equations, which are covariance terms between the velocity and tracer fluctuation about the mean, making the system of equations underdetermined. To solve the system of equations, a closure is necessary, which is commonly assumed to be in the form of diffusion down the mean

gradient. This closure is motivated by Lagrangian particle dispersion which behaves diffusively assuming the decorrelation length of the fluid parcel displacement is small compared to the spatial scale of the tracer gradient.

To evaluate the validity of this assumption a comparison of the mixing length to the curvature scale of the diagnosed tracer field is described in Section B.3.

Additionally a diffusive form of closure is desirable for implementation of parametrizations of eddy effects in numerical models since the expression for the eddy fluxes is based on the mean state (the 'coarse' output of a model).

In the most general form the full eddy flux vector is expressed as the product of a second order tensor $\mathbf{R}$ and the gradient of the mean tracer.

$$\overline{\mathbf{u}'C'} \simeq -\mathbf{R}\nabla\overline{C} \ . \tag{1.5}$$

However, here $\mathbf{R}$ does not have to represent a purely diffusive process, e.g. a symmetric tensor. Any second order tensor can be split up into a symmetric diffusivity tensor ($\mathbf{K}$) and an asymmetric advection tensor. A representation of the full tensor is needed to accurately reproduce the effect (both diffusive and advective) in a coarse resolution model. However, for this thesis we will focus on $\mathbf{K}$, e.g. the diffusive part of the eddy flux. A real and symmetric tensor can be fully described by its (real) eigenvalues and orthogonal eigenvectors. Furthermore the eigenvectors can be chosen as an orthonormal basis of the tensor, called the 'principal axes' of the tensor. The

real and positive eigenvalues then represent a typical diffusivity in the direction of the corresponding principal axis (eigenvector). Results from idealized models (Bachman et al., 2015) and drifter experiments as well as observations (Rypina et al., 2012; Lumpkin and Johnson, 2013) indicate strong anisotropy in the diffusion tensor, often aligned with regions of strong flow. The potential mechanisms causing the anisotropy are summarized in (Fox-Kemper et al., 2013). These regions, e.g the western boundary currents and the ACC, usually show strong lateral gradients across the flow direction. Only when the principal axis is aligned with the gradient of the tracer field the diffusivity can be represented by a scalar. This is also true in anisotropic homogeneous turbulence, where the diffusivity along all principal axes is equal.

An alternative framework for diagnosing only the part of the eddy diffusivity leading to irreversible mixing is based on the 'roughness' of the tracer field. Roughness is enhanced by mesoscale stirring and enhances the small scale lateral gradient on which 'small-scale' diffusion acts (and is amplified by), in turn permanently destroying tracer variance.

This physical concept can be employed using a tracer following coordinate system (e.g. diffusivities are diagnosed along lines of constant tracer concentration) or, with certain restrictions as a local diffusivity with a grid box. The former diagnostic is called 'Effective Diffusivity' (Nakamura, 1996) and used in Chapter 3. The latter diagnostic is the 'Osborn-Cox diffusivity' (Osborn and Cox, 1972), which is used in Chapter 4.

The physical interpretation of the diagnosed mixing processes is very similar: Only the enhanced small scale diffusivity (due to enhanced lateral tracer gradient variance) is diagnosed as a diffusivity, reversible processes are excluded. However, the main difference is that the Osborn-Cox diffusivity is a diagnostic of local destruction of tracer variance by small scale mixing, not able to account for advection of tracer variance, but providing a local estimate of diffusion. The effective diffusivity on the other hand, incorporates non-local effects but provides only an estimate of diffusivity integrated along a tracer contour. As Abernathey and Marshall (2013) points out, the effective diffusivity is equivalent to the Osborn-Cox diffusivity integrated along a tracer contour. Both of these approaches result in a scalar diffusivity relevant for the tracer fields used for diagnosis. This can be understood as a projection of the vector consisting of $\mathbf{K}$ principal axes onto the tracer contour. Using multiple tracers (with different large scale geometries), one can presumably identify the minor axis of the full diffusivity tensor $\mathbf{K}$. The minor axis is of large importance to tracer transport since transport perpendicular to the the direction of flow cannot be accomplished by advection, yet it is important for the transformation of water masses and hence the global circulation. This suggest the relative importance of mixing processes is higher for cross-frontal exchange, usually characterized by the minor principal axis of the diffusivity tensor.

In Chapter 3 the cross frontal diffusivity respective to contours of constant

salinity is used to compare the influence of eddy mixing to the global SSS-maxima. This effectively eliminates the effects of advection from the salinity budget equation, and provides a unique view on mixing effects relevant to water mass transformation. Several studies have documented the spatial heterogeneity of eddy diffusivities from observations(Abernathey and Marshall, 2013; Cole et al., 2015) with significant implications for tracer transport if implemented in numerical models (Gnanadesikan et al., 2015). This thesis will focus in particular on the temporal variability in eddy diffusivities. In Chapter 4 the temporal variability of global eddy diffusivities is investigated. Chapter 3 will investigate the temporal variability in a water mass framework with relevance to the water masses subducted in the shallow overturning circulation.

1.3 The shallow overturning circulation and its role for global climate

The shallow overturning circulation (SOC) is contained in the upper 500 m of the global ocean basins. The mean circulation is characterized by subduction of water masses in the center of the subtropical gyres, which is advected equatorwards. At the equator water is eventually upwelled and returned to the subtropics at the surface due to poleward Ekman drift. In the zonal mean the circulation describes a cell, the so called subtropical cell, but when

following a water particle, the described path in space can be more complex (Schott et al., 2004; O'Connor et al., 2005).

The SOC is associated with large mean volume transports and higher mean tracer gradients than the deeper overturning, resulting in higher heat transports on average (Boccaletti et al., 2005) and presumably also higher salt transports. Due to the higher velocities and smaller extent of the circulation, the residence time is smaller than in the deep overturning cell. These make the SOC important for decadal climate variability.

By connecting the subtropical surface region to the tropical thermocline, spice (density compensated temperature and salinity) anomalies can be transported along isopycnals to the equator where they may feed back to the atmosphere (e.g. Yeager and Large (2007)). In this scenario a change of surface salinity in the subtropics would results in an associated temperature anomaly on a surface of constant density. This anomaly is subducted below the surface layer and advected equatorwards on the isopycnal. Assuming the tropics did not experience a change in the surface fields, the spice anomaly would eventually reach the surface, where the atmosphere would not 'feel' anything of the salinity anomaly. However the temperature anomaly associated might have an impact on the atmospheric circulation, linking changes of the subtropical ocean surface to the tropical atmosphere. This example is clearly a very idealized scenario and further implications, like a change in diapycnal diffusivities are briefly indicated in Chapter 2.

The SSS-max regions are located in the subduction area of the SOC, which can be seen by the subsurface salinity maximum (S-max) formed. Changes observed at the surface, like the increase of SSS-max salinity are propagated below the surface (Durack and Wijffels, 2010). This affirms the importance of the SOC for the propagation of surface signals to the intermediate and deep ocean, e.g. ocean heat content (Roemmich et al., 2015) and possibly anthropogenic carbon (Nakano et al., 2015). Particularly for these active and passive tracer transports, lateral transport by eddy mixing seems very important, as seen e.g. in the differences of anthropogenic carbon uptake when the values used for the isopycnal (lateral at the surface) diffusivity are varied (Gnanadesikan et al., 2015).

1.4 Thesis aims

Chapter 2 presents the first observational evidence for active eddy mixing in the SSS-max of the North Atlantic by documenting high resolution transects through fresh and warm filaments in the center of the North Atlantic SSS-max. These filaments are confirmed to be caused by mesoscale stirring, as indicated by their alignment with geostrophic surface velocities and their water mass characteristics. Filaments of similar structure and intensity are reproduced frequently in a high resolution regional model. A simple eddy diffusivity estimate based on observations confirms the importance of eddy mixing to the surface salinity budget.

Motivated in part by the results described in Sec. 1.1.2 Chapter 3 presents a global study comparing the contribution of eddy mixing to the SSS-max of each basin. SSS fields are stirred with velocities from altimetry observations in an idealized model setup (the MITgcm is used to solve the advection diffusion equation for the passive tracer field supplied.

The total diffusive flux and the integrated diffusivity along a contour of constant salinity is diagnosed. This watermass coordinate system makes results relevant to the subducted subtropical water masses and the SOC. Besides differences in mean contribution to the surface salinity budget, temporal variability in both lateral diffusivity and total diffusive flux can be observed. The robust variability in surface variability, seemingly connected to large scale climate fluctuations in the South Pacific, suggests this phenomenon is extending over a larger scale than the SSS-max.

Chapter 4 moves away from the initial motivation of the SSS and the global hydrological cycle to investigate the global extent and magnitude of a possible forcing of eddy diffusivities by large scale climate fluctuations. This is achieved by using a similar model setup as in Chapter 3 but a different diagnostic to obtain global monthly maps of surface diffusivities. Composites during times of high ENSO index reveal strong enhancements of surface diffusivities covering most of the central and eastern parts of the North and South Pacific basin.

Chapter 2

Subtropical surface layer salinity budget and the role of mesoscale turbulence

Note: This Chapter has been published in *JGR: Oceans* (2014), Vol. 119(7), pp. 4124–4140, http://doi.org/10.1002/2013JC009715 [1]

Abstract

The subtropical North Atlantic exhibits the saltiest surface waters of the open ocean. Eventually that water is isolated from the surface and exported towards the Equator, as a subsurface salinity maximum (S-max) forming the lower limb of the subtropical cell. Climatologically the winter subtropical surface water, coinciding with the deepest mixed layer of $\sim 100\,m$,

[1] AUTHORS: Julius Busecke [a]*, Arnold L.Gordon [a], Zhijin Li [b], Frederick M. Bingham [c], Jordi Font [d]

[a] Department of Earth and Environmental Sciences and Lamont Doherty Earth Observatory of Columbia University, 61 Route 9W, Palisades, NY 10964, USA
[b] Jet Propulsion Laboratory, California Institute of Technology, Pasadena, California, USA
[c] Center for Marine Science, University of North Carolina Wilmington, Wilmington, North Carolina, USA
[d] SMOS Barcelona Expert Centre (SMOS-BEC), Institut de Ciencies del Mar CSIC, Barcelona, Spain

* corresponding author: julius@ldeo.columbia.edu

is saltier and colder than the S-max. Towed CTD measurements in March/April 2013 (a component of the field program SPURS) within the North Atlantic subtropical surface salinity maximum reveal several relatively fresh, warm anomalies, which deviate strongly from climatological conditions. These features introduce a large amount of freshwater into the subtropical region, exceeding the amount introduced by local rain events. Observed scales and evolution of the features strongly suggest a connection to mesoscale dynamics. This is supported by high-resolution regional model output, which produces an abundance of features that are similar in scale and structure to those observed. It is hypothesized that turbulent transport in the surface ocean is a crucial process for setting mixed layer characteristics, which spread into S-max stratum. High variability in the EKE implies a high potential for interannual variability in the resulting S-max water properties by ocean dynamics in addition to the variability caused by air sea fluxes. This has likely consequences to the meridional transport of heat and freshwater of the subtropical cell in the North Atlantic and to the larger scale ocean and climate system.

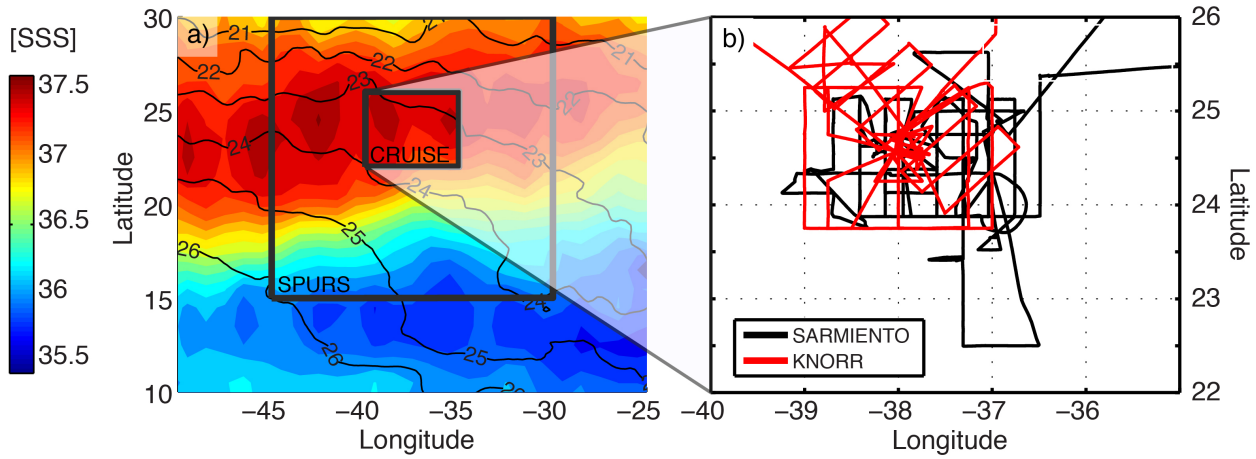

Figure 2.1: a) Sea surface salinity [PSU] from Aquarius L3 (V2) in color and sea surface temperature [$^{\circ}C$] in contours (in black), averaged for March and April 2013. The black boxes indicate the domains used in the text. b) Cruise tracks for the two research vessels utilized in this study. The cruises took place between 2012 and 2013: KNORR (September-October 2012) and SARMIENTO (March-April 2013)

2.1 Introduction

The response of the global freshwater cycle to a changing climate is certainly one of the most pressing questions to answer in order to anticipate and adapt to global climate change (Schmitt, 2008). The ocean is the key element in the global water cycle. It contains about 97% of the Earth's free water and accounts globally for 86% of the evaporation and 78% of the precipitation (Schmitt, 1995). Understanding the marine hydrological cycle is thus crucial to improve the understanding of the global water cycle, including the implications for the terrestrial water cycle. Sea surface salinity (SSS) is an indicator of the marine hydrological cycle, but it is not as straightforward as a rain gauge on land, as advection and mixing (horizontally and vertically) within the ocean can also alter the salinity. To interpret changes in the freshwater cycle using the SSS, it is necessary to understand the underlying ocean processes in order to piece together a full picture of the hydrological cycle in the ocean and its coupling to the atmosphere.

The horizontal SSS maximum (SSS-max) in the subtropical North Atlantic has the highest open-ocean values of SSS in the world. The region of the SSS-max (centered near 25N, 38W; Figure 2.1a) is highly evaporative (Schanze et al., 2010), with evaporation exceeding precipitation ($E - P > 0$) the entire year. To balance this loss, fresher waters have to be advected or mixed both horizontally and vertically into the salty surface layer. Salty surface waters are exported equatorwards below the surface, forming the S-max core near 100-150 m (Worthington, 1976), often referred to as the subtropical underwater (O'Connor et al., 2005). In the tropics wind induced Ekman divergence causes upwelling of the subsurface waters, which are subsequently freshened due to excess rainfall. On average Ekman transport spreads the lower salinity surface water towards the subtropics, closing the shallow overturning cell (Schott et al., 2004). This manuscript will use the equivalent but more widely used term subtropical cell (STC). The STC has been described as a major ocean circulation feature which is important to the poleward heat transport (Boccaletti et al., 2005), and as such is important for the global climate.

The climatological SSS-max is depicted as a region with low lateral gradients of salinity, by data averaging and smoothing procedures (e.g. (Schmitt, 2008) Figure 2.1 b). Using underway data from research and commercial vessels (Reverdin et al., 2007), and now the Aquarius (Bingham et al., 2014) and SMOS (Font et al., 2010) satellites, the SSS field can be observed at much higher resolution than before, revealing far more variability, with a robust seasonal cycle and shifts in position of the SSS-max. Net evaporation and surface salinity are anticorrelated (Gordon and Giulivi, 2014) and the maximum surface salinity is located north of the E-P maximum (e.g. (Schmitt, 2008)), both strong indications of the significant influence of oceanic processes in setting the water properties and controlling the variability of the SSS-max.

The ocean processes responsible for controlling mixed layer properties in the SSS-max and the export of salty surface waters into the S-max layer are the subject of this study, with a focus on the influence of turbulent mesoscale structures in the surface layer that stir freshwater into the region, as observed during the SPURS (Salinity Processes in the Upper Ocean Regional Study; http://spurs.jpl.nasa.gov) field project.

2.2 Data and methods

Most of the data described herein were collected during one of the field expeditions organized within the SPURS project. The measurements were carried out between March 22nd and April 8th on the Spanish research vessel SARMIENTO DE GAMBOA (SPURS-MIDAS cruise, track shown in Figure 2.1b). Additional data sets used in this study are listed below. Throughout the text the CRUISE-domain and SPURS-domain (Figure 2.1a) will be used for spatial reference.

2.2.1 Underway

The underway thermosalinograph (TSG, model SeaBird SBE 21) was located at 2-3 m depth near the bow of the ship, measuring temperature and conductivity in 6-second intervals. The TSG data showed periods of very high variability, which might be caused by several reasons like the shallow intake entraining bubbles due to ship movement, variable flow rates in the seawater system or strong diurnal warming and salinification, leading to strong gradients in the upper meters of the water column, as indicated by other measurements during previous cruises. All data shown are smoothed with a Gaussian window of 20 min length. The salinity calibration was performed by adjusting to water samples drawn from the seawater system. A constant value is fitted to the residuals between the TSG and water samples weighted by the normalized inverse of the variance that was experienced before the sample was taken. This method reduces the error due to uncertainty in the transit time from TSG to the sample station. The estimated constant offset that was determined this way is 0.04 PSU. The temperature data were adjusted by preselecting samples with wind speed $> 8m/s$ and during nighttime, which have been seen to exhibit very small vertical gradients in the upper meters within this region (Fratantoni, personal communication). The temperature was then adjusted downwards by a constant offset such that 99% of the samples are neutral or stably stratified (comparing the TSG and SeaSoar). This yields an offset of 0.59 $°C$. Since the temperature is not determined by a hull sensor, but rather after the water passes through the intake pump, the bias could be due to the influence of the ship and pump, which might vary over time and with the flow rate.

2.2.2 Shipboard Acoustic Doppler Current Profiler (SADCP)

The shipboard instantaneous velocities were recorded by a Teledyne RDI 75 Khz Workhorse Ocean Surveyor. Due to low scatter environments the narrow band mode and a bin size of 16m was chosen (the topmost bin was centered at $\sim 24m$). The data presented in this study was averaged to 2 min intervals.

2.2.3 SeaSoar

The SeaSoar towed sensor system was equipped with dual pumped temperature/conductivity sensors. A final calibration is not available as of now. Initial comparison between sensors yields differences that are at least an order of magnitude lower than the gradients of structures relevant to this study and should not significantly bias our findings. SeaSoar data were averaged on 1-dbar bins and over 10-minute intervals, ensuring that the full cycle from bottom to surface of the SeaSoar is included in every binned profile.

Figure 2.2 shows examples of the along track variability and typical vertical profiles that were recorded by the SeaSoar. There is large variability in potential temperature, salinity and density, representing strong active fronts in the mixed layer, as temperature and salinity are not compensated in density over various regions of the record.

2.2.4 CTD

Additional subsurface data from the KNORR cruise in September/October 2012 are used for a seasonal comparison (see Discussion). 99 CTD profiles were collected in the measurement area (cruise track is shown in Figure 2.1b).

2.2.5 MIMOC climatology

The MIMOC climatology is a gridded seasonal climatology derived primarily from Argo data. It provides monthly profiles on a 0.5x0.5 deg grid (Schmidtko et al., 2013) (V 2.2 on a z-grid was used in this study). The data set is available under http://www.pmel.noaa.gov/mimoc/. Mixed layer depth was determined by a density difference to the surface exceeding $0.1\,kg/m^3$.

2.2.6 TRMM

For the analysis of rain event size in the region TRMM (Tropical Rainfall Measuring Mission) data (product: 3B42, http://mirador.gsfc.nasa.gov), with a spatial resolution of 1/4 degrees

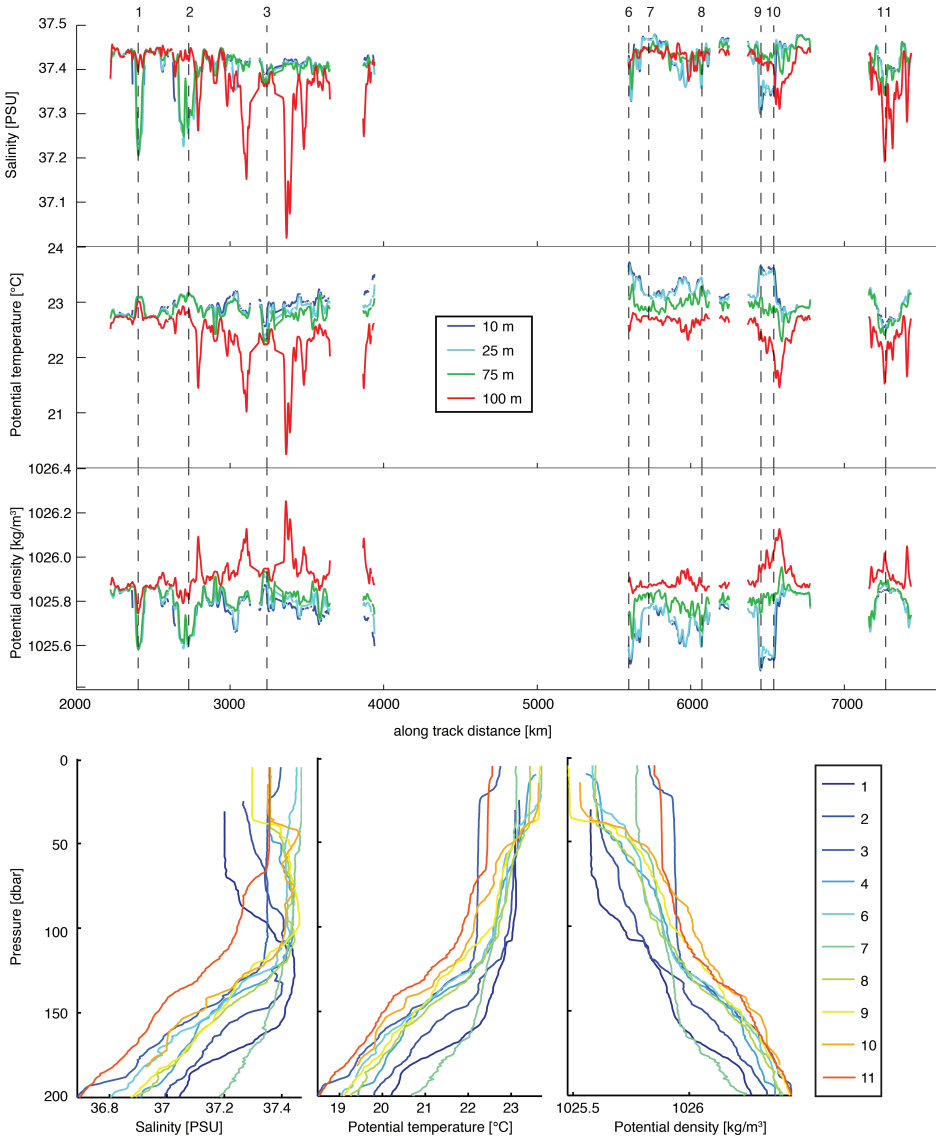

Figure 2.2: SeaSoar data. Upper panel shows along track variations of salinity/potential temperature/density (a Gaussian window of 60 min length is used as a low pass filter for clarity in this figure). Depths are color-coded. Note that large excursions at 100 m depth are confined to that depth and hence represent depth variations of the permanent pycnocline rather then surface variability. The lower panel shows typical profiles of salinity/potential temperature/density with depth (line color corresponds to marker numbers for spatial reference during the survey (see upper panel and other Figures)).

and temporal resolution of 3 hours was used. Connected grid cells of $> 1mm/h$ rain rate within the SPURS area are indexed as individual rain events. The 1 mm threshold is chosen arbitrary, but results derived in this study do not significantly depend on the choice of the threshold value. For each event the rain rate is multiplied by the time resolution and summed over time and space, yielding the total volume of freshwater that enters the ocean. Additionally, the mean rain rate and duration of each event were calculated.

2.2.7 AVISO

For the assessment of the spatial structure of surface velocities AVISO altimeter data is used. The product (dt_upd_global_merged_msla_uv, October 1992-July 2013, http://www.aviso.oceanobs.com) is treated as geostrophic zonal and meridional velocity anomalies u and v with respect to a longterm mean. These are decomposed into $u = \bar{u} + u'$ at each grid point using a 3 month Gaussian window, in order to separate seasonal and longer fluctuations ($\bar{u}$) from the mesoscale signal (u') . The Eddy Kinetic Energy (EKE) was calculated as: $(EKE = 1/2((u')^2 + (v')^2))$.

2.2.8 ROMS

We set up a regional modeling system, based on the Regional Ocean Modeling System (ROMS) (Shchepetkin and McWilliams, 2009). ROMS is configured as a nested set of three spatial domains, centered at 38W and 24.5N. The outside domain has a horizontal resolution of 9 km for a region of 2500 km by 2800km, the next domain has a resolution of 3 km for a region of 1100 km by 1000 km, and the last domain has a resolution of 1 km for a region of 360 km by 300 km. There are 50 vertical levels with a resolution of a few meters near the surface. The lateral boundary condition is the climatology, consisting of the monthly means derived from the Hybrid Coordinate Ocean Model (HYCOM) outputs of four years, from September 2008 through August 2011. The HYCOM model uses a resolution of about 9 km and data assimilation.(http://hycom.org/dataserver/glb-analysis). One-way nesting is

used for the lateral boundary condition for the two fine grid domains (Blayo and Debreu, 1999). The results presented here are extracted from the domain with a resolution of 3 km. To compute the surface fluxes, the atmospheric fields of 10-m winds, 2-m temperatures, precipitation rates, humidity, short- and long-wave radiation are used. They are derived form hourly forecasts from the Global Forecast System (GFS) at the National Center for Environmental Prediction (NCEP) and used to compute the wind stresses, evaporation, latent and sensible heat fluxes.

2.2.9 Aquarius

Aquarius CAPv2.0 L3 SSS data are used in this study. They are available at (ftp://podaac-ftp.jpl.nasa.gov/allData/aquarius/).

2.2.10 Budgets and turbulent flux definitions

The aim of this study is to evaluate the influence of mesoscale turbulence to the salinity budget in the subtropical North Atlantic. The equilibrium mass balance is given by

$$\iiint_V \nabla \cdot \rho\vec{v}\, dV = \oiint_{A_i} \rho\vec{v} \cdot \vec{n}\, dA = \oiint_{A_s} F\, dA \tag{2.1}$$

A_i denotes the interior surface and A_s the sea surface area of an arbitrary volume V. The forcing term F is the massflux at the surface (negative for evaporation), and $\vec{n}$ is the normal vector to the interior surface. When molecular diffusion and small scale mixing are neglected the equilibrium salt budget can be written as

$$\iiint_V \nabla \cdot \rho S\vec{v}\, dV = \oiint_{A_i} \rho S\vec{v} \cdot \vec{n}\, dA = 0 \tag{2.2}$$

For this study changes in density are neglected and ρ is assumed constant. From the mass balance follows:

$$\bar{F} = \overline{\vec{v} \cdot \vec{n}} \rho \frac{A_i}{A_s} \tag{2.3}$$

Overbars denote time averaged values. Similarly the salt budget can be written as:

$$V\overline{[\nabla \cdot S\vec{v}]} = \overline{\vec{v} \cdot \vec{n} S} A_i \tag{2.4}$$

For the rest of this study we will assume a simplified box volume: $V = A_s h$ where h is the depth of the box. Then the volume flux of freshwater out of the surface can be related to a salinity divergence within the volume using a constant reference salinity S_0:

$$\overline{F_V} = \frac{\overline{F}}{\rho} = -\frac{h}{S_0}\overline{[\nabla \cdot S\vec{v}]} \tag{2.5}$$

Note that this is an average flux over a surface area of $A_s = 1m^2$. A similar formulation can be used to calculate the absolute volume of freshwater V_{FW} that must be added to a volume of water with salinity S_1 to produce a box volume of depth h, surface area $A_s = 1m^2$ and salinity S_2:

$$V_{FW} = \frac{h}{S_0}(S_1 - S_2) \tag{2.6}$$

We now decompose the velocity and salinity into slowly varying mean fluxes (denoted by overbars) and turbulent (eddy) fluxes (time fluctuations shorter than 3 months, denoted by prime terms). This yields the following for the salinity flux term in equation 2.5:

$$\overline{\vec{v}S} = \bar{\vec{v}}\bar{S} + \overline{\vec{v'}S'}. \tag{2.7}$$

This study will focus on the turbulent salinity flux out of the SSS-max area (the second term on the rhs). For simplicity the term "equivalent freshwater flux" will be used throughout the manuscript, noting that mass cannot be mixed and we are dealing with a turbulent salinity

flux which can be expressed as equivalent freshwater flux of opposite sign, using equations 2.5 and 2.7:

$$\overline{F_V} = -\frac{h}{S_0}[\nabla \cdot \overline{S'\vec{v}'}] = -\frac{h}{S_0}\overline{[\nabla \cdot K\nabla(\bar{S})]} \tag{2.8}$$

The turbulent salinity flux $\overline{S'\vec{v}'}$ is approximated here by the product of a surface eddy diffusivity K and the gradient of the slowly varying mean surface salinity salinity field. This simplified formalism enables easy comparison of the relative role of turbulent lateral salinity fluxes and surface freshwater (mass) forcing in the area.

2.3 Observations

The surveyed region showed large upper ocean variability in time and space and on a variety of scales (Figure 2.2), in agreement with earlier underway measurements within this region. The SeaSoar and TSG surveys (Figure 2.3) revealed several distinct features in the surface layer above the permanent pycnocline. Areas of deep mixed layers (up to 150 m), penetrating to the pycnocline were generally found to be the saltiest waters in the region with a salinity of $\sim 37.4\,PSU$ and higher. These waters agree well with the climatological surface values in this region for March and April as well as the average properties in the upper 50 m over the whole cruise (compare the MIMOC profiles for March/April and the lower black diamond in Figure 2.5). These waters are subsequently referred to as SSS-max waters. The temperature and salinity (T/S) measurements show a considerable spread but there are two categories of water characteristics that deviate significantly from the SSS-max waters. Two principal types of fresh features, with higher and lower temperature than the SSS-max water, were found and their importance to the SSS-max region will be investigated below.

2.3.1 Warm/fresh features

The first warm and fresh feature was observed between $\sim 37.75W - 36.5W$ and $23.75N - 24.5N$ (Figure 2.3a and b, markers 1 and 2). Initially this feature had a strong surface

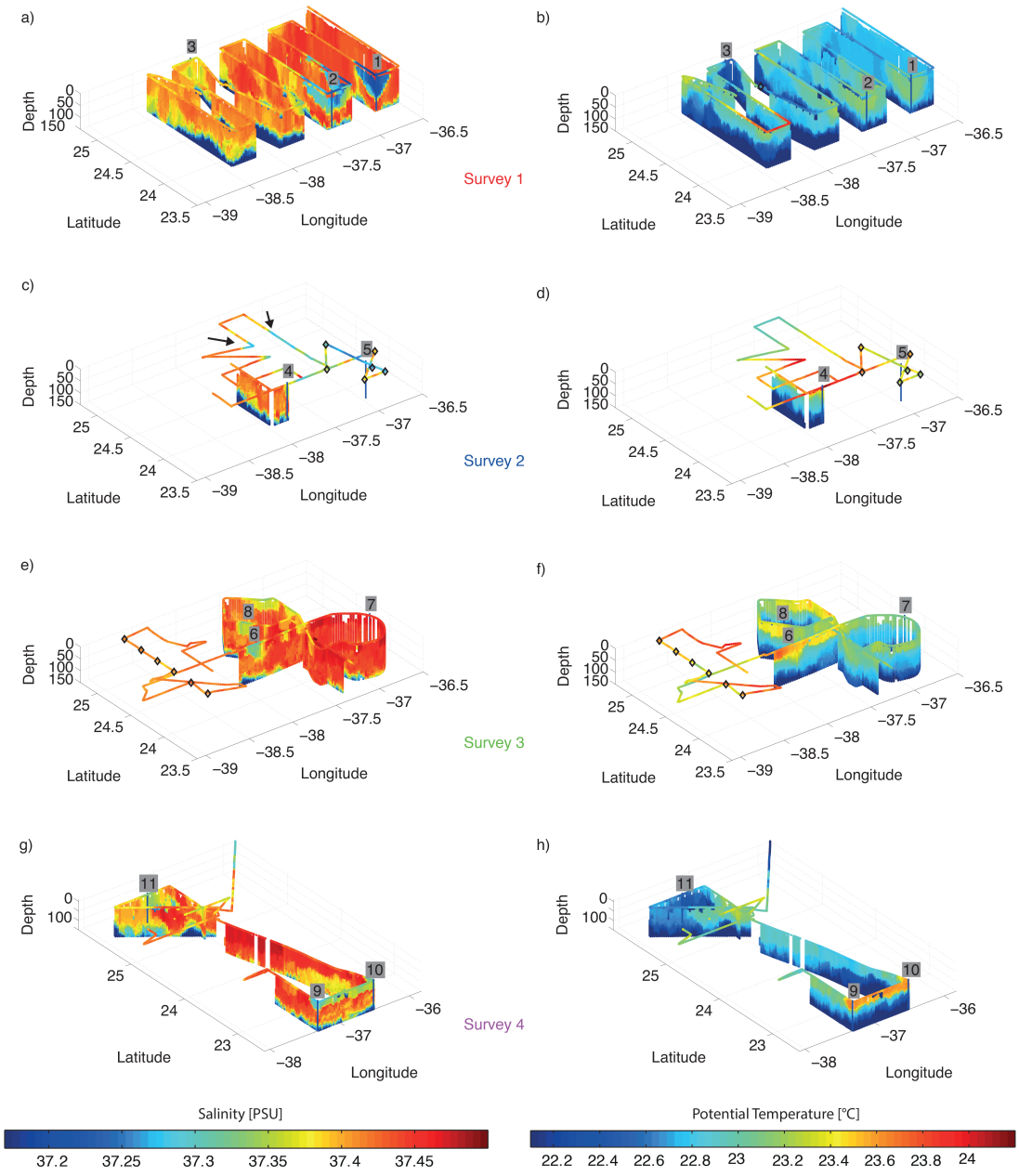

Figure 2.3: SeaSoar and TSG surveys. left column: salinity in PSU. right column: Potential temperature in $^{\circ}C$. Top row: March 22nd - March 28th; second row: March 28th - March 31st; third row: March 31st - April 4th; fourth row: April 4th - April 8th. Grey boxes and numbers are time marker for cross-referencing between figures used throughout the manuscript. Black diamonds indicate CTD stations. Note the changed lateral scales for Survey 4.

signature in temperature/salinity/density with pronounced surface and subsurface fronts to the east and slightly weaker fronts to the west. Changes in surface properties reach values on the order of 0.2 PSU and $0.3^{\circ}\,C$ over distances on the order of 10 km (Figure 2.4 upper panel). Water properties from near-surface TSG and deeper SeaSoar measurements compare well within the fresh feature. The fresh water defines a new mixed layer now considerably shallower (less than 90 m; e.g. Figure 2.4) than the surrounding SSS-max mixed layer. Below, the stratification between the base of the mixed layer and the permanent pycnocline is weak, and properties match the surrounding SSS-max waters which are colder and saltier. The surface fields in survey 2 (Figure 2.3 c and d) show a warm and fresh anomaly with an increased surface area extending further to the north (see Figure 2.3c black arrows). The northwestern extent of the fresh water is sampled well by cruise pattern and is found to the north of the location of the feature in survey 1, suggesting a northward advection of the fresh water volume (This will be supported by the AVISO/ADCP velocities discussed below). Surface gradients appear reduced compared to the first survey. The third survey (Figure 2.3e and f) shows only filamented structures with spatial extent of less than 25 km (Figure 2.3 markers 6 and 8). This discussion assumes that the fresh/warm anomaly at the surface is, at least in surveys 1 and 2, one coherent structure. Given the high spatial and temporal variability along the ship track and missing subsurface data in survey 2 this assumption cannot be conclusively proven (Figure 2.3c and d). Yet the TSG can be used with confidence to identify the extent of the anomaly, which along with the upper ocean velocity field described below, enable us to speculate on the movement of the fresh anomaly as a coherent feature.

The final survey (Figure 2.3g and h) was carried out to extend the survey southward where AVISO altimetry data and ROMS model output (not shown), reveal large EKE and surface salinity gradients, implying the potential for large eddy fluxes, which may be the ocean process shaping the annual cycle of the SSS-max and ultimately the S-max. Towards the south in survey 4 (Figure 2.3g and h) there is an anomaly similar to the one discussed

above, again with a pronounced surface gradient (see markers 9 and 10). This warm, fresh feature forms a strong lateral front with shallower mixed layers within the fresh area and the water below matching the adjacent deep SSS-max mixed layer waters (Figure 2.4). The temperature difference across the front is even slightly higher compared to the feature in survey 1 (up to $0.5\,^{\circ}C$ and 0.15 PSU over distances of $\sim 10km$). This second patch extends roughly about 100 km in longitude, but an areal estimate is not precise, due to the limited pattern coverage close to the frontal region. The depth of the fresh mixed layer is slightly less than seen in first feature. The evolution of this feature could not be observed during the cruise but its presence suggests that the phenomenon observed in the first survey is a regular feature of this area.

2.3.2 Cold features

Two cold subsurface anomalies were recorded during the cruise (Figure 2.3a and b marker 3 and Figure 2.3g and h marker 11). These features are fresher then the SSS-max water, but less so than the aforementioned warm features. They stand out mostly because they have a lower temperature than all of the surrounding mixed layer/deep mixed layer/surface waters. These features tend to have a very weak surface signature and generally show a stronger T/S structure below the surface. The T/S characteristics of these anomalies fit into the thermocline of this area (Figure 2.3a and b and Figure 2.5c marker 3 and 11), and they generally extend from the surface to the depth of the permanent pycnocline. Since the data do not enable us to analyze the evolution of one of those events as with the warm/fresh features the behavior remains speculative. Compared to the warm fresh features these were found further to the north in the measurement region in both observed cases. Rapid transects that include the northern part of the SPURS-domain include multiple fresh features within the mixed layer that show similar properties during the month of April [Gordon and Giulivi, this issue], indicating that these features might also be a regular phenomenon towards the northern boundary of the SSS-max.

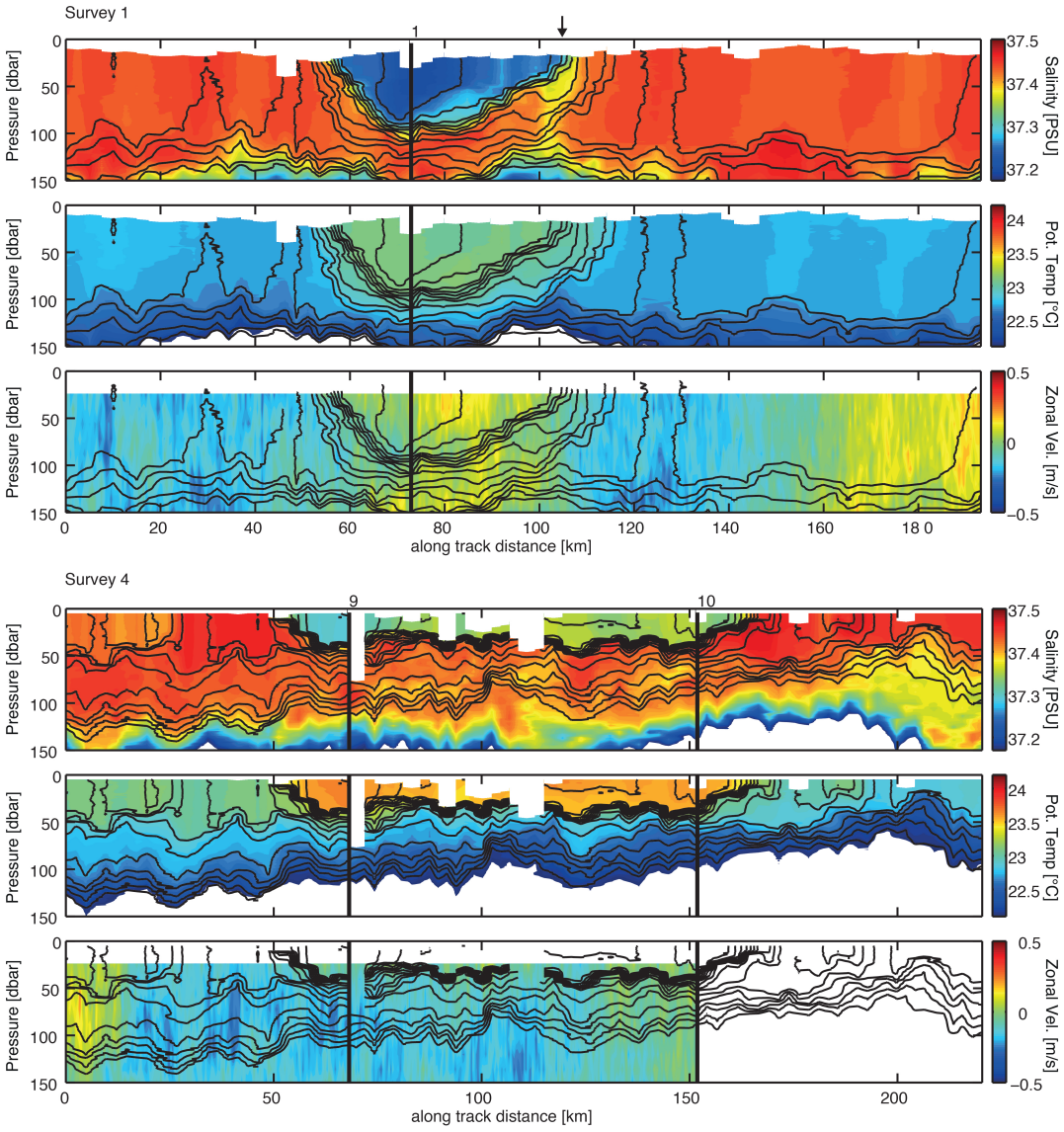

Figure 2.4: Section view of fresh features. The upper two panels are taken from survey 1 (salinity [PSU] on the upper, potential temperature on the mid and zonal velocity in the lower panel). Black arrow indicates the position of the fresh column mentioned in the text. The three panels below are the same but for survey 4. Black vertical lines and numbers denote markers to provide spatial reference (see Figure 2.3 a,b,g and h). Black contours indicate potential density (interval: $0.03 kg/m^3$). Missing velocity data at the end of survey 4 was caused by an error in the ship motion sensors.

2.3.3 The fresh Columns

An interesting aspect of the fresh and warm feature in survey 1 is the structure directly adjacent to the mixed layer front. A fresh vertical column extends downward close to the strongly tilted isopycnals of the front (north of marker 1 in Figure 3 a and b indicated by a black arrow in Figure 5a). Close to the surface isopycnals dip downwards, possibly indicating negative vertical velocities on the heavier side of the front. This agrees qualitatively with the circulation across a strengthening horizontal mixed layer density front (Klein and Lapeyre, 2009) and the subsequent slumping collapse of the front (e.g. (Fox-Kemper et al., 2008), Figure 2b). If actually caused by vertical velocities, the downdrafts of fresh and warm water could act as a mechanism to freshen the underlying waters, which show weak stratification with depth and match the surrounding SSS-max mixed layers. This would imply that the fresh features and the associated dynamics at the mixed layer front could be vital in determining the water characteristics in the region, maybe even in the deeper layers above the pycnocline. The shipboard measurements only provide a snapshot section of salinity, which could be the result of vertical velocities induced by a submesoscale ageostrophic circulation, or just the salinity signature of mesoscale stirring. Nevertheless, without additional data and analysis any conclusion drawn from this sample is highly speculative.

2.3.4 Upper Ocean velocities

The upper ocean velocities inferred from altimetry measurements agree well with the shipboard velocity measurements averaged over the upper 100 m of the water column and 1day-lowpass filtered (Figure 2.6). The northward advection of the fresh and warm feature is clearly supported by both the AVISO and SADCP velocity measurements. The good agreement between the purely geostrophic AVISO velocities, SADCP velocities and the evolution of the surface and subsurface salinities in the domain is compelling evidence for the role that mesoscale dynamics play in the behavior of these features. The Aquarius L3 SSS broadly depicts larger bodies of fresh water in the north and especially the south of the measurement

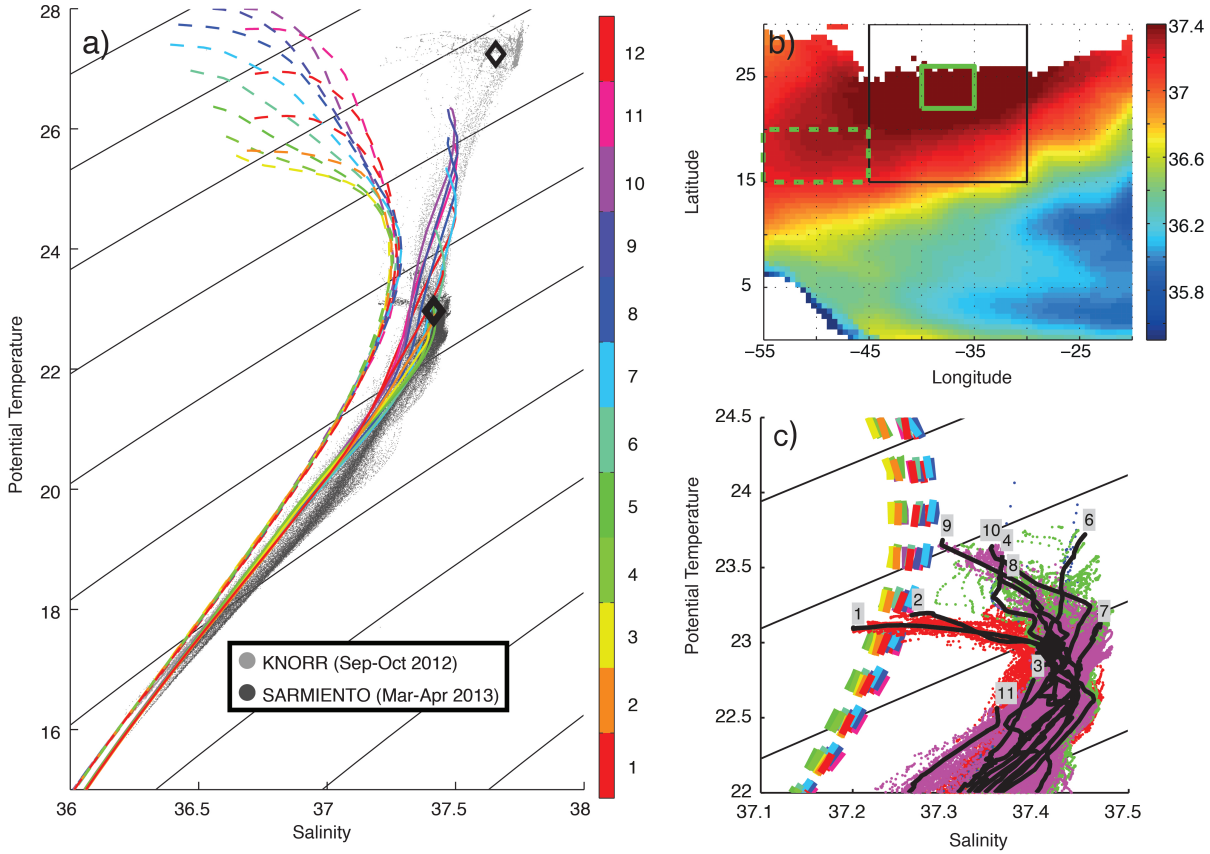

Figure 2.5: a) θ/S relation. Dots are SPURS cruises, dark grey for the SARMIENTO and light grey for the KNORR. Dashed (solid) lines are from the MIMOC climatology and represent the region denoted by the dashed (solid) green box in panel b). Black diamonds are the upper 50 m average for each cruise, upper KNORR, lower SARMIENTO. Black contours show σ_0 values. b) Annual average salinity of the subsurface maximum from MIMOC. Large black box is the SPURS-domain. Green boxes describe areas for panel a). c) Dots: θ/S relation from Sarmiento SeaSoar. Survey 1 in red, survey 2 in blue, survey 3 in green and survey 4 in violet. Thick black lines: numbered marked locations. Thin black contours as in a). Refer to Figure 2.3 for survey numbers and marked locations. Color-coded dashed lines are MIMOC θ/S relation from the panel b) white dashed box.

domain, which could be related to the fresh features during the survey. Aquarius spatial resolution and estimated accuracy (Lagerloef, 2013) is barely enough to resolve texture in the small measurement area, and comparison with the measurements at any given time on the cruise track is not useful. Nonetheless the bigger picture seems to fit with our hypothesized mechanism of fresh water intruding into the area from a larger body of fresh water to the south. The general structure of SSS seems to be aligned with some of the prominent velocity anomaly structures during the survey, which is an encouraging result for the Aquarius data, and promotes further use in the future.

2.4 Discussion

2.4.1 Importance for the regional salinity budget

Following equation 2.6 the volume of freshwater needed to dilute SSS-max water of $S_1 = 37.4$ to a typical value for the fresh feature of $S_2 = 37.2$ yields $V_{FW} = 27cm = 0.27m^3/m^2$ (with $h = 50m$ as a typical depth for the fresh feature). Assuming a surface area with extent of a half circle with 50 km radius for the fresh feature gives a total volume of at least $V_{(FW,Total)} = 10^9\, m^3$ for the anomaly. There are only three possible scenarios for the fate of this freshwater: Advection, evaporation out of the surface and mixing with the surrounding waters (both laterally and vertically).

First we will consider the possibility of lateral advection of the patch. The SeaSoar data suggest a northward advection in the south of the domain during survey 1 and 2, roughly in accordance to the AVISO velocities. To advect the southwestern edge in survey 2 following the AVISO fields to a region uncovered by measurements would imply unrealistic velocities well exceeding the previous movement of the feature as well as AVISO velocities. We conclude that the fresh structures sampled during survey 1-3 are indeed the same feature, hence we can speculate on the evolution of the feature. Obvious deformation of the fresh feature and weakening surface structures (discussed in detail later) further encourage the

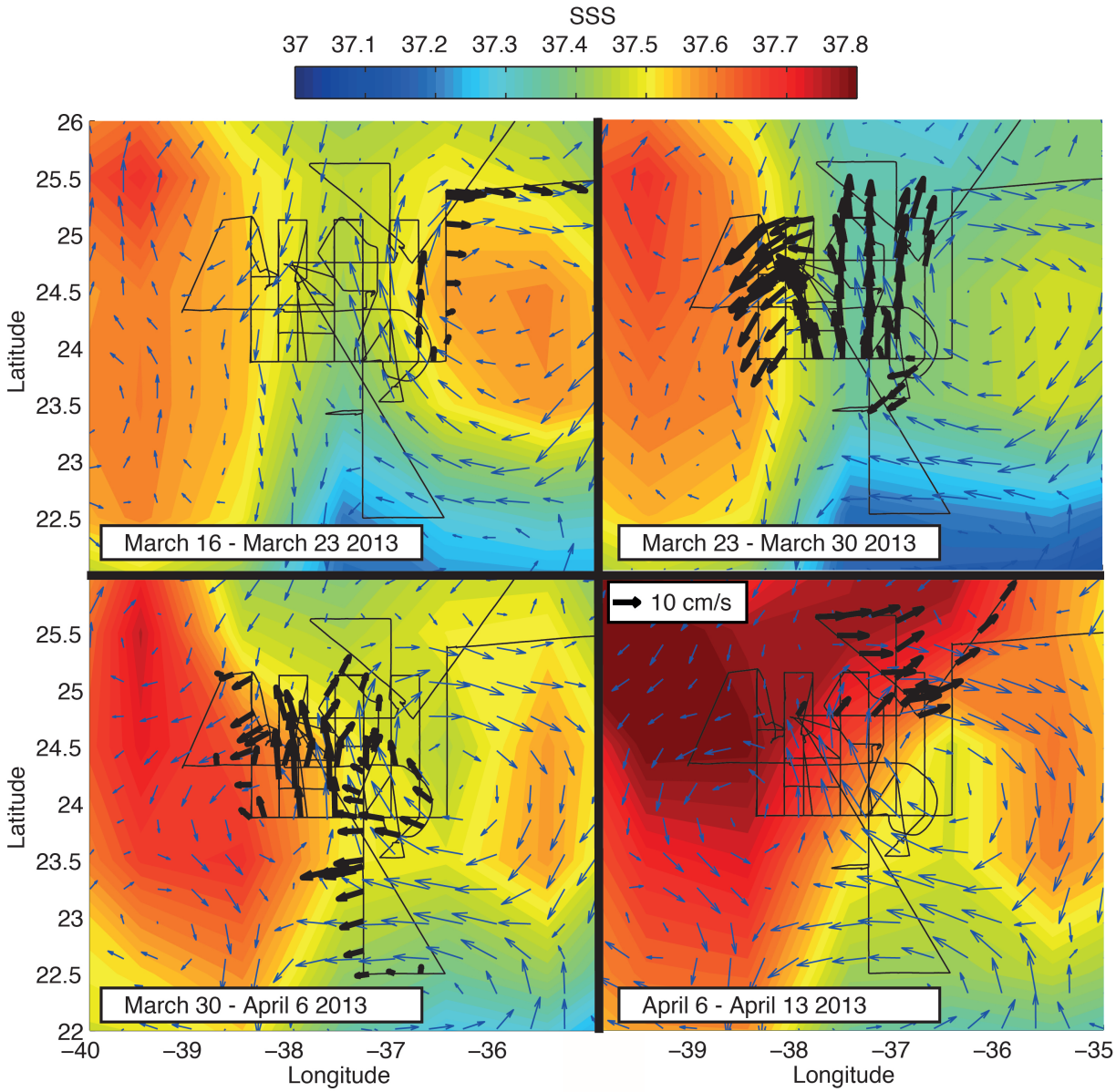

Figure 2.6: Black arrows: SADCP upper ocean velocities (20-100 m depth) measured from the Sarmiento. The line connecting the bases of the arrows is the cruise track. Velocities are lowpass filtered and subsampled every 60th point, corresponding to a time resolution of 2 hours. Blue arrows: Geostrophic velocities from AVISO altimetry. SSS from Aquarius is shown in color. Different panels depict different date ranges as shown in the lower left insets.

dismissal of the pure advection scenario. Additional comparisons with OSCAR current data (http://www.oscar.noaa.gov) were performed, which includes the effect of Ekman transport. Differences were marginal and not qualitatively different, hence we dismiss Ekman transport as an important factor for the advection of this specific feature.

The second possibility would be evaporation out of the surface. Earlier we estimated an additional 27 cm of fresh water that would need to evaporate out of every 50 m deep column with $A_s = 1\,m^2$. The NCEP-GFS fields used for the ROMS simulation at the end of March indicate that evaporation is mostly between 0.5-3 m/yr. To remove the full amount of freshwater at this rate it would take between 33-197 days, and with the April average net evaporation of 1.5 m/year (Gordon and Giulivi, 2014) it would take 65 days. These estimates should be viewed as gross overestimations given that large scale evaporation is not confined to the fresh surface waters: if strong evaporation is not perfectly aligned with the SSS the relative salinity gradient between the salty and fresh water masses would be maintained, with both waters experiencing a corresponding increase in salinity. Since the temperature of the fresh and warm features is higher, we evaluated the influence of a synthetic imposed temperature difference on the evaporation, by using bulk formulae following Fairall et al. (1996).The influence of the SST on the relative evaporation does not exceed 0.4 m/yr, resulting in an even longer time scale than 197 days for a pure evaporation scenario. Since the observed feature disappeared within about 14 days, we conclude that a substantial amount of the freshwater is added to the mixed layer budget in this area via mixing processes. A discussion of how the freshwater is dispersed this rapidly will be included below.

Given that a significant portion of the freshwater has to be added to the mixed layer in the SSS-max region, we need to evaluate the importance of this added freshwater for the SPURS-domain. Analyzing rain events, using the TRMM data set, shows that the volume of freshwater (needed to produce the features) is larger than 98.5% of the accumulated freshwater volume of any single rain event in this area over the period from 2009 to July 2013. The amount of freshwater carried within this structure might be even bigger due to

the unknown southern extent of the anomaly. Here we have used accumulated freshwater volume, as outlined in the data and methods section, to account for a possible deformation of the rain-diluted water due to ocean dynamics. A more traditional approach, using the mean rain rate per event multiplied by the duration of each event leads to the same basic conclusion that less than 0.2% of the rain events add $> 26cm$ freshwater per m^2 to the ocean surface. Along with the previous conclusions about the role of evaporation and advection, this points to the relative importance of the documented T/S anomalies on the surface layer salinity budget in the SSS-max region.

Naturally this leads to the question whether the phenomenon of the intruding fresh features is an exception or if these events happen regularly in the area, matching the idea of lateral turbulent salinity flux as a significant component of the mixed layer salinity budget in this region. Multiple data sources confirm the abundance of these fresh features within the area. VOS and TSG (Gordon and Giulivi, 2014) as well as Aquarius (Bingham et al., 2014) and ROMS model output show fresh and warm signatures year round, suggesting that these features play a significant role in balancing the excess evaporation at the surface by supplying freshwater to the region.

2.4.2 Origin of the anomalies

This leads us to the next question: Where is the freshwater originating from and what is the driving mechanism?

A local rain event and the advection of water from a region outside the SSS-max would be the only plausible scenarios. We showed earlier that the amount of freshwater represented by the anomaly exceeds most rain events within this area. Additionally the TRMM data for the time of the cruise does not show any rain activity that could explain the amount of freshwater contained in the observed fresh features. This further dismisses the process of local rain as explanation for the observations. Aquarius L2/L3 data at the time of survey 1 suggests an extensive area of fresh water to the south of the ship track (e.g. Figure 2.6).

Combining this evidence substantiates the idea of the feature originating from a larger body of water. Climatologic mixed layer waters with characteristics corresponding to the fresh features are found in the south/southeast of the measurement area, extending from 39W-31W between 20N-22N in March with slightly greater zonal and northern extent in April. Matching T/S characteristics are also found further to the west from the CRUISE-domain, still within the SPURS-domain. The map in Figure 2.8a shows regions in the surface layer that match the fresh and warm anomalies as well as the climatological S-max properties. The northward advection of the first fresh/warm feature suggests that it originated from the south of the measurement area. The fact that survey 4, which was carried out towards the south of the previous surveys, encountered a similar fresh structure further establishes the idea of the south/southeast being the source of fresh water features. The relative importance of the western region as origin of fresh water is hard to evaluate from the spatial and temporally limited survey that is presented herein, but the velocity patterns discussed above do not show evidence for freshwater import from the west. A similar analysis of the water properties yields an origin towards the north of the SSS-max for the cold/fresh anomalies, observed during the cruise (not shown).

Preliminary analysis of ROMS model output supports the proposed origin and fate of the fresh feature. The ROMS output presented here is able to reproduce the upper ocean structure in the SPURS-domain reasonably well. The model shows more fresh surface data points, but the maximum surface salinity and associated mixed layer depth is similar (exceeding 37.4 PSU and 100 m mixed layer depth). The model shows an abundance of fresh features that penetrate into the SSS-max water. Figure 2.7 shows an example of a fresh feature that penetrates from the southern region into the SSS-max waters. The fresh water at the eastern border reaches as far north as 24N with a salinity of $\sim 37.2\,PSU$. This is remarkably similar to the feature seen in survey 1 (Figure 2.3). The fresh feature advances northward, gets partially separated and increasingly filamented within $\sim$ 16 days. The SeaSoar data suggests the removal of the fresh features within $\sim$ 14 days (beginning of survey 1 to end of

survey 3), comparable to the feature in the model output. The depth of the simulated feature rarely exceeds 80 m and is found at approximately 50 m on average, values that compare well with the two fresh features seen in the SeaSoar survey (Figure 2.4). For the model, the spatial scale of the surface pattern of salinity varies strongly during the evolution of the feature. In particular, scales vary from $\sim 100 - 40\,km$ during the first days and decrease down to $\sim 10\,km$ after 16 days. This suggests an initial advection by mesoscale dynamics. This suggests that the ROMS model is successfully reproducing the hypothesized dynamics of the observed fresh features, which supports our previous conclusions. Further analyses of the SPURS region using ROMS will be explored in a separate manuscript.

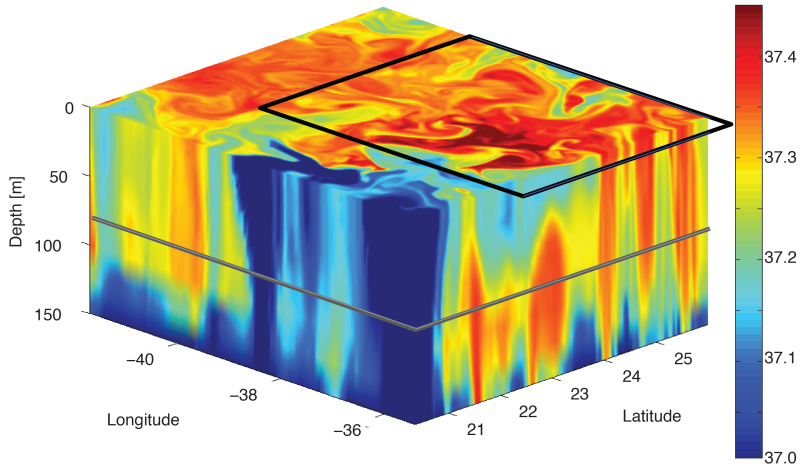

Figure 2.7: A snapshot of ROMS salinity field. Shown in color is a sliced 3d salinity field from a ROMS simulation, showing a feature similar to the one seen in the SeaSoar data (Figure 2.3). Grey line denotes a depth of 80m. The black surface box marks the measurement domain shown in previous figures.

2.4.3 Mechanism for the salinity flux

The last part of our discussion will evaluate dynamic mechanisms that could be responsible for the influx of freshwater into the region as well as the observed fast dispersal within the SSS-max. The observed structures appear tightly associated with mesoscale dynamics. Scales of fresh and warm features are on the order of the first baroclinic Rossby radius within

the region ($\sim 40-50\,km$ (Chelton et al., 1998)), or larger (at least in the beginning of their evolution). Their movement is well explained by the geostrophic velocity anomalies, which agree well with the instantaneous velocities from the ship. While we are only evaluating two fresh and warm features here, the evidence for the role of mesoscale dynamics in the evolution of these features is compelling. When we consider mesoscale turbulence/eddy fluxes as a mechanism for the export of salinity out of the SSS-max to balance the net evaporation of the surface it is important to mention that this does not just mean advection of fresher water into the salty water, but at the same time an export of salty water out of the SSS-max is needed. Mesoscale turbulence exchanges salinity by stirring (and subsequently mixing) of waters along a background salinity gradient. To estimate the potential importance of turbulent salinity flux to the salinity budget in the mixed layer and the role in compensating the net evaporation we approximate the turbulent fluxes following equation 2.8. We use the annual mean SSS field from the MIMOC climatology as the estimates of the salinity fields excluding the eddy effects. To obtain a reasonable estimate of the turbulent flux it is important that the mean tracer field does not show signatures of the actual eddies, which would enhance the curvature of the field and artificially inflate the flux estimate. The MIMOC climatology seems useful in this context since it was specifically derived to minimize the influence of transient structures like eddies in the climatological Argo fields. Furthermore visual inspection of the surface fields does not reveal any features of comparable size to the one investigated in this study. For simplicity we restrict the estimate to a constant eddy diffusivity $K = 1000-3000\frac{m^2}{s}$ from by (Abernathey and Marshall, 2013). The part in square brackets of equation 2.8 thus can be written as: $[\nabla \cdot K\nabla(\bar{S})] = [K\nabla^2(\bar{S})]$ A typical value for the research area (derived from MIMOC) is taken as $\nabla^2(\bar{S}) = 2 \cdot 10^{-12}\,PSU/m^2$ combined with a mean mixed layer depth of $h = 50\,m$ and a reference salinity of $S_0 = 37.2\,PSU$. This would result in a range of equivalent freshwater convergence of about 0.1-0.3 m/yr. Additionally, locally and seasonally the curvature of the salinity field can be considerably larger, meaning that this process can locally balance an even higher percentage of the net

evaporation.

Future work has to be carried out to constrain these estimates and investigate the spatial and temporal distribution of the salinity divergence by geostrophic turbulence. Nonetheless this result confirms that turbulent lateral fluxes are important in the annual salinity budget of the SSS-max, by compensating on average 10-30% of the mean annual net evaporation within the SPURS-domain, ($\sim 1\,m/yr$ from (Gordon and Giulivi, 2014)). This result is in broad agreement with an independent study that investigates the direct turbulent flux estimates using SODA data and concludes that the turbulent fluxes might compensate more than 50% of the loss of freshwater through the surface (Gordon and Giulivi, 2014). To relate the turbulent transport to the large-scale ocean and atmosphere context we have to look at the surface properties of the Subtropical Atlantic region: A key difference between the northern and southern border of the SPURS-domain is the meridional density gradient. Either side shows strong gradients in salinity and temperature (Figure 2.1) but to the south both fields reinforce the density gradient, while in the north the effect on density is opposite. The salinity gradient supports a salinity flux out of the SSS-max region from both north and south, causing regular appearance of both cold and warm fresh features as seen during the SPURS cruise. Both features vary in their vertical structure and density anomaly with respect to the local climatology. The cold fresh features seem to have little variation with depth until the permanent mixed layer is reached and show generally a lower density difference to the surroundings than the warm features. The vertical structure of the latter suggests a higher baroclinicity due to the surface intensified temperature and salinity anomalies, which might explain the fast dispersal. The stronger climatological density gradient in the south might be favorable for the growth of baroclinic instabilities (Charney, 1947), which acting on a strong meridional salinity gradient cause eddy flux of salinity out of the SSS-max region, despite the low mean flow. Indeed the southwestern area exhibits stronger EKE than the rest of the SPURS-domain in the altimetry observations (Figure 2.8b). The EKE in this region furthermore shows a seasonal cycle with maxima in May-July and minima around January-

March (Figure 2.8c). This general behavior is also seen in the ROMS model output. The net evaporation is anti-correlated to the surface salinity within the SPURS-domain (Gordon and Giulivi, 2014), whereas a 90-degree phase shift would be the expected relationship between net evaporation and surface salinity for a domain purely dominated by the surface forcing. This points to the influence of oceanic processes in setting the surface characteristics in this region. The EKE peaks at about the same time as the surface salinity reaches its lowest point and the net evaporation is greatest, suggesting that the turbulent flux of freshwater might balance a major part of the net evaporation together with the mean Ekman flow of tropical waters towards the subtropics from the north and south and possibly vertical mixing at the base of the mixed layer. The seasonality in the EKE and turbulent flux on seasonal to interannual time scales is likely influenced by changes in the wind field. The influence of the wind field on the interannual salinity of the SSS-max was pointed out as early as 1976 (Worthington, 1976). Idealized model studies show that eddy fluxes become important in the surface buoyancy transport in a downwelling regime like the subtropical gyres (Cessi, 2007).

It is important to realize that the Ekman flow and the eddy driven flux are coexisting processes and that the freshwater transport will be achieved as a combination of both. One notable difference between these two components might be the timescales of variability. The EKE shows a strong seasonal cycle and high interannual variability in both space and time, enabling it to play a role in the annual to interannual variability of the SSS-max waters, previously thought to be dominated by air sea fluxes only. Further work has to be carried out to investigate what process might link the large-scale wind field to the seasonal to interannual variability in turbulent fluxes. A likely candidate would be a change in large-scale density gradients by the Ekman transport/pumping, thus enhancing the available potential energy for baroclinic instabilities especially in the southern region.

A separate issue that needs discussion is the fast dispersal of the observed fresh and warm features in the center of the SSS-max domain. As stated earlier, the dominant process for

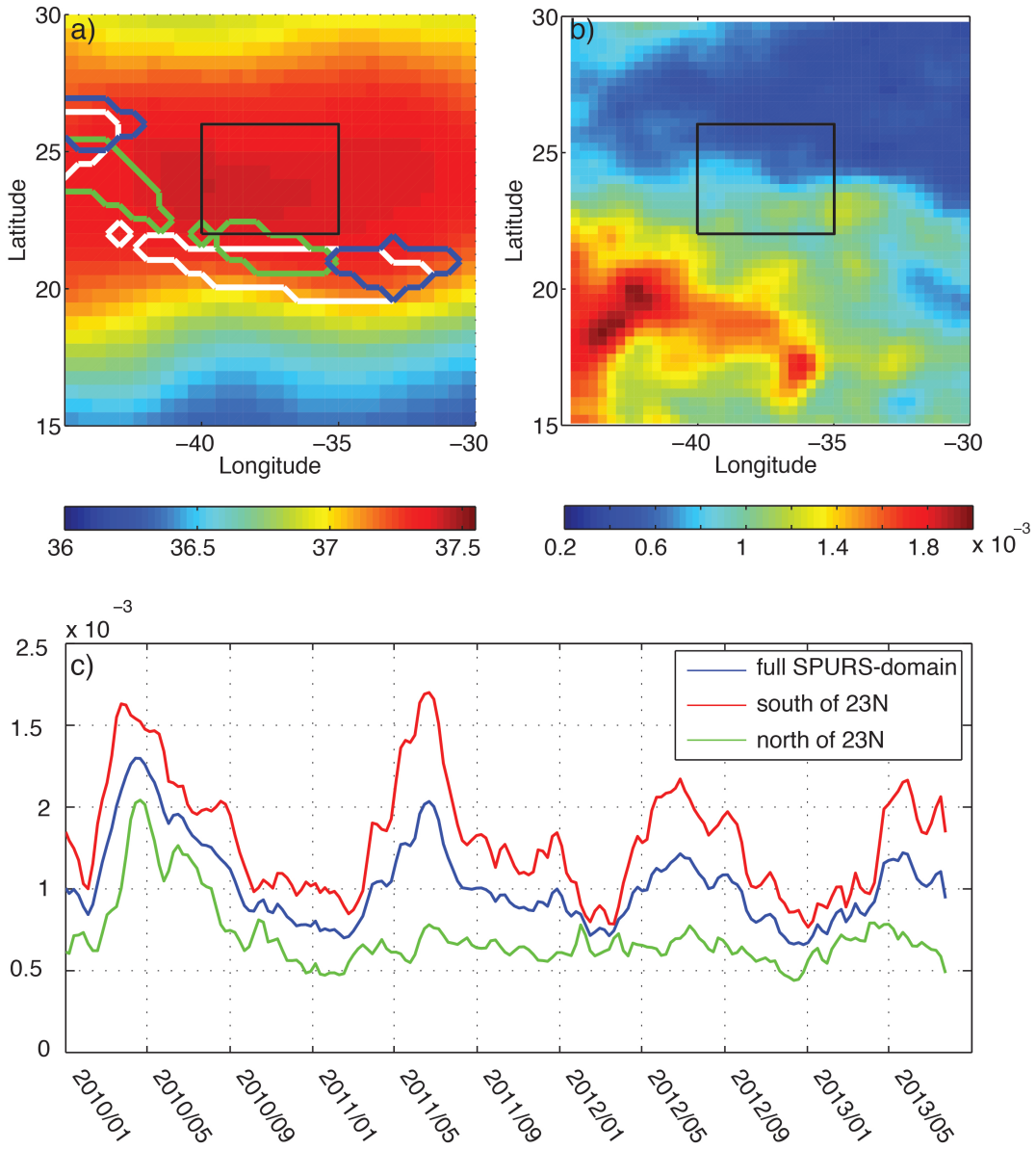

Figure 2.8: a) Mixed layer salinity [PSU] in the SPURS-domain from MIMOC climatology averaged from February to April (months of the deepest mixed layers) in color. Contoured are different water masses from the T/S diagram in Figure 2.5: white: the approximate range of the S-max; green and blue: the T/S characteristics of the two fresh/warm features discovered during the SARMIENTO cruise. b) mean of EKE from 2000-2013 in the SPURS-domain. Black box indicates CRUISE-domain. c) Time series of EKE in the SPURS-domain.

the lateral movement of these features seems to be mesoscale dynamics, which set up strong mixed layer fronts. To add the water into the surrounding mixed layer it ultimately has to be mixed vertically or laterally. Wind driven mixing and vertical entrainment are a possible mechanism but would lead to a deepening of the mixed layer. No evidence for a significant deepening of the fresh mixed layer was recorded during the March 2013 cruise. Limitations of the SeaSoar coverage hinder a comprehensive comparison of the mixed layer depth during the evolution of the fresh warm patch. But CTD stations (Figure 2.3d, black diamonds) do not show any mixed layer deeper than when the feature was first sampled.

The scales of the strong lateral density front and low vertical stratification create an environment favorable for active submesoscale dynamics. Rossby numbers O(1)-O(10) [defined as $Ro = \zeta/f$, ζ is the relative vorticity and f the Coriolis parameter] and Richardson numbers O(1) are found frequently in the upper 50 meters. Given this environment it is likely that active submesoscale dynamics drive strong mixing at the frontal edge and aid dispersal of the fresh water feature in a relatively short amount of time. Areas of strong density fronts along filaments and at the edges of eddies have been shown to contribute significantly to vertical exchanges in the upper ocean up to 500m ((Klein and Lapeyre, 2009) give an overview of observational and numerical studies). Mahadevan et al. (2012) and Fox-Kemper and Ferrari (2008) point out the importance of mixed layer eddies in restratifying the mixed layer. Wind mixing and restratification could work at the same time, and compete against each other (Mahadevan et al., 2012). Evidence for these mechanisms might be seen in the spreading and filamentation of the fresh/warm feature during its evolution, with little increase in depth during the process, as far as the measurements are able to identify the subsurface structure. To quantify the role of submesoscale dynamics in the dispersal of fresh water within the SSS-max domain is outside the scope of this study and should be evaluated in dedicated model studies since shipboard measurements barely resolve the largest feature ($\sim 10\,km$) in the submesoscale regime for the given stratification (typical scale is estimated as $L = Nd/f$ following (Thomas et al., 2008), with N being the buoyancy frequency, f the Coriolis parameter

and d the depth of the mixed layer.) Above we pointed out the vertical freshwater columns at the leading edge of the fresh warm feature. Qualitatively the structure looks very similar to the upper ocean structure in other studies that focus on submesoscale frontal dynamics (Fox-Kemper et al., 2008; Thomas et al., 2010), but at this point we are not able to attribute this structure explicitly to an ageostrophic circulation. Nonetheless it seems plausible that submesoscale dynamics are active in this region and accelerate the dispersal as seen in the survey above. This would add a substantial part of the intruded freshwater to the mixed layer during the breakup, possibly even freshening deeper regions of low stratification above the permanent pycnocline but below the fresh feature and the associated fronts.

2.4.4 Implications for the subtropical cell

Salinity distributions in the North Atlantic suggest that the SSS-max water gets exported towards the southwest (Figure 2.5b) at a depth of about 100-150m, (Worthington, 1976) Yet in the winter months (Jan/Feb/Mar), when the mixed layer is deepest the SSS-max water is too salty and cold to be connected to the S-max through isopycnal pathways. Diapycnal processes are thus needed to link the water properties in T/S space. This is confirmed in Figure 2.5a, using independent data from the MIMOC climatology. Since the used data record spans the period 2007-2011 it suggests that a diapycnal link is a general requirement and not an anomalous feature from the measurement period. The S-max in this study is not purely defined as south of the SPURS-domain but rather to the southwest, since the subsurface salinity maximum migrates towards the west with the North Equatorial Current (compare Figure 2.5b). The two fresh/warm features discussed above are similar as they provide a strong fresh/warm hence low density anomaly to the surrounding SSS-max waters. While the features differ slightly in their T/S characteristics, they both approach the properties of the S-max water and cross isopycnals (marker 1 and 9 in Figure 2.5c). Since we concluded earlier that a substantial amount of the anomalous water is added to the mixed layer by mixing processes, and that these fresh/warm events happen regularly,

they are likely a necessary process that links the SSS-max to the S-max. The cold/fresh feature does not seem to contribute to setting the water properties towards the S-max, since they are denser than the SSS-max waters. This emphasizes the importance of mesoscale turbulence (specifically towards the south of the SSS-max) not only to the SSS-variability but also potentially to the properties of the subducted water in the lower limb of the STC.

2.5 Conclusions

The observational data and model output presented in this paper suggest that the fresh and warm features, and their interaction with the SSS-max surface waters, represent the oceanic processes that ultimately balance a large part of the net evaporation in the subtropical Atlantic. Fresh and cold features seem to be abundant in both the observed data and the model output. The relative importance of these features to the freshwater input of the region remains speculative, since existing data do not enable us to estimate volume, evolution and the time scale of dispersal.

The observed fresh and warm features are not explicable by local rain, hence they must be advected from a different region. Intruding freshwater is quickly dispersed into the surrounding mixed layer and similar features are found frequently in ROMS model output and other data sets, confirming the importance for the salinity budget in the SSS-max region. Analyzing the scale and structure of the features, combined with the observed advection pattern, the equivalent freshwater flux is likely achieved by turbulent fluxes rather than mean flow within the mixed layer. The importance of these mesoscale dynamics to the lateral spreading of low salinity waters into the region is confirmed by the dominance of lateral scales larger than the first baroclinic Rossby radius and the good match between observed advection and geostrophic surface velocities from altimetry data. Fast dispersal is potentially caused by ageostrophic circulation at strong density fronts resulting from the advection of fresh and warm water into salty water. This would be consistent with a general picture of upper ocean

turbulent fluxes, where mesoscale activity dominates lateral turbulent fluxes while vertical fluxes are dominated by mixed layer eddies and fronts (e.g. (Fox-Kemper and Ferrari, 2008)). Variable turbulent fluxes can provide a necessary input of freshwater into the SSS-max and consequently establish the connection between SSS-max and S-max in T/S space. This results in a high potential for variability in the water masses that replenish the S-max caused by a combination of variability in air sea fluxes (e.g. (Hurrell, 1995), (Durack and Wijffels, 2010)) as well as mesoscale dynamics even on interannual timescales (while (Curry et al., 2003) only considers the ocean dynamics to be important on decadal timescales). Indeed Aquarius L2 data shows that the areas of highest interannual variability within the Aquarius record in the SPURS-domain are in the south and west of the CRUISE-domain (Bingham et al., 2014), close to the areas of high EKE and where the surface properties match the S-max in the climatology. The EKE itself shows very high spatial and temporal variability over the course of 10 years. It is highly likely that the interplay between these variations influences the transport of heat and freshwater through the STC, hence this might have a significant influence on the global ocean circulation and climate. How the mesoscale activity and turbulent flux of freshwater is controlled by large scale atmospheric variables and linked to the S-max properties will be subject of future work.

2.6 Acknowledgments

Support for this research was provided by NASA NNX09AU68G. We thank the crew and technical and scientific teams of the R/V SARMIENTO DE GAMBOA and R/V KNORR for their support in collecting the data at sea. The SPURS-MIDAS cruise was part of the MIDAS-6 project funded by the Spanish National R+D Plan under grant AYA2010-22062-C05-01. Jordi Font was supported under the Spanish AYA2012-39356-C05-03 project. Frederick M. Bingham was supported by NASA under grant NNX11AE83G. We appreciate the constructive comments from Andreas Thurnherr, Hsien Ou, Ryan Abernathey and

Claudia Giulivi.

Chapter 3

Lateral eddy mixing in the subtropical salinity maxima of the global ocean

Note: This Chapter has been accepted in *Journal of Physical Oceanography* (2017) [1]

Abstract

A suite of observationally driven model experiments is used to investigate the contribution of near-surface lateral eddy mixing to the subtropical surface salinity maxima in the global ocean. Surface fields of salinity are treated as a passive tracer and stirred by surface velocities derived from altimetry, leading to irreversible water mass transformation. In the absence of surface forcing and vertical processes, the transformation rate can be directly related to the integrated diffusion across tracer contours, which is determined by the observed velocities. The destruction rates of the salinity maxima by lateral mixing can be compared to the production rates by surface forcing, which act to strengthen the maxima. The ratio of

[1]AUTHORS: Julius Busecke [a]*, Ryan P. Abernathey [a], Arnold L. Gordon [a]

[a] Department of Earth and Environmental Sciences and Lamont-Doherty Earth Observatory of Columbia University, 61 Route 9W, Palisades, NY 10964, USA

* corresponding author: julius@ldeo.columbia.edu

destruction by eddy mixing in the surface layer versus the surface forcing exhibits regional differences in the mean - from 10% in the South Pacific up to 25% in the South Indian. Furthermore, the regional basins show seasonal and interannual variability in eddy mixing. The dominant mechanism for this temporal variability varies regionally. Most notably, the North Pacific shows large sensitivity to the background salinity fields and a weak sensitivity to the velocity fields while the North Atlantic exhibits the opposite behavior. The different mechanism for temporal variability could have impacts on the manifestation of a changing hydrological cycle in the SSS field specifically in the North Pacific. We find evidence for large scale interannual changes of eddy diffusivity and transformation rate in several ocean basins that could be related to large scale climate forcing.

3.1 Introduction

The terrestrial freshwater cycle and its behavior in a changing climate is a study area of utmost importance to humanity, specifically from a socio-economic viewpoint (Durack, 2015). Due to the interconnection of various branches of the water cycle and the vastly larger size of the ocean reservoir relative to the land surface (Durack, 2015; Schmitt, 2008) understanding the oceanic branch might be key in improving our understanding of how a changing climate will influence the terrestrial water cycle.

Studying the freshwater flux over the ocean is very challenging due to complicated and spatially sparse measurements and the reliance on bulk formulas for various flux products, resulting in large uncertainties between data sets (Schanze et al., 2010). Due to these difficulties, the idea of using sea surface salinity (SSS) as a proxy of the integrated freshwater forcing has emerged (Schmitt, 2008; Gordon and Giulivi, 2008). By removing (adding) freshwater through evaporation (E) (precipitation (P)) at the surface the SSS is raised (lowered). The general alignment between the areas of positive net evaporation (evaporation - precipitation) and local salinity maxima in the subtropical gyre of the North Atlantic was pointed

out as early as (Wüst, 1936). The complication with this approach, often called "salinity as an ocean rain gauge" (Schmitt, 2008), is the influence of ocean dynamics (Vinogradova and Ponte, 2013; Ponte and Vinogradova, 2016; Gordon, 2016).

The SSS distribution is influenced by advection and mixing both horizontally and vertically, and all processes need to be quantified in order to relate changes in the SSS field to changes in the water cycle. To achieve this goal, the SPURS (Salinity Processes in the Upper Ocean Study) field experiment was carried out in the SSS-maximum (SSS-max) of the subtropical North Atlantic, with the goal to observe all relevant processes in one of the global salinity maxima and then apply these findings to the other subtropical regions in the global ocean. An overview of the program and many relevant publications is given by Lindstrom et al. (2015).

Besides being relevant for the study of the surface salinity expression of a change in the global water cycle, the SSS-maxima are source regions for subtropical underwater (STUW, O'Connor et al. (2005)) that feed into the shallow overturning circulation (e.g. Schott et al. (2004)). These subducted water mass characteristics are important for the global climate since they contribute significantly to global tracer transports (e.g. Boccaletti et al. (2005)). This results from the strong circulation paired with strong near surface gradients, compared to the deep ocean. Hence changes in mean gradients of temperature and salinity might modify meridional heat and freshwater transports of the upper ocean. Additionally the subducted water masses are a potential pathway for subtropical surface anomalies to the tropical thermocline and subsequently the upwelling regions of the globe. Changes in surface salinity on isopycnals are by definition associated with temperature (spice) anomalies which have the potential to alter sea surface temperature once upwelled in the tropics. This emphasizes the need to study the mechanisms responsible for the variability of the SSS.

Observations during SPURS show strong lateral salinity gradients associated with mesoscale filaments. These gradients are most intense near the surface and the salinity variability is strongly reduced along the subduction path of the SSS-max (Busecke et al., 2014). Moti-

vated by these findings, this study focuses on the process of lateral eddy mixing within the mixed layer. The importance of eddy mixing to the mean salinity and volume budgets in the North Atlantic has been covered in various studies (Gordon et al., 2015; Busecke et al., 2014; Bryan and Bachman, 2014; Schmitt and Blair, 2015; Johnson et al., 2016; Amores et al., 2016) using different methods and data sources. When the destruction of the saltiest water masses is compared to the creation by positive net evaporation, the studies infer different mean values and temporal variability.

We introduce a novel approach to estimate the eddy mixing contribution in all subtropical basins with a coherent methodology. A suite of observation driven experiments is conducted where the mechanism of water mass destruction via eddy mixing is isolated. Using a salinity coordinate system, as in the pioneering study of (Walin, 1977), we investigate all major ocean basins. Together with the comparison of the mean effect of eddy mixing for the SSS-max, we examine the variability induced by the observed surface velocity field and test the sensitivity to seasonal and interannual variations in SSS fields. These sensitivity experiments enable us to identify the dominant processes for the variability in eddy mixing–the surface velocities or the SSS fields.

The manuscript is structured as follows: In the remainder of the introduction we address the discrepancies within the existing estimates with a brief overview of the existing studies estimating the relevance of eddy mixing to the North Atlantic SSS-max and discuss potential sources for disagreement. Then we introduce the methodology, model set up and data used for this study in Section 3.2. We present and discuss the results in Section 3.3 and conclude in Section 3.4, including possible future work.

3.1.1 Budgets and the choice of a control volume

In order to evaluate the importance of any process to a large-scale feature like the SSS-max, it is useful to investigate the salinity budget over a control volume that encompasses the feature of interest.

We start with the local salinity budget in a very general form.

$$\frac{\partial S}{\partial t} = -\nabla \cdot (F_S) = -\nabla \cdot (F_{S,Diff} + F_{S,Adv}) \tag{3.1}$$

with the boundary condition

$$F_{S,Diff} = F_{Surface}\,\hat{\mathbf{k}} \quad at \quad z = 0 \tag{3.2}$$

$\hat{\mathbf{k}}$ is the unit vector normal to the surface.

Here F_S is the sum of all both diffusive ($F_{S,Diff}$) and advective ($F_{S,Adv}$) oceanic salinity fluxes, and $F_{Surface}$ is the effective salinity flux due to freshwater forcing at the surface:

$$F_{Surface} = S(E - P) \tag{3.3}$$

E is generally larger than P in the subtropical basins (e.g. Schanze et al. (2010)), and no significant sources and sinks for salinity exist in the interior ocean. The SSS-max is surrounded by fresher waters in the horizontal and vertical, leaving the surface forcing as the only process that can lead to an increase in salinity. In order to maintain a steady state, the diffusive and advective fluxes have to be directed out of the high salinity region, balancing the surface forcing.

An appropriate volume has to be defined over which to compare surface forcing to salinity flux divergence. The salinity budget within an arbitrary volume V hence can be written as:

$$\begin{aligned} \iiint_V \frac{\partial S}{\partial t} dV &= \iiint_V -\nabla \cdot (F_{S,Diff} + F_{S,Adv}) dV \\ &= -\iint_{\partial V} (F_{S,Diff} + F_{S,Adv}) \cdot \hat{\mathbf{n}} \partial V + \iint_A F_{Surface}\, dA \end{aligned} \tag{3.4}$$

The second equality follows from the divergence theorem. The integrated salinity tendency can be related to the salinity flux through ∂V, the internal (oceanic) boundary of V and the

surface flux integrated over the surface area A. The vector $\hat{\mathbf{n}}$ is the unit normal vector of V.

Two general choices of volumes are used in the literature:

1. The Eulerian control box: Most studies use some variation of a box fixed in space. Either a local grid box (Busecke et al., 2014) or point measurement from a mooring (Farrar et al., 2015), zonally elongated boxes within the SSS-max (Gordon and Giulivi, 2014) or a larger box around the SSS-max (Qu et al., 2011; Amores et al., 2016).

2. The "water mass" boundary: The studies of Bryan and Bachman (2014); Schmitt and Blair (2015); Johnson et al. (2016) and this study utilize a control volume ($V(S_0, t)$) bounded by a surface of constant salinity S_0. It can be shown that this eliminates the advection term from the salinity budget, leaving only diffusion (both lateral and vertical) as a possible compensation for the surface forcing (Walin, 1977; Marshall et al., 1999). The budget becomes

$$\iiint\limits_{V(S>S_0)} \frac{\partial S}{\partial t} dV = - \iint\limits_{\partial V(S=S_0)} (F_{S,Diff}) \cdot \hat{\mathbf{n}} \partial V + \iint\limits_{A(S>S_0)} (F_{Surface}) \cdot \hat{\mathbf{n}} dA \tag{3.5}$$

   Note that in this case the surface forcing is also evaluated on the same isohaline control surface. The salinity budget in V can be related to the time change in volume bounded by the same isohaline (Transformation Rate; TFR) (see Bryan and Bachman (2014) for full derivation):

$$TFR = \frac{\partial (V(S_0, t))}{\partial t} = \frac{\partial}{\partial S_0} \iiint\limits_{V(S>S_0)} \frac{\partial S}{\partial t} dV \tag{3.6}$$

In order to compare the results of the Eulerian and water-mass budgets, either the variability in the position of the control volume has to be negligible or the spatial variability of diffusive salinity fluxes and surface forcing must be very homogeneous in space. We argue that these conditions are not met.

The SSS-max exhibits variability from seasonal (Gordon and Giulivi (2014); Gordon et al.

(2015)) to interannual (Bingham et al., 2014) to decadal (Gordon and Giulivi, 2008; Durack and Wijffels, 2010) time scales. Furthermore there is evidence for strong spatial variability of lateral diffusivities and SSS gradients (Abernathey and Marshall, 2013; Gordon et al., 2015), implying strong spatial variability of the resulting diffusive fluxes. This could explain some of the spread of results between the studies using fixed control volumes. In the presence of strong inhomogeneity, even small differences in the position of the control volume will lead to very different results for each of the terms in the salinity/volume budget. Besides the choice of the control volume, a second major factor is the actual quantification of each of the terms in the budget. We focus our study on a particular process–lateral eddy mixing in the near-surface layer–and proceed by reviewing common methods to quantify this process.

3.1.2 Quantifying eddy mixing

In this section we outline the exact processes we aim to study in detail with respect to the SSS-max.

Unsteady motions in the ocean play a large role for the general circulation, tracer transports and thereby global climate. Fox-Kemper et al. (2013) provides a review of mesoscale eddy transport in the ocean. Following their terminology, all fluctuations from the mean circulation with time scales of weeks and length scales of several hundred kilometers (i.e. mesoscale) will be referred to as "eddies."

Tracer fluxes caused by eddies are commonly expressed as a covariance term $\overline{\mathbf{u}'C'}$, where the primes indicate a deviation from the time mean represented by the over bar, such that $C = C' + \overline{C}$.

A common approach is to represent the eddy flux using a diffusive closure involving the the mean tracer gradient and a tensor $\mathbf{R}$:

$$\overline{\mathbf{u}'C'} \simeq -\mathbf{R}\nabla\overline{C} \ . \tag{3.7}$$

However, here $\mathbf{R}$ does not represent a purely diffusive process. The tensor can be split up into a symmetric diffusion tensor ($\mathbf{K}$) and an asymmetric advection tensor (e.g. Fox-Kemper et al. (2013) equation 8.25). Observational estimates of the diffusivity tensor are rare and usually derived from long term averages, and it is difficult to match such data sets to tracer fields to obtain an estimate of the diffusive eddy flux, let alone resolve the diffusive flux into the SSS-max in time. For further details and references on this approach the reader is referred to (Fox-Kemper et al., 2013) and references therein.

In order to circumvent these issues, we choose to simulate the evolution of surface tracer fields using observed surface velocities and diagnose the diffusive flux within a coordinate system defined by a water mass (here salinity). As illustrated in Fig. 3.1b and c, in a tracer coordinate system, advective stirring by eddies stretches and filaments tracer contours, leading to irreversible mixing (a.k.a. water mass transformation) at small scales and a net diffusive flux across tracer contours. In this context, and throughout our study, "eddy mixing" refers to the enhancement of small-scale mixing by mesoscale stirring (Figure 3.1).

To further separate the effects of the large scale tracer gradients and velocity we employ the concept of "effective diffusivity" (Nakamura, 1996). This diffusivity is appropriate for our analysis since it does not correspond to an Eulerian diffusivity, but rather represents the averaged enhancement of small scale diffusivity along a tracer contour. Thus it is directly relevant to the net diffusive flux across isohalines and into the SSS-max.

3.2 Methods and Data

As stated above, when evaluating a volume bounded by a tracer surface, the flux across this boundary can only be achieved by diffusion and the flux through the sea surface (Equation 3.5 and 3.6). The sum of these fluxes is directly related to the volume bounded by the isohaline.

Our approach is only focused on the near surface layer for several reasons. Firstly, the availability of velocity data for over 20 years through altimetry enables us to conduct a

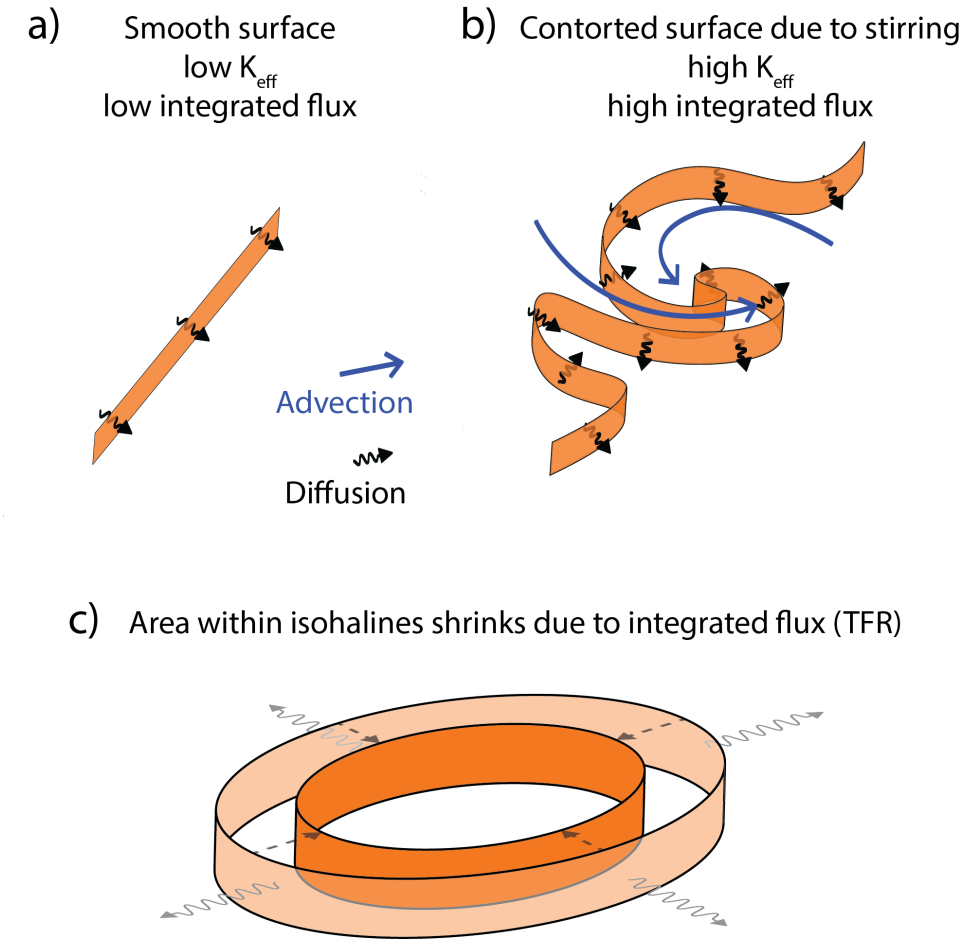

Figure 3.1: Schematic illustrating the investigated processes. Orange surfaces symbolize lines of constant surface salinity scaled by the mean Mixed Layer Depth (MLD). The smooth initial condition in each experiment (a) gets stirred by mesoscale velocities (blue arrows), which enhances the diffusive flux (black arrows) across the contour (b). The integrated flux across a closed contour (indicated by wavy gray arrows in c) leads to the destruction of salty water masses within the contour - the transformation rate (TFR; indicated by dotted arrows in c).

data driven study on eddy mixing, which is not possible with subsurface data at this point. Secondly, the strong lateral gradients observed within the mixed layer of the North Atlantic SSS-max (Busecke et al., 2014) point to the importance of the near-surface lateral eddy mixing versus the interior. Global inverse mixing estimates (Groeskamp et al., 2017) support the idea of lateral near surface eddy mixing being much stronger than along isopycnal mixing in the interior.

We simulate a 2D salinity field advected by observed velocities, without any other forcing. By eliminating all other processes, the evolution of the water mass volume is governed purely by lateral mesoscale stirring. If the contour is closed, the lateral diffusive flux, integrated along a tracer contour is now directly related to the area transformation rate.

$$TFR_A(S_0,t) = \frac{\partial}{\partial t} \iint\limits_{(S \geq S_0)} dA = -\int_{\partial A(S=S_0)} (F_{S,Diff}) \cdot \hat{\mathbf{n}} \partial A \tag{3.8}$$

In order to compare these values with the climatological surface forcing to determine the importance to the volume budget, they have to be scaled with a depth. We chose the mean mixed layer depth within an isohaline $\overline{MLD}(S_0)$ to focus on the variability of lateral mixing without masking the results with the temporal variability of the mixed layer depth. That variability is not small and certainly influences any full budget estimate. Large variability of the mixed layer depth can be seen in the NA (Busecke et al., 2014; Farrar et al., 2015). Here we want to specifically focus on the variability in lateral stirring processes, hence the choice of a constant depth.

$$TFR_{Eddy,V}(S_0,t) = TFR_{Eddy,A}(S_0,t)\overline{MLD}(S_0) \tag{3.9}$$

This can be seen as a special case of Equation 3.6, where V_{S_0} is the extruded contour of $S(x,y,t) = S_0$ (see Figure 3.1a). The upper and lower boundary both have the boundary condition

$$F_{S,Diff} = 0 \quad at \quad z = 0 \quad and \quad z = \overline{MLD}(S_0)\ . \tag{3.10}$$

In the following, the subscript V is dropped for simplicity, and all TFR values are in units of volume per time. To avoid confusion when referring to a strong (more negative) TFR, the sign for the TFR caused by eddy mixing will be reversed in all the plots.

With this setup we purposely neglect all other processes that influence the SSS in the real ocean like the surface forcing and all vertical processes, e.g. subduction, entrainment and diapycnal mixing. The robust nature of this diagnostic, which relies just on the area within a contour and isolation of the mixing effect of the observed velocities enables the study of temporal variability in eddy mixing. The downside of this approach clearly is the integral character of the results. It is not possible to diagnose local extrema in fluxes. It is well suited for the purpose of this study, since the main interest lies in the role of lateral eddy mixing to the formation and maintenance of the large scale SSS-maxima.

3.2.1 Surface forcing compensation

Transformation rates by eddy mixing are compared to the volume transformation rates by surface forcing in salinity coordinates (using equations 3.3 and 3.6):

$$TFR_{EP,V}(S_0,t) = \frac{\partial}{\partial S_0} \iint\limits_{(S \geq S_0)} S(E-P)dA \tag{3.11}$$

To analyze the importance of eddy mixing to the budget, we compare the ratio of TFR due to eddy mixing with the TFR due to surface forcing. We call this ratio the surface forcing compensation (SFC):

$$SFC = -\frac{\overline{TFR_{Eddy}(S_0,t)}}{\overline{TFR_{EP}(S_0,t)}} \tag{3.12}$$

3.2.2 Effective diffusivities

It is worth dissecting variability of the TFR into contributions from variability in the stirring (velocity fluctuations) and variability in the background salinity field, which includes changes in local gradients as well as a changing position of the reference isohaline. To isolate the

effect of the velocity fluctuations, we calculate the effective diffusivity. This method uses the same water mass frame of reference as the TFR and is thus directly comparable to the other results.

The effective diffusivity is a diagnostic developed by (Nakamura, 1996) to measure the diffusive transport across an instantaneous tracer contour. It represents the net mixing integrated along the tracer contour (salinity contour in our case). The effective diffusivity for a tracer q can be written as

$$K_{eff}(q) = \kappa \frac{L_e^2(q)}{L_{min}^2} \tag{3.13}$$

where κ is the molecular (or grid-scale) diffusivity, L_e is the "equivalent length" of an instantaneous tracer contour, and L_{min} is the minimum possible length that contour can achieve under a conservative rearrangement of the tracer field (Marshall et al., 2006). L_e can be calculated from the instantaneous tracer field. Stirring by mesoscale turbulence leads to highly filamented tracer contours and causes L_e to be many times greater than L_{min}, leading to enhanced mixing. The ratio L_e^2/L_{min}^2 quantifies the relative enhancement of molecular / grid-scale diffusivity due to this stirring. Although K_{eff} formally depends on κ, it was shown by Marshall et al. (2006) that this dependence drops out in the high-Peclet-number regime because L_e^2 also depends inversely on κ.

Following Nakamura (1996), the equivalent length of any tracer contour q can be calculated as:

$$L_e^2(q) = \frac{\frac{d}{dA}\int_A |\nabla q|^2 dA}{(\frac{\partial q}{\partial A})^2} \tag{3.14}$$

As described therein this value can be evaluated at any tracer time step and is then mapped back to a 'reference position', in this case the tracer contour position in the smooth initial field of each experiment. The minimal length of the contour L_{min}^2 is simply the L_e^2 value corresponding with the initial condition of each experiment, before stirring has caused any filamentation of the contour.

Even though this diagnostic has been mostly used in scenarios with a high degree of

uniformity in the zonal direction like the Southern Ocean (Abernathey et al., 2010) and the central part of the Pacific (Abernathey and Marshall, 2013), it can be applied to any tracer field. An example of this application can be found in Lee et al. (2009), who studied the effective diffusivity of a tracer patch released in the subtropical gyre. In the case of the SSS-max, the salinity contour values map geographically to the distance from the center of the maximum.

The effective diffusivity is not defined for a vanishing background gradient. To avoid the occurrence of weak tracer gradients our initial conditions are reset in regular intervals as described below.

3.2.3 Data

We use absolute geostrophic velocities from the AVISO DUACS2014 (1993-2014) altimetry product, produced by Ssalto/Duacs and distributed by Aviso, with support from Cnes (http://www.aviso.altimetry.fr/duacs/). The data is subset in weekly fields and has a native spatial resolution of 1/4 degree. We assume that the velocity fluctuation of the largest most energetic eddies are captured by this data. The long standing AVISO record represents our current best estimate of the surface eddy field. Since there is no similarly long, global observational record of higher resolution we are not able to investigate how unresolved velocity structures influence the results. Such a comparison will be left to future studies. The geostrophic velocities do not include the Ekman velocities at the surface, but as Rypina et al. (2012) show, these have little influence on the mixing characteristics at the surface. Climatological SSS fields as well as mixed layer depth are taken from the MIMOC-Argo climatology (Schmidtko et al., 2013). The data are given as climatological months with a spatial resolution of 1/2 degree. Additionally annual SSS fields are used from ECCO-MIT v4 r2 ocean state estimate (Forget et al., 2015) and the ADPRC gridded Argo product (http://apdrc.soest.hawaii.edu/projects/Argo/data/gridded/).

E data is taken from the OAFlux (Yu et al., 2008) monthly mean product and P from

the Global Precipitation Climatology Project (GPCP) (Huffman et al., 2010), both of which have a spatial resolution of 1 degree. The fields are averaged into climatological monthly means and interpolated on the MIMOC grid for analysis.

3.2.4 Model setup

We conduct a suite of experiments by stirring initial SSS fields with observed velocities. From these experiments, we diagnose the transformation rate by eddy mixing and surface forcing as well as the effective diffusivity.

The basis for this study are numerical experiments run in the MITgcm (Marshall et al., 1997) following the setup of Abernathey and Marshall (2013). The model output is calculated in 900 second intervals and tracer snapshots are output every 7 days. Initial SSS fields are passively advected by 7-day snapshots of two-dimensional AVISO absolute geostrophic velocities after both have been interpolated onto the 1/10 deg. model grid. The velocities need to be slightly corrected in order to be non-divergent, using the procedure described in Abernathey and Marshall (2013) Appendix A. The only difference from that study is that here we used the newer DUACS 2014 product from AVISO. Tracer transport across isolines can only be achieved via the model's prescribed grid-scale diffusivity κ (the schematic in Figure 3.1 illustrates the process). However as discussed in detail in Abernathey and Marshall (2013) and references therein, the width of tracer filaments (and thereby L_e^2) is also dependent on κ, in such a way that the effective diffusivity is largely independent of this value. This makes the results robust in the sense that they are not governed by an internal "tuning" parameter of the model but instead depend almost completely on the velocity input, which is derived from observations. The small scale diffusivity for these model experiments was diagnosed as $\kappa = 63 m^2/s$ (Table B1, Abernathey and Marshall 2013).

In addition to calculating long-term averages of TFR_{Eddy} and K_{eff}, we expanded the method with the explicit goal of resolving temporal fluctuations in eddy mixing. Due to the lack of a restoring mechanism for the tracer, over long time scales the tracer field will

increasingly homogenize and large-scale features might be deformed and shifted. In a homogenized tracer field no mesoscale velocity can produce a tracer fluctuation and the diagnostics presented here become meaningless. The advection and deformation of large-scale features will impact a useful remapping of the results to the initial conditions. This prompts us to reset the tracer fields in regular intervals, or results could not be interpreted anymore using the initial position of the SSS-maxima. This methodology is well suited to examine the SSS-maxima in the subtropical gyres, since mean advection is relatively low and the main features are not advected out of their original position quickly. Two tracers are simulated in parallel and reset at different phase and the results are averaged to eliminate any residual drift in the diagnostics and maintain the background field "quasi- constant". We obtained an uncertainty associated with the reset period by comparing certain ranges. All results that are discussed as significant exceed this uncertainty, and are as such assumed to be robust features of the input fields derived from observations. For further details see Appendix.

3.2.5 Initial conditions

Each setup as described above will result in time series of TFR and K_{eff} for each basin, describing the influence of a changing velocity field, which evolves with time but is the same in each experiment. The results might depend of the initial condition, which determines the position and hence exposure of the reference isohaline to possibly different features of the velocity field. To investigate the eddy mixing sensitivity to changes in the initial conditions we evaluate a suite of experiments with varying tracer initial conditions, all of which are averaged SSS fields. These are reset in an identical manner as described above , keeping each of the different initial conditions "quasi-constant". Nothing but the initial condition is changed between the various experiments. In the following each experiment is denoted by a suffix indicating the initial conditions used as outlined in Tab. 3.1.

Comparison between the different initial condition experiments then gives an indication of the sensitivity of the results to the variable background fields. None of these experiments

will give a realistic representation of the actual variations in eddy mixing which are likely to depend on both variable velocities and SSS fields.

Consider a strong stirring anomaly that only occurs during a time X. One of the SSS-max features could 'move' into that particular region during time Y. This would result in a strong variation of the diffusivity and TFR in the experiments with the initial conditions close to time Y. This however could be irrelevant for the 'actual' SSS-max when time X is not equal to time Y, or it could even emphasize the variability when they are equal. To get a crude estimate of such a combined variability we introduce the "combined" experiments. These are not separate experiments, but instead combine the results of the existing experiments according to the matching initial conditions. This still does not provide a fully resolved time series for each basin, but it provides a guide for interpreting the importance of variability in diffusivity and transformation rate and exclude completely improbable scenarios that can arise due to the combination of the full variable velocity record with averaged and non-evolving initial conditions. Using these estimates we can investigate situations where the spread between experiments is large and whether any detected variability could be significant for the real world SSS-max

The procedure is explained in detail in the Appendix and shown schematically in Figure A2.

To summarize the main diagnostics used in this paper before we discuss the results:

- Effective Diffusivity: The cross isohaline eddy diffusivity, relevant for water mass transformation. A measure of the stirring strength of the velocity field on the boundary of the volume, not dependent on the background gradient.

- TFR: A measure of the integrated diffusive flux into the volume bounded by an isohaline. Compared to the effective diffusivity TFR incorporates both the velocity statistics and the background gradient.

- SFC: The comparison of the lateral diffusive flux into the volume vs. the surface

Group suffix	Individual suffix	Initial SSS condition
-	mean	full time mean (MIMOC)
monthly	jan	climatological January (MIMOC)
	feb	climatological February (MIMOC)
	...	...
	nov	climatological November (MIMOC)
	dec	climatological December (MIMOC)
annual, ECCO	ECCO 1992	annual mean 1992 (ECCO)
	ECCO 1993	annual mean 1993 (ECCO)
	...	...
	ECCO 2010	annual mean 2013 (ECCO)
	ECCO 2011	annual mean 2014 (ECCO)
annual, ARGO	ARGO 2006	annual mean 2006 (APDRC)
	ARGO 2007	annual mean 2007 (APDRC)
	...	...
	ARGO 2013	annual mean 2013 (APDRC)
	ARGO 2014	annual mean 2014 (APDRC)

Table 3.1: List of initial conditions and corresponding suffixes used in the text. Data sources are given in parentheses in the last column. See Section 3.2 for details.

forcing integrated over the corresponding sea surface. This gives an indication of how important surface eddy mixing is for the volume budget.

3.3 Results

The mean salinity differs significantly between the global ocean basins. In order to compare the saltiest regions, we use the reference salinities S_{ref} from (Gordon et al., 2015). Each basin is then analyzed in regional boxes to ensure the values represent only the SSS-max region and not other areas with identical salinities. See Figure 3.2 for the position of the reference salinities as well as the regional boxes used.

3.3.1 Mean

The results for the mean SSS fields can be seen in Figure 3.3, with each of the diagnostics plotted against the bounding salinity contour with the regional reference salinity subtracted. The purpose of showing the full salinity domain is to demonstrate that, within the highest

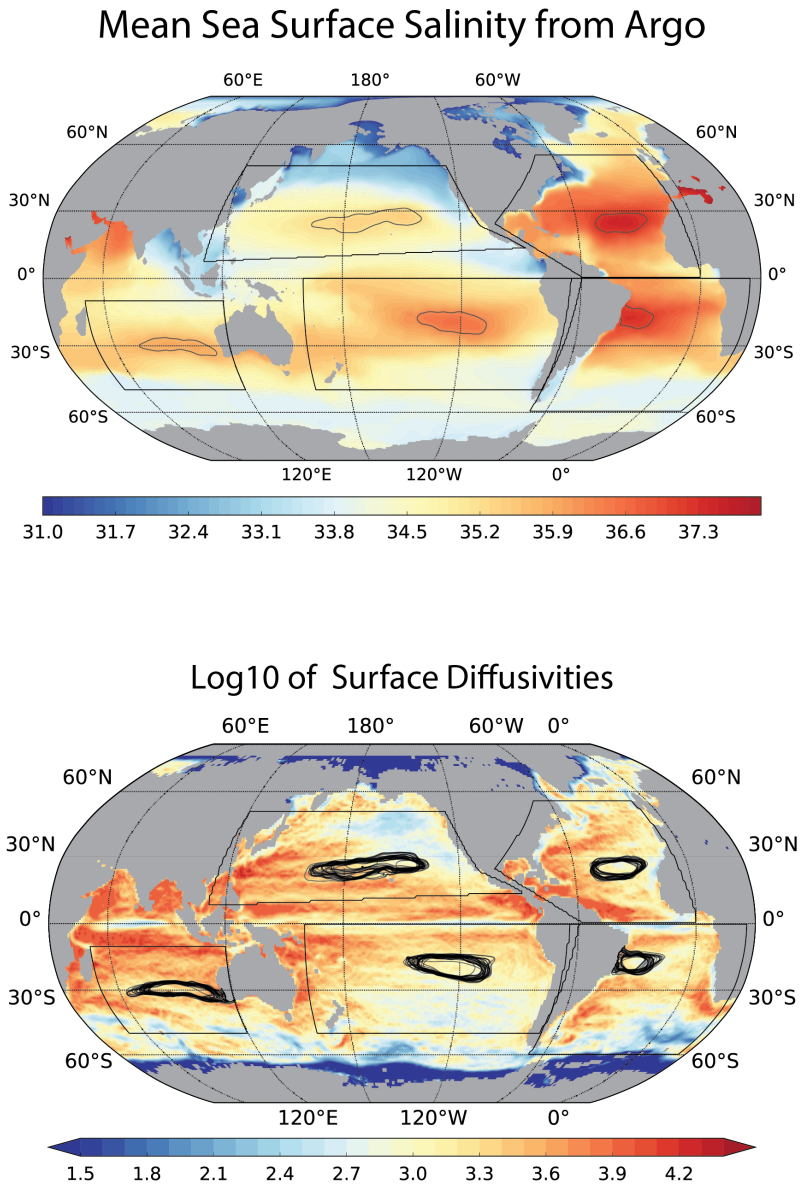

Figure 3.2: Mean SSS from MIMOC (upper) and surface diffusivities reproduced from Abernathey et al. 2013 (lower) in color. In the upper plot the black contour represents the S_{ref} contour for each basin based on Gordon et al. (2015) for the $MIMOC_{mean}$ initial condition. In the lower box the same salinity is shown for all used initial conditions (see Tab. 3.1 for reference). Black boxes indicate regional domains used in this study.

salinities of each basin, the results are relatively constant and not strongly dependent on the choice of the reference salinity. Hence for all further analysis we show the values on the basin specific reference isohaline S_{ref} only (indicated by the horizontal line in Figure 3.3).

Note that the lower values represent isohalines further outward from the SSS-max. Thus they might not be contained within the regional boxes. This will violate the previously outlined equations, by introducing a non zero lateral boundary flux. As discussed later in the Appendix, the low lateral gradient in the Southern Indian (SI) presents a problem with regard to this constraint. Outer salinities in the SI should be regarded as unreliable. We confirmed that for all experiments the actual reference isohaline is well contained in the regional domains (see Appendix).

Figure 3.3 shows the $TFR_{Eddy,mean}$ is highest in the SI and North Pacific (NP) with mean values of about $3.4/3.5Sv$. The other basins show lower TFR with the North Atlantic (NA) at about 2 Sv, followed by the South Atlantic (SA) with about 1.5 Sv and the South Pacific (SP) with 1.2 Sv. The difference between the NP/SI and NA/SA/SP might reflect the larger area within salinity contours due to the weaker lateral salinity gradient and do not necessarily indicate a higher relative contribution to the budget by eddy mixing. The SFC (Figure 3.3b) illustrates this by showing what percentage of the TFR_{EP} is compensated by $TFR_{Eddy,mean}$. Here the SI still has the highest value (25%) while the NP is found well in the spread of the other basins. The standout basin in terms of TFR and SFC seems to be the SP that shows the lowest SFC at $< 10\%$ for salinities $< S_{ref}$ throughout most of the salinity space. The NA which in terms of salinity processes has received the majority of the attention in the science community during recent years has a SFC of around 20%.

Regional differences also emerge in the diffusivites (Figure 3.3c). The SP again shows the lowest values compared to the other regions. But the basin ranking in SFC is not mirrored in all the K_{eff} values. Most notably, the SI has weak diffusivity values while the transformation rate is highest. Alignment of high local diffusivities with high gradients that dominate the overall TFR, and in turn the SFC, are necessary to explain this behavior. This illustrates

that localized structures can be decisive for the total diffusive flux out of the SSS-max. The effects of these structures for the mean quantities is captured with the methods used here, but it is not possible to locate these "hot spots" in space with our method.

Any localized covariance between gradient and diffusivity is important for understanding temporal variability in eddy mixing. Our observation driven model studies are therefore well posed to investigate temporal variability in eddy mixing by representing the interrelated variability of the SSS and eddy fields in both time and space.

3.3.2 Comparison to existing studies

To our knowledge the closest studies using a comparable control volume (isohaline coordinates) are Bryan and Bachman (2014) (North Atlantic only) and Johnson et al. (2016) (global). Both studies use the same methodology and model setup. Another study by Schmitt and Blair (2015) applies diffusivity estimates to a climatology in a similar framework and finds similar results as Bryan and Bachman (2014). They investigate the full volume bounded by the isohaline, including the subsurface below the mixed layer. There are some caveats to the comparison as outlined below, but as we conclude, the most striking regional characteristics seem robust when compared to our results.

The comparison between the three studies above might be complicated by several issues. The model studies show large biases in their surface salinity fields, which changes the mean position of the outcrop area. Hence even when we present our results in the exact reference salinities of their study, the bounded area can vary significantly. This could not only affect the water mass transformation by eddy mixing but also the appropriate surface forcing term. Bryan and Bachman (2014) show a comparison of the forcing term and the water mass transformation rate due to surface fluxes, where the model term deviates significantly from estimates using climatological data sets (Figure 3.4).

In order to compare our results with these previous studies, most of which evaluate the salinity budget, we additionally calculated the SFC for the salinity budget. By integrating

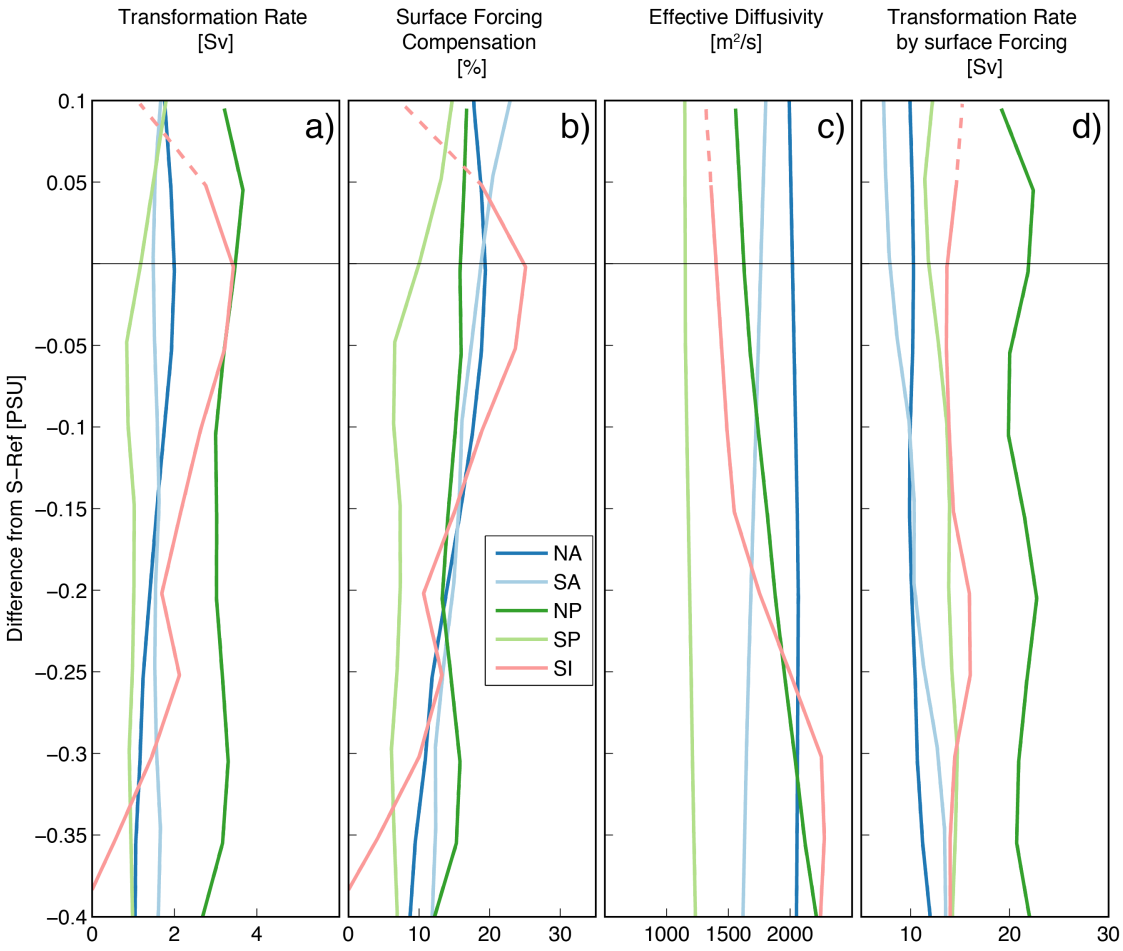

Figure 3.3: Time averaged diagnostics in salinity space. All computed from '$MIMOC_{mean}$' experiment. a): Transformation Rates (TFR) by Eddy Mixing . b): Surface Forcing Compensation. c): Effective Diffusivities (K_{eff}). d): Mean Transformation Rates by Surface Forcing. Colors indicate ocean basin and the y axis is the salinity of the bounding isohaline. The y-axis represents the difference from the S_{ref} value (Figure 3.2) in each basin, with positive values representing isohalines toward the center of the SSS-max. When the area within an isohaline is smaller than 100 grid boxes the line is dashed.

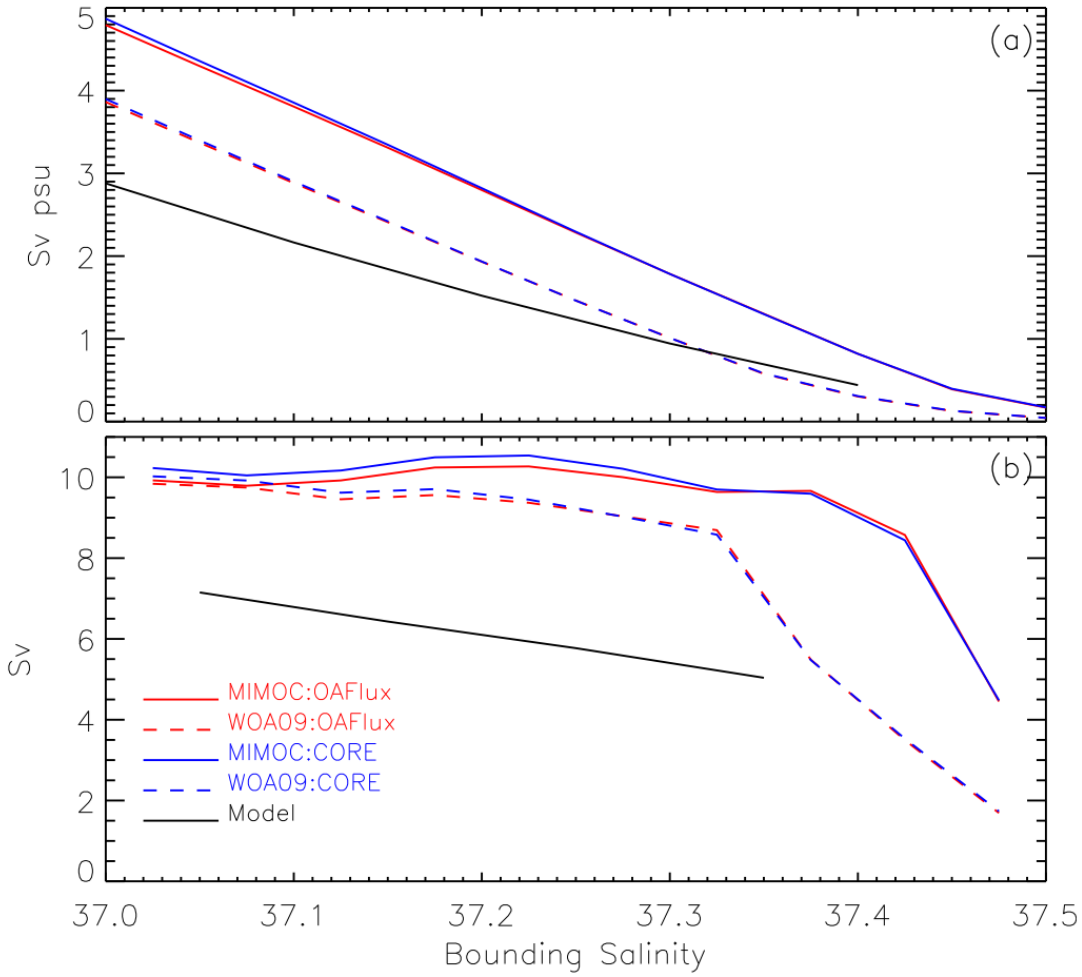

Figure 3.4: (a) Annual-mean surface forcing term in (Bryan and Bachman (2014) Eq. 6) evaluated using the MIMOC(solid) and WOA09(dashed) climatologies with the OAFlux and GPCP surface flux climatology (red) or CORE surface fluxes (blue). (b) Water mass transformation rate due to surface flux terms in (a) computed from (Bryan and Bachman (2014) Eq. 8). FIG. Reproduced from Bryan and Bachman (2014) Figure 11

the right hand side of Equation 3.9 and 3.11 in salinity space and dividing them similar to Equation 3.12.

Results are shown in Table 3.2 as SFC_S. Furthermore we evaluated all results on the reference salinities from Johnson et al. (2016) (Table 3.2; gray columns). For each basin except the SI, the difference in the various SFC values is 5% or smaller, a minor difference considering the spread in regional results from previous studies (e.g. 10-50% SFC in the NA). We will discuss possible reason for the wide range of results below.

Some similarities emerge: The SP SSS-max has the weakest eddy mixing contribution both for the mixed layer and the full isohaline volume. Our results using the SFC based on the volume budget as well as the full depth results from Johnson et al. (2016) suggest that the largest contribution by eddy mixing is found in the SI. Results for alternative reference salinities might be biased since the area within the isohaline could be leaving the regional boundary in our study (see Appendix).

The remaining basins differ in their ranking depending on the metric used. It should not come as a surprise that not all basins compare well in both studies, as the comparison is between eddy mixing estimates for the mixed layer only versus the full depth isohaline volume. Assuming the results are indeed comparable, despite the aforementioned reasons, one can estimate a crude ratio of SFC between the mixed layer and the interior by comparing the SFC values to each other (Table 3.2; last row). The ratio varies from 22% up to 37%. Given the small surface area of the lateral mixed layer boundary compared to the surface of the subsurface isohaline volume this might indicate a significant depth dependency of the lateral eddy mixing - strong in the mixed layer and comparably weak in the interior. Further research has to show to what degree these studies are actually comparable and if these findings can be confirmed from independent estimates.

Besides the choice of control volume, the actual quantification method for F_{Eddy} could matter for the resulting SFC. Gordon and Giulivi (2014) proposed the idea of eddy fluxes as a significant contribution to the salinity/freshwater budget in the North Atlantic SSS-max

region. They estimate the covariance term from SODA reanalysis data by defining the prime terms as the deviation from the zonal average over a box that is approximately 25 degrees wide. This is about 50 times the range of the first Rossby Radius in this area (about 50km (Chelton et al., 1998)), possibly including large scale circulation features in the prime terms. This potentially biases the contribution of eddy mixing by adding some of the long term advective variability. That would explain why this study concludes the highest SFC in the mixed layer of the North Atlantic at around 50%. Our results agree reasonably well with Busecke et al. (2014), who estimated 10%-30% SFC in the NA mixed layer based on the distribution of local divergence of eddy diffusion by using a constant scalar eddy diffusivity and a typical SSS curvature found in a similar box as Gordon and Giulivi (2014). The choice of a "typical" SSS-curvature might effectively mitigate some of the variability caused by the moving SSS-max combined with a fixed control volume.

Basin	NA		SA		NP		SP		SI	
S_{ref}	**37.2**	37.0	**37.1**	37.0	**35.2**	35.2	**36.3**	36.1	**35.8**	35.6
TFR [Sv]	**2.00 (3)**	1.40 (2)	**1.48 (2)**	1.52 (3)	**3.46 (5)**	3.46 (5)	**1.20 (1)**	1.02 (1)	**3.43 (4)**	2.15 (4)
SFC [%]	**19 (4)**	14 (2)	**19 (3)**	18 (5)	**16 (2)**	16 (4)	**10 (1)**	7 (1)	**25 (5)**	15 (3)
SFC_S[%]	**15 (4)**	16 (4)	**17 (5)**	17 (5)	**13 (3)**	13 (2)	**11 (1)**	9 (1)	**11 (2)**	15 (3)
$SFC_{S,FullDepth}$[%]		55 (3)		46 (2)		60 (4)		41 (1)		70 (5)
Mixed Layer vs Interior	**27 (4)**	29 (4)	**36 (5)**	37 (5)	**22 (2)**	22 (1)	**26 (3)**	23 (3)	**16 (1)**	22 (2)

Table 3.2: Mean Results. The columns show the results from the 'MIMOC mean' experiment. In each column (basin) the values are calculated according to the reference salinities from (Gordon et al., 2015) (bold font) and (Johnson et al., 2016) (regular font). The rank for each basin is given in parentheses after the value. From top to bottom: The Transformation rate (TFR); The surface forcing compensation from the volume budget (SFC); The surface forcing compensation from the Salinity budget (SFC_S); The SFC estimate from the salinity budget over the full depth from (Johnson et al., 2016) ($SFC_{S,FullDepth}$) and a comparison between (SFC_S) and ($SFC_{S,FullDepth}$) (Mixed Layer vs. interior). Note that for the last row results are derived for both reference salinities by dividing both values for (SFC_S) by the single results from (Johnson et al., 2016). Please note the bold values in the last row are comparing values where the reference salinities are not equal. For details see text.

3.3.3 Seasonal variability

We find that temporal variability exists in the TFR as well as K_{eff} on various time scales. We focus on the seasonal and interannual signal. In agreement with Bryan and Bachman

(2014) and Johnson et al. (2016), this variability is small compared to the other terms in the volume budget (not shown), namely surface forcing and vertical diffusion. Since these two effects are largely compensating, the eddy mixing can still play an important role for the tendency term in the volume budget of the SSS-maxima. Indeed variations in interannual $TFR_{Eddy,mean}$ are of comparable magnitude as the TFR calculated from the actual change in area from observations (using the same fixed MLD, not shown).

Before we present the results, we begin with a discussion of mechanisms that can cause a temporal variability in the TFR. We will assume that the diffusive flux across the contour is expressed as the product of a mean cross-contour diffusivity K_{eff} and the salinity gradient on the contour $\nabla_l S$ (by definition perpendicular to the contour). As outlined above K_{eff} itself is independent of the background gradient, since it only measures the enhancement of a spatial gradient (which has to be non-zero) by the stirring action of a given velocity field. The resulting flux will scale with both the cross-contour diffusivity as well as the cross contour gradient. Since K_{eff} is the result of the velocities acting on the background fields, and the velocities can vary both in space and time,there are three principal mechanism that could cause temporal variability in TFR. In each basin there is likely a contribution by each of these mechanisms but in the following list we lay out how each mechanism would affect the results in isolation in order to facilitate the identification of the dominant process within the results that follow:

1. Change of K_{eff} due to temporal variability in the velocity field. Assume the velocity field would have spatially homogeneous stirring characteristics which vary with time. All experiment would show coherent variability in both TFR and K_{eff}, since for each experiment the position of the cross-contour gradient is constrained by the reset procedure, hence the diffusivity would control the time evolution of the TFR.

2. Change of K_{eff} due to changes in the position of the contour in a field of spatially variable stirring. Opposite to above now assume a temporally constant stirring action of the velocity field which varies in space instead. All experiments would show

constant TFR and K_{eff}, since for a constrained contour in a single experiment the stirring action resulting in K_{eff} as well as the cross contour gradient would remain 'quasi-constant'. The position of the reference contour varies between each experiment, potentially exposed to other parts of the velocity field. This would cause a spread between experiments in both TFR and K_{eff}.

3. Change in salinity gradient $\nabla_l S$ on the contour. As explained above, single experiments would show no variability in either TFR or K_{eff}, since the gradient is constrained by the reset. Experiments would show constant TFR and K_{eff} as in 2, however the spread between experiments only affects TFR. Contrary to 2 the K_{eff} would remain constant between experiments, since the stirring characteristics and the contour position are identical and K_{eff} is independent from the background gradient (see Section 3.2).

These idealized mechanisms are assuming that any change in gradient or diffusivity along the contour is represented well by a mean value. If strong heterogeneity along the contour occurs the TFR and K_{eff} values shown here within a single experiment could show low temporal coherency, especially when the "along-contour" anomalies of diffusivity and gradient covary.

The left column in Figure 3.6 shows the seasonal cycle for each experiment, separated into ocean basins. The seasonal cycle extracted from the experiments with monthly (gray lines), mean (blue line) initial conditions and the combined (black) experiment are shown. Regional differences in the seasonal cycle are evident. The combined seasonal cycle in the SI and SP is very small or not truly an annual harmonic. In the NA, SA and NP the combined seasonal cycle is of significant size compared to the mean and is shaped close to an annual harmonic with the highest values during the spring of the respective hemisphere. The SI and SP show relatively weak seasonal cycles in $K_{eff,mean}$ (red line), that cannot be related to the TFR_{mean} in a straightforward manner, suggesting increased importance of the local interplay of diffusivities and gradients or simply a non-significant seasonal signal.

We want to focus on the NP and NA in particular as they seem to display two regionally

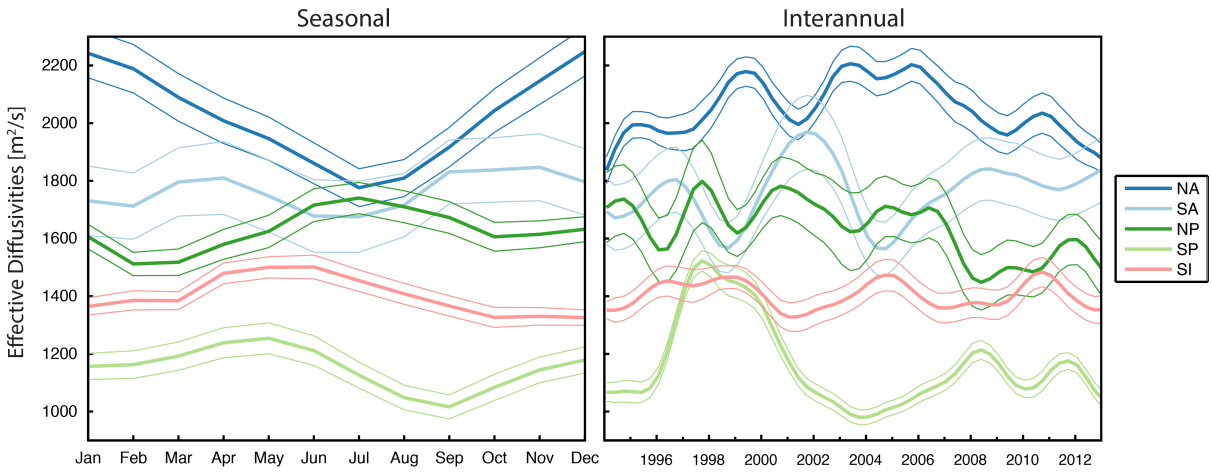

Figure 3.5: Effective diffusivities for S_{ref}. $K_{eff,mean}$ (thick line) and the std of the monthly (left) and annual (right) experiments (indicated by thin lines) are shown for all basins (color) for the seasonal (left) and interannual (right) signal, processed identical to the TFR (see Figure 3.6).

different origins of the combined seasonality related to the idealized scenarios from above. In the NA every experiment with monthly initial condition is exhibiting a very similar seasonal cycle in terms of timing and amplitude. When comparing the K_{eff} values for the NA (Figure 3.5a) the variability is very coherent and larger than the offset between the single experiments. This suggests a local change in diffusivities (mechanism 1 from above) as the leading cause of variability in the NA. The time lag of about a month between $K_{eff,mean}$ and TFR_{mean} in the NA (Figure 3.6a) is an interesting result in itself, which is robust for all experiments (not shown). We interpret the lag as the time between the fast creation of lateral tracer gradient variance (stirring, reflected in K_{eff} which is then slowly digested by small scale diffusion acting on this gradient variance). This yet again illustrates the complex nature of the eddy mixing and the problems which may arise when eddy mixing is diagnosed from methods involving matching of vastly different data sets. Due to the less coherent signals in other basins it is unclear if the length of this lag is the same in every basin.

In the NP the TFR of each experiment seems to be rather constant with a larger offset in between experiments. The K_{eff} values in Figure 3.5a show a similar offset between

experiments as the NA, but in the case of the NP it is not small compared to the annual cycle. Hence it seems likely that a change in diffusivity due to the changing position is responsible for the variability in TFR. This is plausible if we consider the variable position of the NP S_{ref} contour and its vicinity to strong gradients in surface diffusivities (Figure 3.2). We cannot rule out a change in local gradient on the contour as a contribution. It is clear however that in the NP the initial fields of SSS are more important for the variability in eddy mixing than the velocity field, contrary to the NA.

The SA exhibits the largest spread in K_{eff} between experiments. We suggest that this is caused by its unique position in the western boundary current. The SA SSS-max is exposed to strong advection, possibly moving in and out of areas of spatially heterogeneous diffusivities. This does not result in a clear seasonal cycle as in the NA and NP and it is left for further studies to determine whether this large variability remains robust when other processes (as mentioned in the method section) are invoked. We will now apply the same analysis to the interannual signals to investigate if we find evidence for local changes of diffusivites on time scales longer than a year.

3.3.4 Interannual variability

Figure 3.6 (right column) and Figure 3.5 (right) show interannual variability of K_{eff} and TFR.

Similar to the seasonal plots, the gray lines in Figure 3.6, right column, mark each experiment with annual averaged initial conditions, while the $TFR_{annual,combined}$ is shown in black. The combined experiment should be viewed as a check whether various initial conditions can change or compensate the variability imposed by the velocity field.

The character of the longer-term variations is quite different between basins. The NA TFR increases till ca. 2006 and then decreases in a similar fashion. This is consistent with the combined ECCO experiment but the combined ARGO experiment shows an offset which suggests the TFR to stay high in the later part of the record. The SA shows several shorter

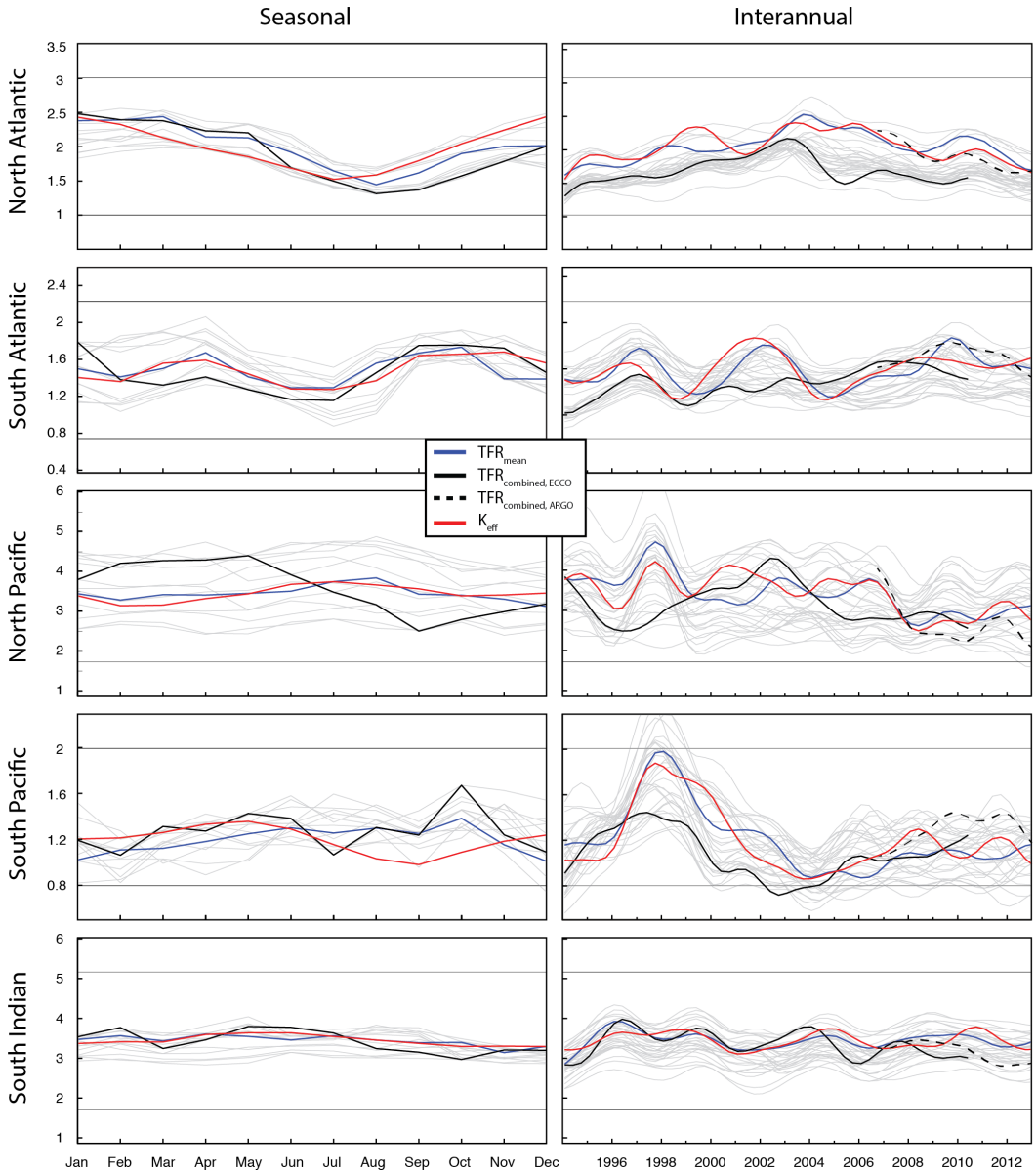

Figure 3.6: Seasonal cycle (left column) and interannual variability (right column) of Transformation Rate [Sv] on S_{ref}. The sign is reversed, with positive values indicating destruction of salty water masses. Colors indicate different experiments (see Table 3.1). Left column: Seasonal cycle. Blue indicates TFR_{mean} black $TFR_{combined}$ and gray lines are all $TFR_{monthly}$ experiments. Right column: interannual record, derived by pre-averaging every 4 months and smoothing with a 1.5 year Gaussian window. Colors as before with gray indicating all experiments with annual initial conditions (Table 3.1). Thick black and dashed black lines indicates $TFR_{combined}$ derived from experiments with annually averaged initial conditions from ECCO and ARGO respectively, for more details see text. K_{eff} (red) is displayed in all plots normalized by the mean and std of TFR_{mean} for comparison.

fluctuations while the longer term seems to be quite steady.

The NP shows an increase in K_{eff} and TFR around 1998 in several experiments. For the SSS-max this seems to be rather irrelevant, since the combined experiment does not capture it. Towards the end of the record the TFR seems to decrease slightly. Similar to the seasonal cycle, the NP shows the largest spread between experiments compared to all other basins, again indicating the possible larger sensitivity to changes in SSS fields compared to the other basins.

The SP shows a strong maximum in $TFR_{annual}/K_{eff,annual}$ in 1998. When the combined experiment is considered, the amplitude is lessened somewhat but the peak remains the largest interannual anomaly in all ocean basins.

The SI again shows very little variability, similarly to the seasonal cycle.

The comparison between the combined experiments from ARGO and ECCO suggests that results in the NA and to a lesser degree in the SP are sensitive to the source of initial conditions. In the SA,NP and SI the records diverge only slightly. Especially for the earlier years of the ARGO record the mismatch might be caused by limited float coverage.

It is worth noting that in the SP (and in many experiments for the NP) the variability in eddy mixing seems to be roughly coincident with the strong El Niño of 1997-1998.

This indicates that large scale environmental processes might be linked to time variable mixing relevant for the subtropical SSS-maxima. The tight distribution of $K_{eff,annual}$ values for the NA and SP suggest that these changes are mainly caused by local changes in diffusivity which appear very coherent in space, affecting most experiments. Even in the NP the high number of experiments showing a peak around 1998 contribute to this idea. The SSS-max might not be impacted by the anomalous velocities, due to an anomalous contour position, but it indicates that diffusivity changes might be happening adjacent to the SSS-max.

These results suggest a link between large scale climate forcing and the eddy mixing in the NA and SP SSS-max via locally changing diffusivities (mechanism 1 from above).

The SA and NP show considerable spread between the K_{eff} values. Similar to the

seasonal interpretation, we conclude that the changing position of the reference isohaline is the dominant driver for the variability in the NP and SA. Both of these basins show larger lateral gradients in surface diffusivities (Abernathey and Marshall, 2013), qualitatively confirming the potential for high variability in diffusivites by changing the position of the reference isohaline.

The SI shows little spread in K_{eff} and little variability in the single experiments. The variability in TFR is also low compared to the other basins. This is particularly interesting since it has arguably the largest contribution of eddy mixing to the budget, while having both a small mean diffusivity and by far the least variability. Local "hot spots" for the eddy mixing (locations where diffusivity and gradient line up locally to dominate the overall TFR) could explain the discrepancy between the high integrated diffusive flux and the low averaged diffusivity.

The following list summarizes the regional "character" (lending from Gordon et al. (2015)) of each basin with respect to the eddy mixing in the surface layer:

- The SP has by far the lowest SFC of all the basins. This is likely due to its unique separation from the western boundary current. The Southern Inter-tropical Convergence Zone shifts the SSS-max far into the eastern part of the basin, prohibiting access to the energetic western region of the basin. The seasonal cycle is very irregular although the amplitude is relatively higher than in the SI in agreement with Gordon et al. (2015) Figure 3. The interannual record shows the strongest signal of all basins with a strong pulse of elevated TFR and K_{eff} around 1998, which is proposed to be related to larger scale climate variability modulating local diffusivities with time.

- The SI is the strongest basin in terms of SFC and TFR but interestingly very low K_{eff} and low temporal variability in eddy mixing, possibly influenced by its unique poleward position in a predominantly zonal mean flow, stabilizing seasonal gradients and possibly suppressing the eddy diffusivities in a region relatively high in EKE (e.g. Klocker and Abernathey (2014)).

- The SA has a similar SFC to the NP and NA and shows a less coherent seasonal cycle in TFR that is similar in magnitude and timing (with a 6 month shift accounting for the hemispheric difference) to the NP and NA. It seems that it represents somewhat of a mixed case in terms of the responsible mechanism (local diffusivity changes vs. monthly SSS fields).

- The NA seems to be largely dominated by local changes in diffusivities both for the seasonal and interannual variability. What exactly renders this mechanism so dominant in the NA is subject to speculation: It might be related to the high lateral salinity gradient (inhibiting strong lateral movement of the reference isohaline) or the relatively low lateral gradient in surface diffusivities which further reduce the influence of a changing isohaline position to the effective diffusivity.

- The NP variability in eddy mixing is strongly dependent on the SSS fields. Both the seasonal cycle as well as interannual variability are shown to be strongly influenced by the position of the reference isohaline, supported by conditions of low lateral SSS gradient and high surface diffusivity gradient. The interannual record shows some indications of a long term change which might be caused by local changes in the diffusivites similar to the SP and NA.

3.4 Conclusions

3.4.1 Relevance for the SSS-maxima in the global ocean

Using diagnostics for eddy diffusivity and integrated diffusive flux in a water mass framework, we documented marked regional differences in the strength, variability and the responsible mechanisms for eddy mixing in the SSS-maxima.

The temporal variability of the eddy mixing is a result of regionally differing mechanisms, dominated by variability in either the velocity field or the surface salinity field: On the one

hand local changes of the eddy field resulting in local diffusivity changes and on the other hand changes in the position of the SSS-maximum in a spatially varying field of surface diffusivities.

The results presented here support the notion of each of the SSS-maxima having his own unique character in eddy mixing, in agreement with the results from Gordon et al. (2015) for the mean position and strength of the seasonal cycle.

We argue that temporal variability of eddy mixing and diffusivities has to be taken into account when constructing salinity budgets in the SSS-max regions. Furthermore the application of results from one SSS-max region (e.g. the well studied NA) to other basins might not be possible. Especially when considering a changing climate, which might influence the mechanisms responsible for temporal variability differently.

3.4.2 Implications for the global water cycle

Regional differences in eddy mixing could have implications for the diagnosis of water cycle changes using the SSS on long time scales. If the common conception of an intensifying water cycle in the future — "saltier regions get saltier and fresh regions become fresher" (Held and Soden, 2006) — holds true, these changes might influence the eddy mixing in each basin differently. For instance, the NP shows the highest sensitivity to changes in the surface salinity. Presumably higher eddy mixing would ensue following the intensification of the lateral salinity gradient by an intensified hydrological cycle, and one could imagine a negative feedback. Of course this would only be valid if the eddy diffusivities remain constant, an assumption that cannot be validated for the relevant time scales (more than 50 yrs (Durack and Wijffels, 2010)) at this point. It seems indeed that the observed decadal pattern intensification in SSS are especially weak/inconsistent in the NP, both for strongly forced model runs as well as historic observations (Figure 3.7). This would be in line with the argument presented above. Further research is needed to investigate this mechanism and its potential importance for the imprint of a changing hydrological cycle on the SSS.

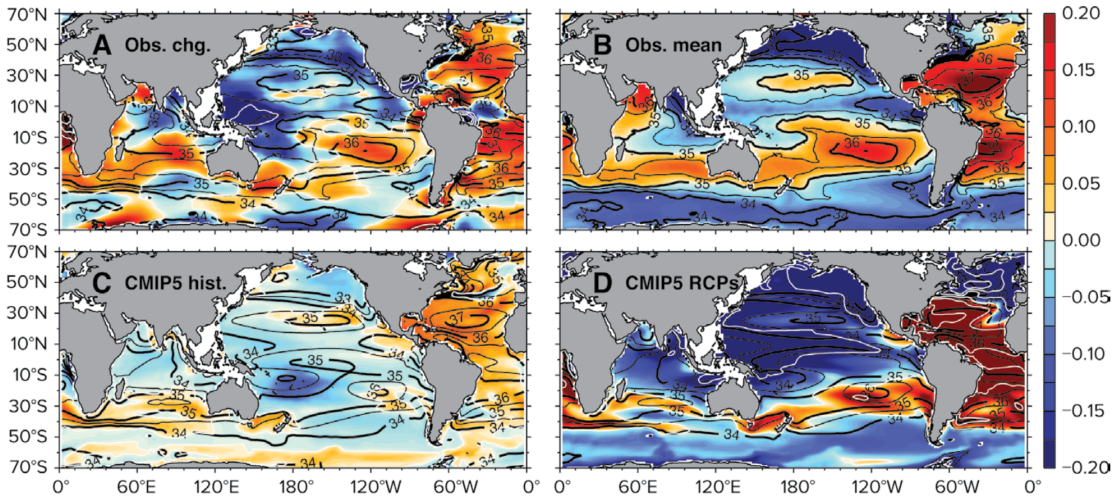

Figure 3.7: Maps of 50-year salinity trends for the near-surface ocean. (A) The 1950–2000 observational change and (B) the correspond- ing 1950–2000 climatological mean of Durack and Wijffels (2010; analysis period 1950–2008). (C) Modeled changes for the 1950–2000 period from the CMIP5 historical experiment MMM (analysis period 1950–1999) and (D) 2050–2099 future projected changes for the most strongly forced RCP85 experiment MMM (analysis period 2050–2099). Black contours bound the climatological mean salinity associated with each map, and white contours bound the salinity trend in increments of 0.25 PSS-78.Reproduced from (Durack, 2015), Figure 7 A/D

3.4.3 Beyond the surface salinity

This study suggests basin scale changes of the local surface diffusivities, potentially affecting areas much broader than the SSS-max. In the case of the South and North Pacific these changes seem connected to large scale climate fluctuations related to ENSO, possibly forming an important climate feedback. To our knowledge such a connection has not been documented using an observationally driven method and could be of relevance to the larger oceanographic and climate science community. A data set of monthly surface diffusivities combining methods from Abernathey and Marshall (2013) and this study will be helpful in identifying locations where eddy diffusivities respond coherently to the large scale environment. Such a data set is in preparation and will be published in a separate manuscript.

3.5 Acknowledgments

We are grateful for the detailed comments from two anonymous reviewers, which greatly improved the manuscript. We also thank Sjoerd Groeskamp, Sloan Coats, Claudia Giulivi and Søren Thomsen for comments on the initial draft. Julius Busecke's research was supported by NASA award NNX14AP29H. Ryan P. Abernathey acknowledges support from NASA award NNX14AI46G. Arnold L. Gordon's research is supported by NASA grant NNX14AI90G to Columbia University. Lamont-Doherty Earth Observatory contribution number XXXX.

Chapter 4

Temporal variability of surface eddy diffusivities in the global ocean from altimetry

4.1 Introduction

Mesoscale velocity fluctuations ('eddies'), are a ubiquitous phenomenon in the global ocean with high importance to the global ocean circulation. Eddy effects are important for the large scale circulation as shown for example for the meridional overturning circulation (Marshall and Speer, 2012; Marshall et al., 2017) and global water mass formation (Groeskamp et al., 2016). One role of eddies in the global ocean circulation is to diffusively mix tracers (heat, salt and anthropogenic carbon) laterally along isopycnals and horizontally at the ocean surface (McCann et al., 1994; Stammer, 1998; Tréguier et al., 2014; Gnanadesikan et al., 2015). Estimates of an eddy diffusivity, which relates the diffusive flux of a tracer to the large scale tracer gradient (as described in detail in Chapter 1) are a matter of a longstanding debate in the literature. Due to the small scale and the turbulent nature of eddy flow it is necessary to obtain long time statistics with high spatial resolution, which to date remain challenging to

obtain. This problem is particularly important when measurements of collocated variables, like velocity and tracer measurements, are required to infer eddy statistics. To address this problem we use an observation-driven surface model experiment combining velocities from altimetry and several tracer fields to diagnose lateral eddy diffusivites near the sea surface. The diffusivities exhibit strong temporal variability in most ocean basins, with interannual variability ranging from 20% to over 300% of the local average in a majority of the global ocean. Correlation with the ENSO index in large parts of the Pacific basins is observed, suggesting a modulation of surface eddy diffusivities by large-scale climate fluctuations. This may constitute a climate feedback mechanism previously unaccounted for in global climate models. Our study demonstrates how the complex surface velocity field modulates lateral surface mixing in the world ocean. We anticipate that the monthly data set of surface diffusivities will be valuable for the testing and development of future parametrization for eddy effects in coarse resolution models.

4.2 Methods

4.2.1 Model Setup

Our experiments are conducted in an idealized surface setup of the MITgcm (Marshall et al., 1997). The horizontal resolution is 0.1 degree on a regular lon/lat grid. Surface initial conditions from observations (see main text) are padded with nearest neighbor values, linearly interpolated onto the model grid and advected with observed absolute geostrophic surface velocities from AVISO (AVISO DUACS2014; produced by Ssalto/Duacs and distributed by Aviso, with support from Cnes (http://www.aviso.altimetry.fr/duacs/).

The velocity fields are padded with zero and linearly interpolated onto the model grid. To extend the velocity record as far as possible, the delayed time product is supplemented with the near real time product after May 2016, extending the record from January 1993 until January 2017. The major results discussed in the manuscript occur in the time frame

when the highest quality velocity product was used. Additional to prior studies using this specific setup (Abernathey and Marshall, 2013; Busecke et al., 2017) we use velocities with daily resolution as provided by the DUACS14 product. In order to conserve a passive tracer under two dimensional advection, the velocity fields needs to be divergence free. Aviso velocities are not strictly divergence free, due to velocity approximations made near the equator and non-zero velocities perpendicular to the coast. For these experiments the velocities are 'divergence corrected' by decomposing the velocity field into the sum of a non divergent streamfunction and velocity potential (Helmholtz decomposition) (Marshall et al., 2006; Abernathey and Marshall, 2013). The latter is subtracted from the interpolated velocity fields. This correction is usually small compared to the raw velocities except near the equator and the coast. The ratio of the correction term to the velocities is typically $O(0.1)$ within the basins (Abernathey and Marshall, 2013). Figure 4.1 shows the magnitude of the velocity speed error and the standard deviation of the uncorrected velocities. The error due to the divergence correction seems only relevant in the coastal areas and near the equator.

The model solves the two dimensional advection-diffusion equation

$$\frac{\partial q}{\partial t} + \mathbf{v} \cdot \nabla q = \kappa \nabla^2 q \tag{4.1}$$

for the passive tracer field q with a constant small-scale (grid-scale) diffusivity of $\kappa = 25 m^2/s$. A numerically diffusive advection scheme is used which causes the effective grid-scale diffusivity to be higher. Abernathey and Marshall (2013) diagnose a constant 'combined' diffusivity using the globally averaged tracer variance budget

$$\frac{\partial}{\partial t} \iint \frac{q^2}{2} = -\kappa_{num} \iint |\nabla q|^2 \tag{4.2}$$

They diagnose $\kappa_{num} = 63 m^2/s$, which will be used as the value for κ throughout the rest of the manuscript.

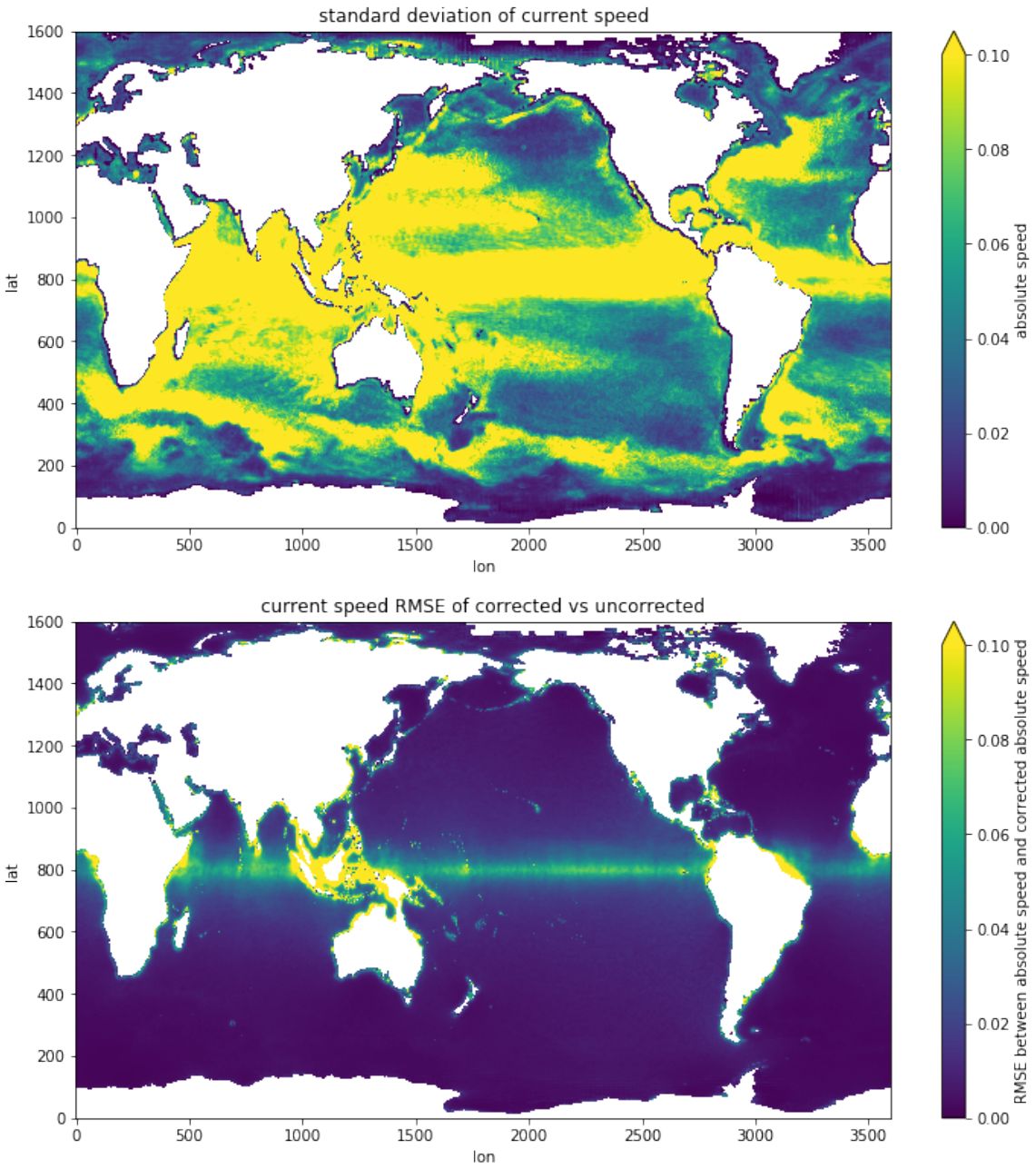

Figure 4.1: Visualization of the velocity speed error introduced by the divergence correction (see above). **Upper)** Standard deviation of uncorrected velocities from Aviso (details, see Methods) in $[m/s]$. **Lower)** Root Mean Square Error based on the difference between the uncorrected and divergence corrected velocities in $[m/s]$

4.2.2 Osborn Cox Diffusivity

To infer lateral surface diffusivities from an instantaneous tracer field we use the Osborn Cox Diffusivity K_{OC} , which represents the local down-gradient eddy flux associated with irreversible mixing (Osborn and Cox, 1972).

$$K_{OC} = \kappa \frac{\overline{|\nabla q'|^2}}{|\nabla \overline{q}|^2} \tag{4.3}$$

With q as an arbitrary tracer field and the prime/overbar representing the deviation/average with respect to the diagnostic averaging time (30 days) and the spatial coarsening interval of 2deg by 2 deg(coarsened grid cells with any land in it are masked from the final results).

Physically K_{OC} represents the local enhancement of the small scale diffusivity κ. The ratio $\frac{\overline{|\nabla q'|^2}}{|\nabla \overline{q}|^2}$ can be interpreted analogous to the ratio of length scales of the 'effective diffusivity' by (Nakamura, 1996) (described in detail in Chapter 3), with large variance in the gradient of the lateral tracer anomaly representing a highly filamented tracer field. Mixing is however, not a purely local process, and contrary to 'effective diffusivity' the advection of tracer variance is neglected here. Previous studies have shown that the advection of tracer variance (as diagnosed from the full tracer variance budget) is of secondary importance when interpreting large scale features, hence the Osborn-Cox diffusivity represents a reasonable overall eddy diffusivity (Abernathey and Marshall, 2013). For large local curvature in the tracer field diffusivity values are masked following the procedure described in Appendix B2.

4.2.3 Resolving temporal variability

A previous study using this methodology has focused on the spatial variability of the long-term mean (Abernathey and Marshall, 2013). Using a different diagnostic but identical model setup, Busecke et al. (2017) documented significant temporal variability in eddy diffusivities in the subtropical basins, where the maximum surface salinity is located. Their methodology provides integral values for tracer contours and is not able to localize such variability in space.

In order to resolve spatio-temporal variability in this manuscript we will combine some of the methods from both studies cited above: For each experiment (defined by the initial tracer field q_0), we compute two passive tracers simultaneously and reset each tracer with equal and regular time intervals (13 months) but the reset phase of one tracer is shifted by half a reset interval, similar to (Busecke et al., 2017). After that each of the respective reset points the initial spin-up phase (3 months) is removed due to the dominating role of the tendency term in the tracer variance budget (for details see (Abernathey and Marshall, 2013; Busecke et al., 2017)). For each initial tracer q we average the diagnosed diffusivity from both tracers and call it $K_{OC,q}$. The deviation between both tracers in each experiment is generally much smaller than the average diffusivity (see B.1). Specifically the fluctuations discussed in this manuscript are much larger than any potential effect of the averaging procedure.

4.3 Results and Discussion

As discussed previously, the spatial distribution of K_{OC} depends on the initial tracer field q_0, indicating the anisotropy in the full diffusivity tensor (Abernathey and Marshall, 2013). We compute the diffusivities for 4 experiments with different initial conditions q_0 :

- $K_{OC,LAT}$ Linear function of the latitude
- $K_{OC,PSI}$ Streamfunction for the mean flow , based on Aviso altimetry fields.
- $K_{OC,SST}$ Mean Climatological Sea Surface Temperature (SST) (Schmidtko et al., 2013)
- $K_{OC,SSS}$ Mean Climatological Sea Surface Salinity (SSS) (Schmidtko et al., 2013)

Results from these experiments mostly differ in the form of offsets between tracers, while temporal variability is very coherent on interannual and longer time scales (see Figure B.2). This suggests that the temporal diffusivity changes are dominated by the velocity fields which are derived from observations. Nonetheless absolute values of diffusivity differ largely. This is likely a consequence of diagnosing a scalar diffusivity, which is relevant for the tracer

advected, but does not represent the full diffusivity tensor. As discussed in Chapter 1 tracer transport across fronts is usually dominated by eddy mixing, since advective transports are often aligned with frontal features, making the 'cross-frontal' diffusivity relevant to water mass transformations. We exploit the different geometry of each tracer field, assuming that each result represents the projection of the two principal axes of the diffusivity tensor. Hence we compute a minimum diffusivity K_{min} across all experiments, by choosing the K_{OC} time series of the experiment with the lowest time averaged diffusivity at every grid point. K_{min} is interpreted as the 'cross-frontal' diffusivity. A corresponding uncertainty estimate is described in Appendix B1

An earlier study, using the same diagnostic as in this study, has documented large spatial variability in time averaged surface diffusivities (Abernathey and Marshall, 2013), suggesting lateral differences extending over several orders of magnitude. The western boundary currents show diffusivities up to several $10^3 m^2/s$ while diffusivities on the order of $10^2 m^2/s$ are found in the subtropical gyres. This structure is generally confirmed by other observation based estimates in the ocean interior (Cole et al., 2015) and correspond well with the results presented here (Figure 4.2 upper left and center)

Numerical model studies have documented that changing the constant diffusivity in an eddy parametrization can have strong impacts on the meridional overturning circulation (Marshall et al., 2017), and that spatially variable diffusivities are required for realistic water mass formation rates e.g. in the Southern Ocean (Groeskamp et al., 2016) and affect the distribution of tracers in the ocean, for instance for the uptake of anthropogenic carbon (Gnanadesikan et al., 2015).

We hypothesize that temporal variability in diffusivity, if sufficiently large, could have similarly strong implications for the global ocean circulation. Motivated by a study of the global sea surface salinity maxima, suggesting large scale increase of surface diffusivities in the subtropical gyre of the South Pacific (Busecke et al., 2017) during the 1997/1998 El Niño, we investigate temporal variability in surface diffusivities globally with a focus on the

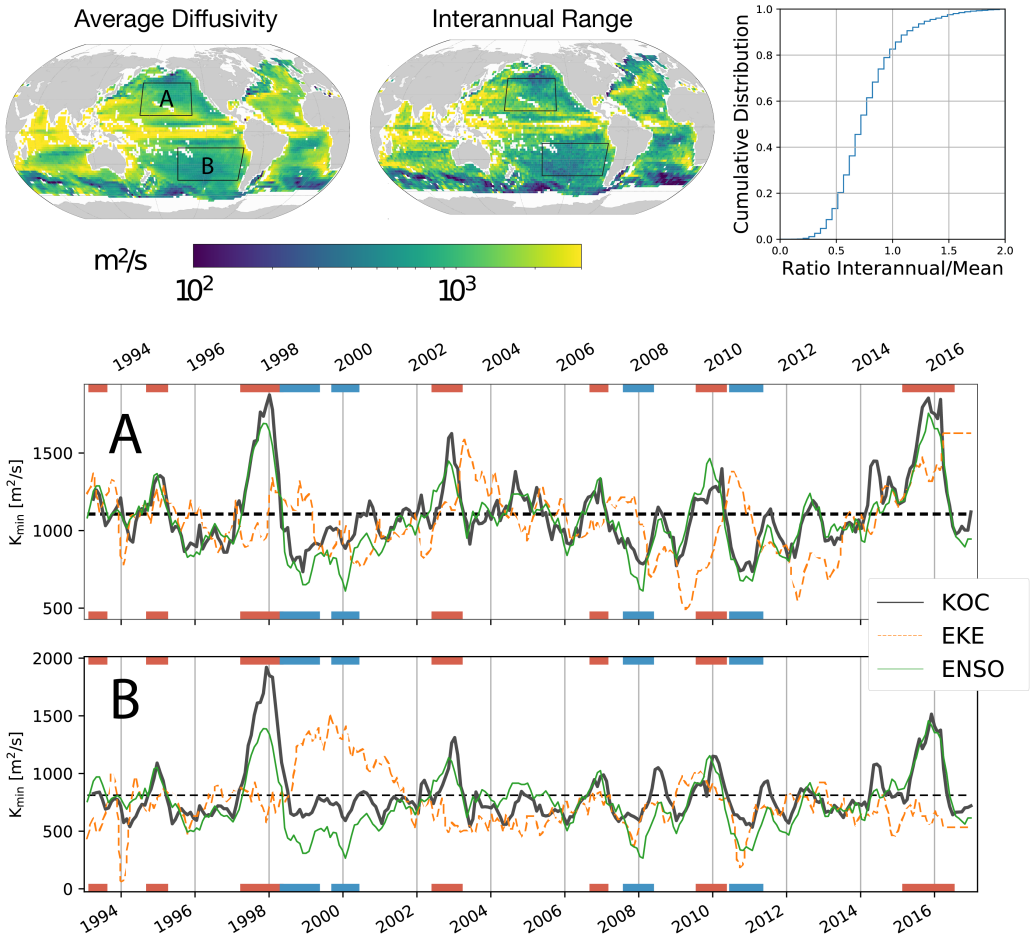

Figure 4.2: K_{min} results. **upper left)** Mean K_{min}. **upper center)** Interannual range of K_min, defined as the difference between 15th and 85th percentile of annual averages. **upper right)** Cumulative histogram of ratio of interannual range over average diffusivity. **center and lower)** timeseries of diffusivity averaged within boxes indicated in upper left and center maps. Gray line indicated averaged K_{min}, the green line the scaled NINO3.4 index and the orange line the scaled EKE with the seasonal cycle removed. Red and blue markers indicate times categorized as 'El Nino'/'La Nina' used for composites in Figure 4.3

Pacific subtropical basins.

The annual range of K_{min} resembles the spatial structure of the mean (Figure 4.2 upper left and center). High variability $O(10^3 m^2/s)$ is found in the equatorial regions, the western boundary current extensions and parts of the Indian Ocean. The subtropical and subpolar basins show lower variability $O(10^2 m^2/s)$. To further evaluate the importance of the temporal variability, we compare the temporal standard deviation to the mean value (Figure 4.2 upper right). In over 80% of the global ocean the interannual range is larger then 50% of the mean diffusivity with many areas reaching much higher values, exceeding the magnitude of the local mean in areas like the eastern subtropical Pacific, in parts of the western/central tropical Pacific and parts of the Indian Ocean. This confirms that temporal variability in surface diffusivities might be of similar impact to the large scale circulation as spatial variability.

Fig 4.2 shows time series of example regions located in the subtropics of the Pacific. Interannual variability shows regional differences, but generally contains low frequency components and strong peaks. Particularly the Pacific basins show strong correlation between the surface diffusivity and the NINO3.4 index (Reynolds et al., 2002) (Figure 4.2), confirming results of a previous study using a different methodology (Busecke et al., 2017). Both Pacific basins show increases in K_{min} within a few months after positive El Niño Southern Oscillation (ENSO) events. The peaks of K_{min} are especially pronounced during the strong El Niño of 1997/98 and 2015/16. The diffusivities within the large box in the South Pacific show values two times as strong as the approximate baseline in early 1998. The North Pacific shows a particular strong response in early 2016, with a doubled surface diffusivity throughout the large scale box. During the negative ENSO phases diffusivities are generally low in the Pacific boxes, but they do not show as strong of a response as during positive phases. This behavior is more pronounced in the South Pacific, which has the lowest average diffusivities.

Figure 4.3 shows the spatial extent of anomalies occurring simultaneously to ENSO

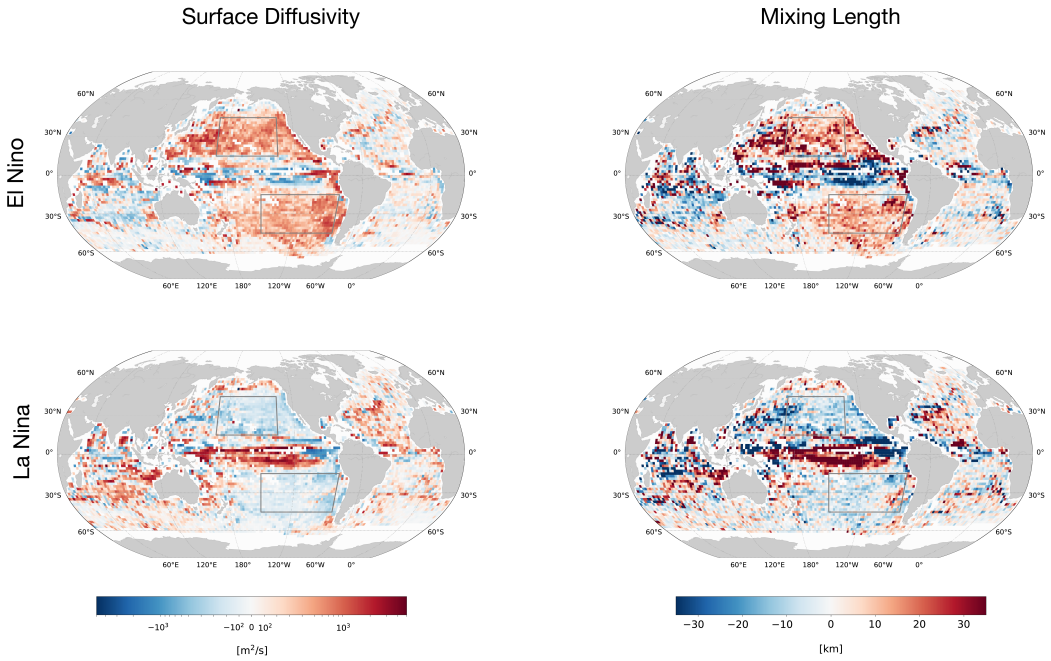

Figure 4.3: ENSO composites. **upper row)** Composites for NINO3.4 larger than 1 deg C. Indicated by red markers in Figure 4.2. **lower row)** Composites for NINO3.4 smaller than -1 deg C. Indicated by blue shading in Figure 4.2. **left column)** Composite of K_{min} anomaly from temporal mean. **right column)** Composite of L_{mix} anomaly from temporal mean. For details see text.

events, by compositing surface diffusivities during high and low NINO3.4 periods. During positive events an increase of several hundred m^2/s can be observed throughout the subtropical basins in the Pacific. Changes in the tropics are even higher. Yet they do not represent such a strong change compared to the mean, which is very high in the tropics. A clear pattern emerges over all of the subtropical Pacific with signals during positive ENSO phases close to 100% of the mean in the central and eastern basin.

These findings indicate that changes in the surface velocity field, leading to a basin wide increase in lateral surface diffusivity, are modulated by large-scale climate fluctuations. To our knowledge, this has not been shown before, especially not from an estimate based on observations. Changes of this magnitude and spatial extent could have significant consequences for the distribution of water masses and the ocean circulation near the surface, since

the amplitude of the anomalies is similar to the range of sensitivity studies that find large differences in circulation pattern and tracer dispersion (e.g. (Gnanadesikan et al., 2015; Marshall et al., 2017)).

Two important, and connected, questions arise from these observations: First, which characteristic of the velocity field is causing observed changes in surface diffusivity? And secondly which physical process could couple the tropical sea surface temperatures (ENSO) to such changes? To answer these questions in depth is outside of the scope of this study. We will however briefly discuss an obvious candidate for the former: It seems that a stronger eddy kinetic energy (EKE), is not the reason increased diffusivities are observed during positive ENSO events, at least not in the Pacific. Figure 4.2 shows very little relation between the time series of EKE and K_{min}.

This suggests that more complex interaction between large scale velocity changes and the eddy field might have a first order influence on the variability of K_{min}, while the EKE on its own still plays a role but it might be of second order. We hypothesize diffusivity suppression by large scale velocity anomalies to play a leading role in modulating surface velocities (Ferrari and Nikurashin, 2010; Klocker and Abernathey, 2014). This can be supported by the spatial pattern of the diagnosed mixing length L_{mix} (Figure 4.3 left column). For an arbitrary tracer c L_{mix}, which indicates the distance over which a water parcel preserves its characteristics before they mix with the sourroundings is calculated as follows:

$$L_{mix} = \frac{\sqrt{\frac{(c')^2}{2}}}{|\nabla \overline{c}|} \tag{4.4}$$

These results suggest a modulation of the mixing length due to the interaction of the eddy field with the large scale flow. Previous work on surpressed mixing length theory (Ferrari and Nikurashin, 2010; Klocker and Abernathey, 2014) would suggest that one of the following parameters changes due to large scale climate fluctuation, which could explain the strong changes in diagnosed surface diffusivity:

- The size of the most energetic eddies
- The large scale variations of the surface velocities
- The depth averaged velocity, which is important for the doppler-shifted phase speed of the eddies

The influence of the interaction between eddy field and time variable mean flow has to be explored in a more comprehensive way. A separate manuscript, building on the existing work on eddy-meanflow interaction is in preparation.

4.4 Conclusions

This study focuses on providing a novel data set of surface diffusivities and present evidence for the connection between surface diffusivites and large scale climate indicies. This could present an important climate feedback which is not represented in state-of-the-art climate models. Our results provide needed observation based estimates of spatio-temporal variability which should be used to inform and test future parametrization for the effects of mesoscale eddies in coarse scale climate models.

An additional open question is if this variability extends significantly below the surface layer. This needs to be investigated in future eddy resolving model studies, since subsurface observations lack the resolution and record length of subsurface velocities, making a similar study based on observations difficult.

Chapter 5

Conclusions

The goal of this thesis was to investigate the impact of eddy mixing on tracer transports in the near-surface ocean with a focus on the subtropical ocean. Using several diagnostics to investigate the variability of irreversible mixing induced by the mesoscale velocity field underline the importance of temporal variability in eddy mixing for the upper ocean.

Chapter 2 provided high resolution surveys of fresh filaments in the central subtropical Atlantic, confirming the importance of eddy fluxes, previously proposed (Gordon and Giulivi, 2014) for the SSS, from an observational viewpoint. It served as a motivation to investigate the importance of eddy mixing to the surface salinity budget. Furthermore it pointed out the watermass characteristics of the surface and subsurface water masses, which will be further discussed below.

Chapter 3 and 4 suggest that the variability in surface diffusivities is especially relevant in the subtropics, due to the generally low lateral surface diffusivities in these regions. This has general implications for studies investigating processes that affect the SSS, particularly for studies using a mixed layer budget in regions of high SSS (e.g. SPURS). The global results however also suggest high variability in the fresh tropical regions, where the second stage of SPURS is currently being carried out.

The work presented in this thesis implies that eddy mixing has a large impact on the

distribution of tracers like SSS and SST, and hence on the watermasses which are subducted in the shallow overturning circulation. It is implied that for budget studies of surface salinity, eddy mixing can not be neglected as a minor term. Furthermore the work presented here suggests significant temporal variability in the transformation rate by eddy mixing in the high salinity regions of the global ocean. This has to be taken into account when constructing surface budgets. Special care has to be applied when interpreting other terms as a residual from the budget, since temporal variability in eddy mixing is of significant size compared to the mean budget in most SSS-maxima and could project onto these. This is particularly true when budgets are constructed from different data sources with large errors. I suspect that a more careful treatment of eddy mixing in budget analysis can, at least to a degree, resolve some of the apparent discrepancies between studies in the SPURS region (Lindstrom et al., 2015). When comparing results between models, in situ measurements and remotely sensed fields a careful analysis of resolved scales is necessary to achieve comparability between results. Particularly when dealing with partially or fully 'eddy resolving' products e.g. the output of SMOS, Aquarius and SMAP satellites it is important to appropriately separate the large scale from eddy scales. Firstly eddy diffusivities can not readily be applied to these fields since they already contain direct signatures of mesoscale features, greatly enhancing the lateral gradients and subsequently the inferred tracer flux. Secondly when eddy effects are resolved, covariance fluxes (more precisely the prime terms in Eq. 1.5) have to be defined on the appropriate scales.

This thesis documents overall strong heterogeneity in eddy mixing characteristics between different ocean basins. This extends the notion of Gordon et al. (2015), that each SSS-max has its own 'personality'. It seems likely that the position of each SSS-max and the general setup of the basins plays a large role in determining the specific mechanism that are responsible for the mean state and observed variability. This again emphasizes the potential for each basin to react differently to a changing climate and exhibit different internal variability characteristics that need to be understood in detail to improve future climate

projections, especially due to the importance of the SOC to ocean heat and anthropogenic carbon uptake.

The results in Chapter 4 extend the importance of temporal variability in surface diffusivities globally. The temporal variability is large in most regions of the global ocean, and I presented evidence that suggests a connection between large scale climate variability and surface diffusivities. The magnitude of temporal variability and the suspected connection to large scale climate variability can be of large importance to the climate system. Such a connection could effectively dampen changes in the surface induced by ENSO, by mixing away any anomalies before they propagate to the interior. These anomalies could include upper ocean heat and salt content as well as other relevant tracers which change in the subtropics in conjunction with ENSO. It seems that from a kinematic viewpoint changes of EKE are not the main driver of variability in diffusivities, which leaves the interaction of the larger scale velocities with the eddy field to explain the observed enhancements in eddy mixing during positive ENSO phases. It is imperative to further investigate mechanisms responsible as well as possible differences in the time scale they react to a large change in the tropical Pacific. If the time scale is similar to the time scale of occurrences, it is plausible that surface anomalies might just be dampened. However, if the timing is offset this could result in quite a different effect for the climate system, which needs to be explored further.

In this context a necessary step would be to develop eddy parametrization which reproduce the observed variability in diffusivity, requiring knowledge of the processes modulating surface diffusivities. The data set provided with Chapter 4 will be useful in

1. Identifying responsible physical processes coupling ENSO, and large scale climate variability in general, to changes in surface diffusivities

2. Evaluating the interplay between diffusivities and surface tracers varying on an interannual basis, with a focus on the changes during ENSO events. Chapter 3, indicates that changes in the SSS field partially compensate the change in diffusivities with regard to the integrated diffusive salt flux out of the SSS-main the South Pacific. However, due

to the method used the results are limited to the saltiest regions of the subtropics.

3. Testing the ability of future parametrization to reproduce the correct spatio-temporal structure of the diffusive transfer coefficient at the surface.

5.1 Future Work

My future work will focus on the identification of the responsible mechanisms for the observations in Chapter 4. I will specifically investigate the mechanism of suppression of eddy diffusivities by mean flow (Ferrari and Nikurashin, 2010; Klocker and Abernathey, 2014). This will include studying eddy resolving model output to compare the variability in lateral surface diffusivity and mechanisms responsible.

Subsequently I plan to focus on a more complete investigation of the influence of mixing processes on the transports in the SOC. This will involve studying the subsurface. I plan to explore the vertical structure of variability in lateral diffusivities as well as the associated diapycnal diffusivities. An additional point of interest about the tracer distribution in the SOC was briefly discussed in Chapter 2. The subsurface salinity maximum is shifted to lighter densities along the subduction path, which could be indicative of vertically increasing diapycnal diffusivities. My future work will investigate if processes like double diffusion Zhang et al. (1998) or remote tidal mixing (Melet et al., 2016) are essential in reproducing the observed distribution of the water masses subducted in the SOC. Of special interest is the role of double diffusion which supposedly affects the Atlantic more than the Pacific, due to the higher vertical salinity gradient in the thermocline (Schmitt, 1994). Can surface signatures of a warming climate, particularly an intensified SSS pattern (Durack, 2015) be dampened by double diffusion when subducted to depth as suggested by (Johnson and Kearney, 2009).

I suggest the work presented in this thesis and the proposed work will contribute to the process understanding of lateral eddy mixing in the ocean as well as the representation of

these processes in future climate models, which in turn could improve the internal and forced variability characteristics of future climate projections.

Bibliography

Abernathey, R. P., Marshall, J., 2013. Global surface eddy diffusivities derived from satellite altimetry. Journal of Geophysical Research: Oceans 118 (2), 901–916.

Abernathey, R. P., Marshall, J., Mazloff, M., Shuckburgh, E., Mazloff, M., Shuckburgh, E., 1 2010. Enhancement of Mesoscale Eddy Stirring at Steering Levels in the Southern Ocean. dx.doi.org 40 (1), 170–184.

Amores, A., Melnichenko, O., Maximenko, N., 12 2016. Coherent mesoscale eddies in the North Atlantic subtropical gyre : 3D structure and transport with application to the salinity maximum . Journal of Geophysical Research: Oceans, 1–45.

Bachman, S. D., Fox-Kemper, B., Bryan, F. O., 2015. A tracer-based inversion method for diagnosing eddy-induced diffusivity and advection. Ocean Modelling 86 (1), 1–14.

Beal, L. M., De Ruijter, W. P. M., Biastoch, A., Zahn, R., others, 2011. On the role of the Agulhas system in ocean circulation and climate. Nature 472 (7344), 429–436.

Bingham, F. M., Busecke, J., Gordon, A. L., Giulivi, C. F., Li, Z., 11 2014. The North Atlantic subtropical surface salinity maximum as observed by Aquarius. Journal of Geophysical Research: Oceans 119 (11), 7741–7755.

Bingham, F. M., Foltz, G. R., McPhaden, M. J., 2012. Characteristics of the seasonal cycle of surface layer salinity in the global ocean. Ocean Science 8 (5), 915.

Blayo, E., Debreu, L., 6 1999. Adaptive Mesh Refinement for Finite-Difference Ocean Models: First Experiments. J Phys Oceanogr 29 (6), 1239–1250.

Boccaletti, G., Ferrari, R., Adcroft, A., Ferreira, D., Marshall, J., 5 2005. The vertical structure of ocean heat transport. Geophysical research letters 32 (10), L10603.

Boutin, J., Chao, Y., Asher, W. E., Delcroix, T., Drucker, R., Drushka, K., Kolodziejczyk, N., Lee, T., Reul, N., Reverdin, G., Schanze, J., Soloviev, A., Yu, L., Anderson, J., Brucker, L., Dinnat, E., Santos-Garcia, A., Jones, W. L., Maes, C., Meissner, T., Tang, W., Vinogradova, N., Ward, B., 2016. Satellite and in situ salinity understanding near-surface stratification and subfootprint variability. Bulletin of the American Meteorological Society 97 (8), 1391–1407.

Bryan, F., Bachman, S., 12 2014. Isohaline salinity budget of the North Atlantic salinity maximum. dx.doi.org 45 (3), 724–736.

Busecke, J., Abernathey, R. P., Gordon, A., 2017. Lateral Eddy Mixing in the subtropical salinity maxima of the global Ocean. Journal of Physical Oceanography.

Busecke, J., Gordon, A. L., Li, Z., Bingham, F. M., Font, J., 1 2014. Subtropical surface layer salinity budget and the role of mesoscale turbulence. Journal of Geophysical Research: Oceans 119 (7), 4124–4140.

Cessi, P., 8 2007. Regimes of Thermocline Scaling: The Interaction of Wind Stress and Surface Buoyancy. J Phys Oceanogr 37 (8), 2009–2021.

Charney, J. G., 10 1947. The Dynamics of Long Waves in a Baroclinic Westerly Current. Journal of Meteorology 4 (5), 136–162.

Chelton, D. B., DeSzoeke, R. A., Schlax, M. G., El Naggar, K., Siwertz, N., 3 1998. Geographical Variability of the First Baroclinic Rossby Radius of Deformation. J Phys Oceanogr 28 (3), 433–460.

Cole, S. T., Wortham, C., Kunze, E., Owens, W. B., 2015. Eddy stirring and horizontal diffusivity from Argo float observations: Geographic and depth variability. Geophysical Research Letters 42 (10), 3989–3997.

Curry, R., Dickson, B., Yashayaev, I., 1 2003. A change in the freshwater balance of the Atlantic Ocean over the past four decades. Nature.

Durack, P. J., 2015. Ocean Salinity and the Global Water Cycle. Oceanography 28 (1), 20–31.

Durack, P. J., Wijffels, S. E., 8 2010. Fifty-Year Trends in Global Ocean Salinities and Their Relationship to Broad-Scale Warming. Journal of Climate 23 (16), 4342–4362.

Entekhabi, D., Njoku, E. G., O'Neill, P. E., Kellogg, K. H., Crow, W. T., Edelstein, W. N., Entin, J. K., Goodman, S. D., Jackson, T. J., Johnson, J., others, 2010. The soil moisture active passive (SMAP) mission. Proceedings of the IEEE 98 (5), 704–716.

Fairall, C. W., Bradley, E. F., Rogers, D. P., Edson, J. B., Young, G. S., 1 1996. Bulk parameterization of air-sea fluxes for Tropical Ocean-Global Atmosphere Coupled-Ocean Atmosphere Response Experiment. Journal of Geophysical Research: Oceans (1978–2012) 101 (C2), 3747–3764.

Farrar, J. T., Rainville, L., Plueddemann, A. J., Kessler, W. S., 1 2015. Salinity and temperature balances at the SPURS central mooring during fall and winter. Oceanography.

Ferrari, R., Nikurashin, M., 7 2010. Suppression of Eddy Diffusivity across Jets in the Southern Ocean. Journal of Physical Oceanography 40 (7), 1501–1519.

Font, J., Camps, A., Borges, A., Martin-Neira, M., Boutin, J., Reul, N., Kerr, Y. H., Hahne, A., Mecklenburg, S., 1 2010. SMOS: The Challenging Sea Surface Salinity Measurement From Space 98 (5), 649–665.

Forget, G., Campin, J. M., Heimbach, P., Hill, C. N., Ponte, R. M., 1 2015. ECCO version 4: an integrated framework for non-linear inverse modeling and global ocean state estimation. Geoscientific Model Development Discussions 8 (5), 3653–3743.

Fox-Kemper, B., Ferrari, R., 1 2008. Parameterization of mixed layer eddies. Part II: Prognosis and impact. Journal of Physical Oceanography.

Fox-Kemper, B., Ferrari, R., Hallberg, R., 6 2008. Parameterization of Mixed Layer Eddies. Part I: Theory and Diagnosis. J Phys Oceanogr 38 (6), 1145–1165.

Fox-Kemper, B., Lumpkin, R., Bryan, F. O., 2013. Lateral transport in the ocean interior. Ocean Circulation and Climate: A 21st century perspective 103, 185–209.

Gnanadesikan, A., Pradal, M.-A., Abernathey, R. P., 6 2015. Isopycnal mixing by mesoscale eddies significantly impacts oceanic anthropogenic carbon uptake. Geophysical Research Letters 42 (11), 4249–4255.

Gordon, A., Giulivi, C., 3 2008. Sea Surface Salinity Trends over Fifty Years Within the Subtropical North Atlantic. Oceanography 21 (1), 20–29.

Gordon, A. L., 1986. Interocean exchange of thermocline water. Journal of Geophysical Research: Oceans 91 (C4), 5037–5046.

Gordon, A. L., 1 2016. The marine hydrological cycle: The ocean's floods and droughts. Geophysical research letters.

Gordon, A. L., Giulivi, C. F., 1 2014. Ocean eddy freshwater flux convergence into the North Atlantic subtropics. Journal of Geophysical Research 119 (6), 3327–3335.

Gordon, A. L., Giulivi, C. F., Busecke, J., Bingham, F. M., 2015. Differences among subtropical surface salinity patterns. Oceanography 28 (1), 1–30.

Gordon, A. L., Weiss, R. F., Smethie, W. M., Warner, M. J., 1992. Thermocline and intermediate water communication between the South Atlantic and Indian Oceans. Journal of Geophysical Research: Oceans 97 (C5), 7223–7240.

Groeskamp, S., Abernathey, R. P., Klocker, A., 2016. Water mass transformation by cabbeling and thermobaricity. Geophysical Research Letters 43 (20), 835–10.

Groeskamp, S., Sloyan, B. M., Zika, J. D., McDougall, T. J., 2017. Mixing inferred from an ocean climatology and surface fluxes. Journal of Physical Oceanography.

Held, I. M., Soden, B. J., 2006. Robust responses of the hydrological cycle to global warming. Journal of Climate 19 (21), 5686–5699.

Huang, R. X., 1993. Real Freshwater Flux as a natural Boundary Condition for the Salinity Balance and Thermohaline Circulation Forced by Evaporation and Precipitation. Journal of Physical Oceanography 23.

Huffman, G. J., Adler, R. F., Arkin, P., Chang, A., Ferraro, R., Gruber, A., Janowiak, J., McNab, A., Rudolf, B., Schneider, U., 2 2010. The Global Precipitation Climatology Project (GPCP) Combined Precipitation Dataset. Bulletin of the American Meteorological Society 78 (1), 5–20.

Hurrell, J. W., 1 1995. Decadal trends in the North Atlantic oscillation. Science.

Johnson, B. K., Bryan, F. O., Grodsky, S. A., Carton, J. A., 7 2016. Climatological Annual Cycle of the Salinity Budgets of the Subtropical Maxima. Journal of Physical Oceanography, 15–0202.

Johnson, G. C., Kearney, K. A., 11 2009. Ocean climate change fingerprints attenuated by salt fingering? Geophysical Research Letters 36 (21), L21603.

Klein, P., Lapeyre, G., 1 2009. The Oceanic Vertical Pump Induced by Mesoscale and Submesoscale Turbulence. Annual Review of Marine Science 1 (1), 351–375.

Klocker, A., Abernathey, R. P., 1 2014. Global patterns of mesoscale eddy properties and diffusivities. Journal of Physical Oceanography.

Lagerloef, G., 2 2013. Aquarius Salinity Validation Analysis; Data Version 2.0 Tech. Rep. Aquarius SAC/D.

Lagerloef, G., Colomb, F. R., Le Vine, D., Wentz, F., Yueh, S., Ruf, C., Lilly, J., Gunn, J., Chao, Y., deCharon, A., others, 2008. The Aquarius/SAC-D mission: Designed to meet the salinity remote-sensing challenge. Oceanography 21 (1), 68–81.

Lee, M.-M., Nurser, A. J. G., Coward, A. C., De Cuevas, B. A., 2009. Effective Eddy Diffusivities Inferred from a Point Release Tracer in an Eddy-Resolving Ocean Model. Journal of Physical Oceanography 39 (4), 894–914.

Lindstrom, E., Bryan, F., Schmitt, R., 1 2015. SPURS: Salinity Processes in the Upper-ocean Regional Study - The North Atlantic Experiment. Oceanography.

Lumpkin, R., Johnson, G. C., 2013. Global ocean surface velocities from drifters: Mean, variance, El Nino-Southern Oscillation response, and seasonal cycle. Journal of Geophysical Research: Oceans 118 (6), 2992–3006.

Mahadevan, A., D'Asaro, E., Lee, C., Perry, M. J., 7 2012. Eddy-Driven Stratification Initiates North Atlantic Spring Phytoplankton Blooms. Science 337 (6090), 54–58.

Marshall, J., Adcroft, A., Hill, C., Perelman, L., Heisey, C., 3 1997. A finite-volume, incompressible Navier Stokes model for studies of the ocean on parallel computers. Journal of Geophysical Research: Oceans (1978–2012) 102 (C3), 5753–5766.

Marshall, J., Jamous, D., Nilsson, J., 4 1999. Reconciling thermodynamic and dynamic methods of computation of water-mass transformation rates. Deep Sea Research Part I: Oceanographic Research Papers 46 (4), 545–572.

Marshall, J., Scott, J. R., Romanou, A., Kelley, M., Leboissetier, A., 2017. The dependence of the ocean's MOC on mesoscale eddy diffusivities: A model study. Ocean Modelling 111, 1–8.

Marshall, J., Shuckburgh, E., Jones, H., Hill, C., 2006. Estimates and Implications of Surface Eddy Diffusivity in the Southern Ocean Derived from Tracer Transport. Journal of Physical Oceanography 36 (9), 1806–1821.

Marshall, J., Speer, K., 2012. Closure of the meridional overturning circulation through Southern Ocean upwelling. Nature Geoscience 5 (3), 171–180.

Maximenko, N., Niiler, P., Rio, M. H., Melnichenko, O., Centurioni, L., Chambers, D., Zlotnicki, V., Galperin, B., 2009. Mean dynamic topography of the ocean derived from satellite and drifting buoy data using three different techniques. Journal of Atmospheric and Oceanic Technology 26 (9), 1910–1919.

McCann, M. P., Semtner, A. J., Chervin, R. M., 1994. Transports and budgets of volume, heat, and salt from a global eddy-resolving ocean model. Climate Dynamics 10, 59–80.

Melet, A., Legg, S., Hallberg, R., 2016. Climatic impacts of parameterized local and remote tidal mixing. Journal of Climate, 151221155323005.

Nakamura, N., 1 1996. Two-dimensional mixing, edge formation, and permeability diagnosed in an area coordinate. Journal of the Atmospheric Sciences 53 (11), 1524–1537.

Nakano, H., Ishii, M., Rodgers, K. B., Tsujino, H., Yamanaka, G., 10 2015. Anthropogenic CO 2 uptake, transport, storage, and dynamical controls in the ocean imposed by the meridional overturning circulation: A modeling study. Global Biogeochemical Cycles 29 (10), 1706–1724.

O'Connor, B. M., Fine, R. A., Olson, D. B., 1 2005. A global comparison of subtropical underwater formation rates. Deep Sea Research Part I: Oceanographic Research Papers.

Olbers, D., Willebrand, J., Eden, C., 2012. Ocean dynamics. Springer Science & Business Media.

Osborn, T. R., Cox, C. S., 1972. Oceanic fine structure. Geophysical Fluid Dynamics 3 (1), 321–345.

Pachauri, R. K., Allen, M. R., Barros, V. R., Broome, J., Cramer, W., Christ, R., Church, J. A., Clarke, L., Dahe, Q., Dasgupta, P., others, 2014. Climate change 2014: synthesis report. Contribution of Working Groups I, II and III to the fifth assessment report of the Intergovernmental Panel on Climate Change. IPCC.

Ponte, R. M., Vinogradova, N. T., 7 2016. An assessment of basic processes controlling mean surface salinity over the global ocean. Geophysical research letters 43 (13), 7052–7058.

Qu, T., Gao, S., Fukumori, I., 2011. What governs the North Atlantic salinity maximum in a global GCM? Geophysical Research Letters 38 (7), 1–6.

Reverdin, G., Kestenare, E., Frankignoul, C., Delcroix, T., 5 2007. Surface salinity in the Atlantic Ocean (30°S–50°N). Progress in Oceanography 73 (3-4), 311–340.

Reynolds, R. W., Rayner, N. A., Smith, T. M., Stokes, D. C., Wang, W., 2002. An improved in situ and satellite SST analysis for climate. Journal of climate 15 (13), 1609–1625.

Roach, A. T., Aagaard, K., Pease, C. H., Salo, S. A., Weingartner, T., Pavlov, V., Kulakov, M., 1995. Direct measurements of transport and water properties through the Bering Strait. Journal of Geophysical Research: Oceans 100 (C9), 18443–18457.

Roemmich, D., Boebel, O., Desaubies, Y., Freeland, H., King, B., LeTraon, P.-Y., Molinari, R., Owens, B., Riser, S., Send, U., others, 1999. ARGO: the global array of profiling floats. CLIVAR Exchanges 13 (4 (3)), 4–5.

Roemmich, D., Church, J., Gilson, J., Monselesan, D., Sutton, P., Wijffels, S., 2 2015. Unabated planetary warming and its ocean structure since 2006. Nature Climate Change 5 (3), 240–245.

Rypina, I. I., Kamenkovich, I., Berloff, P. S., Pratt, L. J., 2012. Eddy-Induced Particle Dispersion in the Near-Surface North Atlantic. Journal of Physical Oceanography 42 (12), 2206–2228.

Schanze, J. J., Schmitt, R. W., Yu, L. L., 1 2010. The global oceanic freshwater cycle: A state-of-the-art quantification. Journal of Marine Research 68 (3), 569–595.

Schmidtko, S., Johnson, G. C., Lyman, J. M., 1 2013. MIMOC: A global monthly isopycnal upper-ocean climatology with mixed layers. Journal of Geophysical Research: Oceans, 1–15.

Schmitt, R. W., 1 1994. Double Diffusion in Oceanography. Annual Review of Fluid Mechanics 26 (1), 255–285.

Schmitt, R. W., 7 1995. The ocean component of the global water cycle. Reviews of Geophysics 33 (S2), 1395–1409.

Schmitt, R. W., 1 2008. Salinity and the Global Water Cycle. Oceanography 21 (1).

Schmitt, R. W., Blair, A., 2015. A river of salt. Oceanography.

Schott, F. A., Mccreary, J. P., Johnson, G. C., 1 2004. Shallow overturning circulations of the tropical -subtropical oceans. Earth's Climate 147, 261–304.

Sebille, E., Sprintall, J., Schwarzkopf, F. U., Sen Gupta, A., Santoso, A., England, M. H., Biastoch, A., Böning, C. W., 2014. Pacific-to-Indian Ocean connectivity: Tasman leakage, Indonesian Throughflow, and the role of ENSO. Journal of Geophysical Research: Oceans 119 (2), 1365–1382.

Shchepetkin, A. F., McWilliams, J. C., 1 2009. Computational kernel algorithms for fine-scale, multi-process, long-time oceanic simulations. Handbook of Numerical Analysis 14.

Skliris, N., Zika, J. D., Nurser, G., Josey, S. A., Marsh, R., 2016. Global water cycle amplifying at less than the Clausius-Clapeyron rate. Scientific Reports 6, 38752.

Stammer, D., 1998. On Eddy Characteristics, Eddy Transports, and Mean Flow Properties. Journal of Physical Oceanography 28 (4), 727–739.

Thomas, L. N., Lee, C. M., Yoshikawa, Y., 1 2010. The Subpolar Front of the Japan/East Sea. Part II: Inverse Method for Determining the Frontal Vertical Circulation. J Phys Oceanogr 40 (1), 3–25.

Thomas, L. N., Tandon, A., Mahadevan, A., 1 2008. Ocean Modeling in an Eddying Regime. Ocean modeling in an . . . , Ch. Submesosca.

Tréguier, A.-M., Deshayes, J., Sommer, J. L., Lique, C., Madec, G., Penduff, T., Molines, J.-M., Barnier, B., Bourdallé-Badie, R., Talandier, C., 2014. Meridional transport of salt in the global ocean from an eddy-resolving model. Ocean Science 10 (2), 243–255.

Uppala, S. M., Kallberg, P. W., Simmons, A. J., Andrae, U., Bechtold, V. D., Fiorino, M., Gibson, J. K., Haseler, J., Hernandez, A., Kelly, G. A., Li, X., Onogi, K., Saarinen, S., Sokka, N., Allan, R. P., Andersson, E., Arpe, K., Balmaseda, M. A., Beljaars, A. C. M., Van De Berg, L., Bidlot, J., Bormann, N., Caires, S., Chevallier, F., Dethof, A., Dragosavac, M., Fisher, M., Fuentes, M., Hagemann, S., Holm, E., Hoskins, B. J., Isaksen, L., Janssen, P. A. E. M., Jenne, R., McNally, A. P., Mahfouf, J. F., Morcrette, J. J., Rayner, N. A., Saunders, R. W., Simon, P., Sterl, A., Trenberth, K. E., Untch, A., Vasiljevic, D., Viterbo, P., Woollen, J., 2005. The ERA-40 re-analysis. Quarterly Journal of the Royal Meteorological Society 131 (612), 2961–3012.

Vinogradova, N. T., Ponte, R. M., 6 2013. Clarifying the link between surface salinity and freshwater fluxes on monthly to interannual time scales. Journal of Geophysical Research: Oceans 118 (6), 3190–3201.

Walin, G., 4 1977. A theoretical framework for the description of estuaries. Tellus 29 (2), 128–136.

Wallace, J. M., Hobbs, P. V., 2006. Atmospheric science: an introductory survey. Vol. 92. Academic press.

Worthington, L. V., 1 1976. On the North Atlantic Circulation. The Johns Hopkins Oceanographic Studies 6, 85–91.

Wüst, G., 1 1936. Oberflächensalzgehalt, Verdunstung und Niederschlag auf dem Weltmeere nebst Bemerkungen zum Wasserhaushalt der Erde. Länderkundliche Forschung Festschrif, 347–359.

Yeager, S. G., Large, W. G., 2007. Observational Evidence of Winter Spice Injection. Journal of Physical Oceanography 37 (12), 2895–2919.

Yu, L., Jin, X., Weller, R. A., 1 2008. Multidecade Global Flux Datasets from the Objectively Analyzed Air-sea Fluxes (OAFlux) Project: Latent and sensible heat fluxes, ocean evaporation, and related surface meteorological variables. OAFlux Project Technical Report. OA-2008-01, 64pp. (2008).

Zaucker, F., Broecker, W. S., 1992. The influence of atmospheric moisture transport on the fresh water balance of the Atlantic drainage basin: General circulation model simulations and observations. Journal of Geophysical Research: Atmospheres 97 (D3), 2765–2773.

Zhang, J., Schmitt, R. W., Huang, R. X., Zhang, J., Schmitt, R. W., Huang, R. X., 4 1998. Sensitivity of the GFDL Modular Ocean Model to Parameterization of Double-Diffusive Processes*. Journal of Physical Oceanography 28 (4), 589–605.

Appendix A

Supplement to Chapter 3

A.1 Reset procedure

Due to the nature of the presented experiments, which do not simulate key processes like surface forcing and all vertical processes a steady state will never be reached in the TFR/K_{eff}. The mixing will eventually just destroy all local maxima and completely homogenize the surface fields. In order to maintain a realistic "quasi-constant" background SSS field the tracer fields have to be reset in regular intervals. Each reset to the smooth initial conditions causes a distinct spike in both TFR and K_{eff}, which represents the adjustment phase in which increased variance is created by stirring the smooth initial conditions until the small scale diffusion limits the variance and the change in TFR and K_{eff} represents the temporal changes in eddy stirring. The aforementioned adjustment phase is unrealistic and has to be removed (we cut the first 2 months in our experiments, leaving a gap in the data record. We compute two different tracer outputs that are reset at shifted intervals and then averaged, to create a continuous time series of TFR and K_{eff} for each salinity S_0. Shifting them exactly half of the reset period also ensures that any residual drift from the reset would be averaged out. Several considerations are influencing the choice of reset period:

- The missing data might still slightly bias the results at the time of reset. It is vital to choose an odd number of months as the interval length, to ensure that the possible effect of the reset is occurring at different months of the year each time, which should be averaged out when analyzing the seasonal cycle.
- The mean position and area of the SSS-max features have to remain within a realistic range, which limits the maximal length of the reset interval to 9-11 months. After that for instance the NA SSS-max get slowly advected into the equatorial current system and the velocity fluctuations acting on the reference isohaline are not representative of the subtropics anymore.
- The reset interval has to be chosen so that the reference salinity does not get eroded too far, which specifically in the SI is a problem in reset periods over 9 months
- Since the adjustment phase removes 2 months from the record, the reset period is chosen as long as possibly allowed by the above criteria, to ensure a maximum of data

points are derived from both tracer records.

We hence decided on a reset period of 9 months, with the second tracer field initiated again after 4.5 months and then reset in 9 months intervals like the first.

A.2 Error due to reset procedure

To estimate the influence of the chosen reset interval we conducted several quality control (QC) experiments with varying reset intervals (7/9/11/13 months), all reset to the mean SSS initial conditions. Results for $TFR_{mean}/K_{eff,mean}$ are calculated identically to the presented data for mean, seasonal and interannual. We estimate the RMSE as:

$$RMSE = \sqrt{\langle \langle x \rangle_{(ex)} - x_{t,ex} \rangle_{(t,ex)}} \tag{A.1}$$

Where $\langle . \rangle_{(ex)}$is the average over all QC experiments without averaging in time and $\langle . \rangle_{(t,ex)}$ is the average over time and experiments. Figure A1 shows the estimated error split into the various temporal estimates. Results discussed as significant exceed these error estimates and are assumed not to be strongly dependent on the reset procedure .

A.3 Combined experiment

In order to evaluate the effect of the interplay between temporally evolving velocities and SSS fields we created several "combined" experiments. As stated above they are not separate model experiments, but instead combinations of the single experiments, aiming to give the most realistic representation of the TFR for a climatological season or interannual variability. We split the existing experiments into chunks and stitch them together in order of their initial conditions. For the 'annual combined' from January 2000 until December 2000 the values are taken from the 'ECCO 2000' experiment (see Table 3.1) and from January 2001 until December 2001 the values from the 'ECCO 2001' experiment (see Table 3.1) are inserted. This is repeated for all annual experiments. We present two 'annual combined' records to cover the whole time frame of the altimetry record. From 1993-2011 we use annually averaged surface fields from ECCO as intial conditions and from 2006 to 2014 we use Argo data (details in Tab. 3.1).

The 'monthly combined' experiment is created by substituting each month in the record with data from the experiment with corresponding climatological initial conditions (see Figure A2). Note that these are climatological monthly initial conditions, meaning the initial conditions are the same for each e.g. January. The velocities however vary interannually as in all other experiments.

A.4 Boundary violation

The water mass framework is well suited for the study of SSS-maxima due to their appearance as local maxima in the SSS fields. One however has to define regional domains in order to not

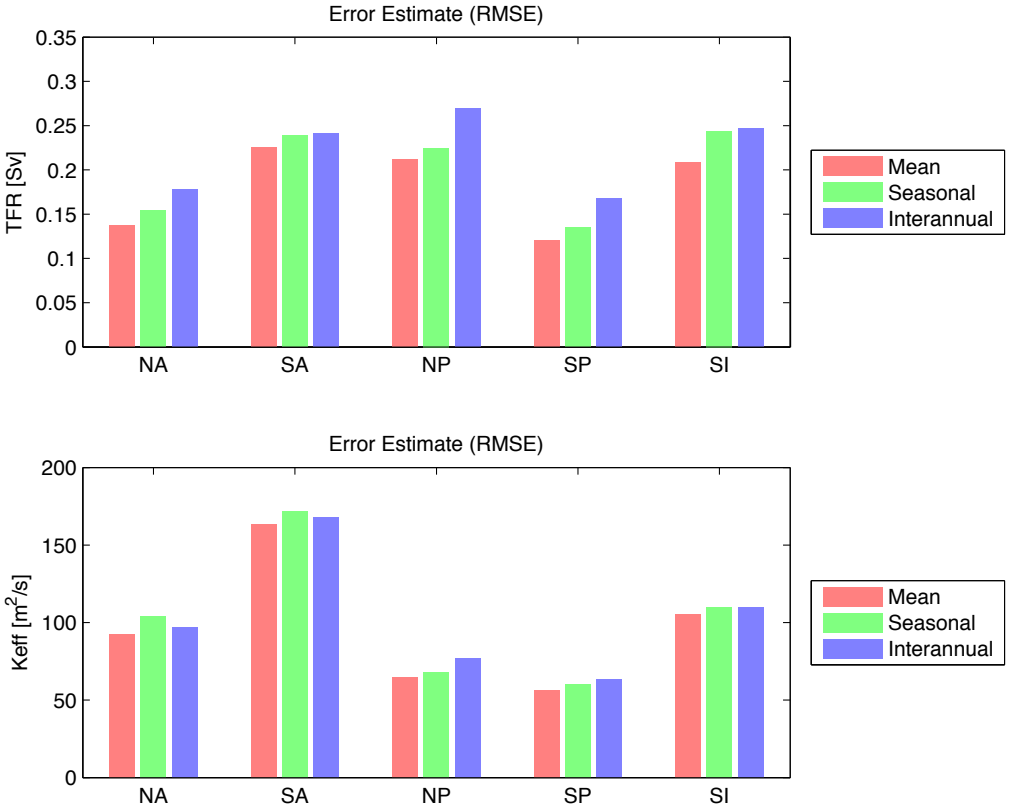

Figure A.1: Root mean square error due to reset procedure. Values are shown for the respective basins and the various time frames considered (color see legend). For details see text.

lump all maxima together globally, making the interpretation of local differences impossible. Depending on the basin the definition of this local domain can be complicated as one has to take good care that the isolines of interest neither leave the box at any time nor other features enter the domain. Our domains are chosen to guarantee both of these aspects for the reference salinity. Due to the regional setup this can mean that even isolines as little away as 0.2 PSU violate this criterion. This is especially critical in basins with low lateral SSS gradients and secondary local maxima in SSS like the SI and NP. In fact in the SI we were not able to completely keep the reference isohaline in the box without making the box unreasonably large, reaching into the SA and SP. Hence we decided to allow a possible but likely small leakage of the reference isohaline on the South coast of Australia. Values at isohalines larger than the reference salinity are not affected by the boundary violation but might be biased due to the fact that the highest salinity values will simply disappear over the reset time, as they diffuse outwards. Thus we urge the reader to interpret the values only on the reference salinity, for which extensive testing has excluded above issues.

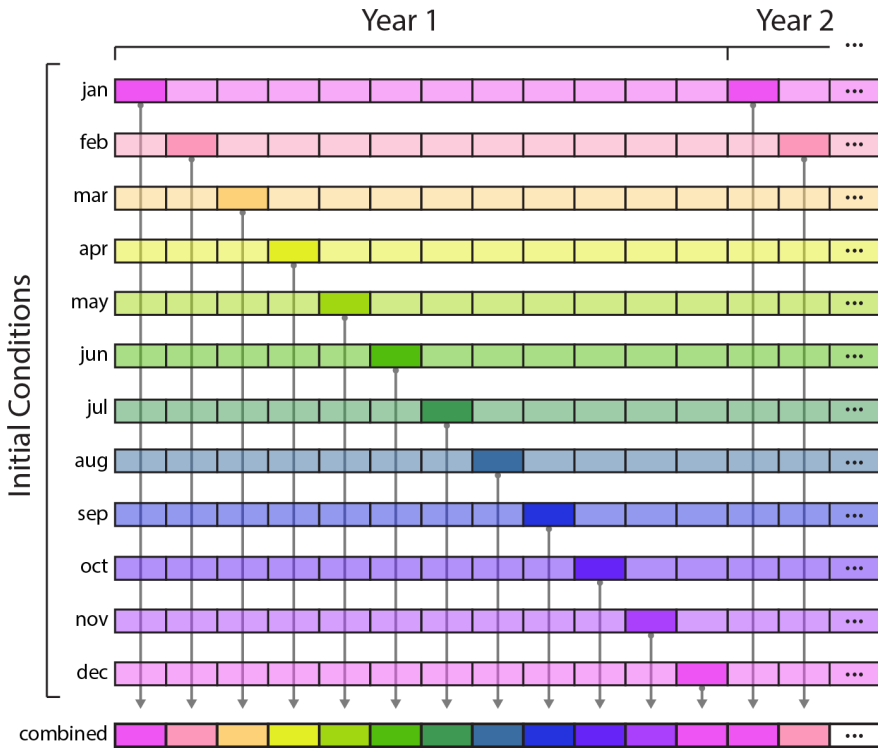

Figure A.2: Schematic for the construction of the 'combined monthly' experiment. Each colored row is an experiment with quasi-constant intial conditions (see Table 3.1 and text for details). Each box represents a month in the full time record (extended for multiple years indicated by the dots on the right). The combined experiment is constructed by concatenating the time series from the respective experiment for each month(dark boxes).

Appendix B

Supplement to Chapter 4

B.1 Uncertainty of K_{min}

The root mean square error between both shifted tracers for each initial condition, defined as

$$RMSE_{tr,q0} = \sqrt{\langle (K_{OC}\{tr, q0\} - \langle K_{OC} \rangle_{tr})^2 \rangle_{t,q0}} \tag{B.1}$$

is minor compared to the mean diffusivities. The $RMSE_{tr,q0}$ is mostly smaller than 2% of the local mean of K_{OC}. We quantify the uncertainty of K_{min} similar to Eq. B.1 as

$$RMSE = \sqrt{\langle (\langle K_{OC,q0} \rangle_{tr} - \langle K_{OC} \rangle_{tr,q0})^2 \rangle_t} \tag{B.2}$$

The estimated uncertainty is smaller then 10% almost everywhere (Fig. B.1). Within the regions we focus on, the deviation between the single tracers is small compared to the spread between the initial conditions. The angled brackets represent a geometric mean over the dimension in subscript (see below for a discussion of the usage of the geometric mean for diffusivities). Generally the results presented in this dataset show robust temporal variability. Time series of each initial condition ($q0$) show very similar temporal evolution, indicating that the variability is indeed caused by the velocity field characteristics (Fig. B.2). Furthermore by comparing the Numerator and Denominator of K_OC is becomes evident, that the Numerator, representing the enhanced 'roughness' or tracer gradient variance dominates the diffusivity signal and particularly the large peaks during strong ENSO events (Fig B.3)

B.2 Validity of Osborn-Cox relationship

The validity of a diffusive closure for the Reynolds tracer fluxes relies on the assumption that the creation of tracer variance is locally balanced by the dissipation of tracer variance. This is equivalent to the statement that the length scale of particle displacement over which the properties of such particle are not changed (the mixing length L_{mix}) is small compared to the curvature scale L_{curv} of the tracer field:

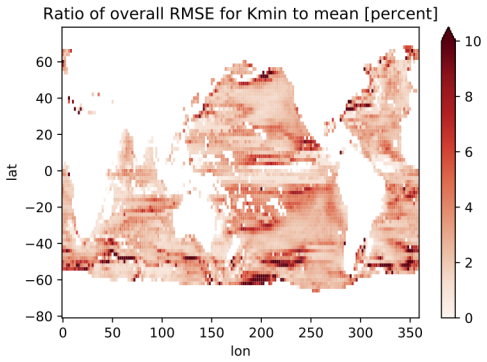

Figure B.1: Estimated uncertainty for K_{min} in m^2/s. The uncertainty stems mostly from the difference between the initial conditions, due to the anisotropy of the diffusivity tensor (see text for details).

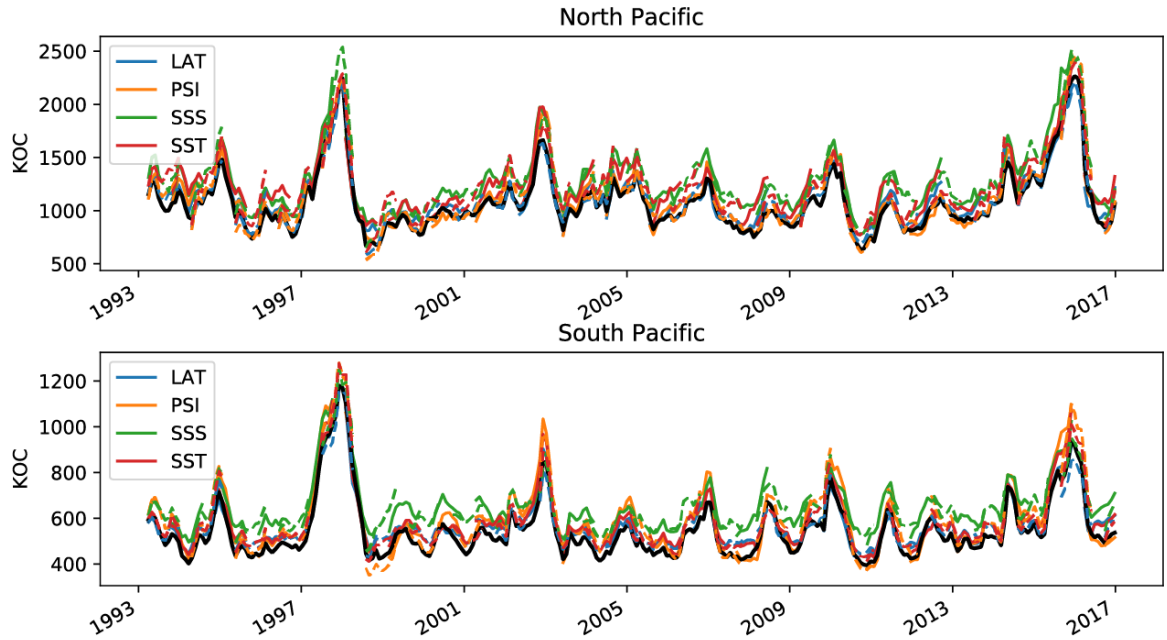

Figure B.2: Temporal evolution of $K_{OC,q}$ (colors) and $K_{min}(black)$. Both tracers with different reset intervals are shown as solid and dotted line in the same color. Temporal evolution of the averaged diffusivity derived from various initial condition and the combined estimate of K_{min}. Values are averaged over the North (upper) and South (lower) Pacific boxes shown in Figure 4.2.

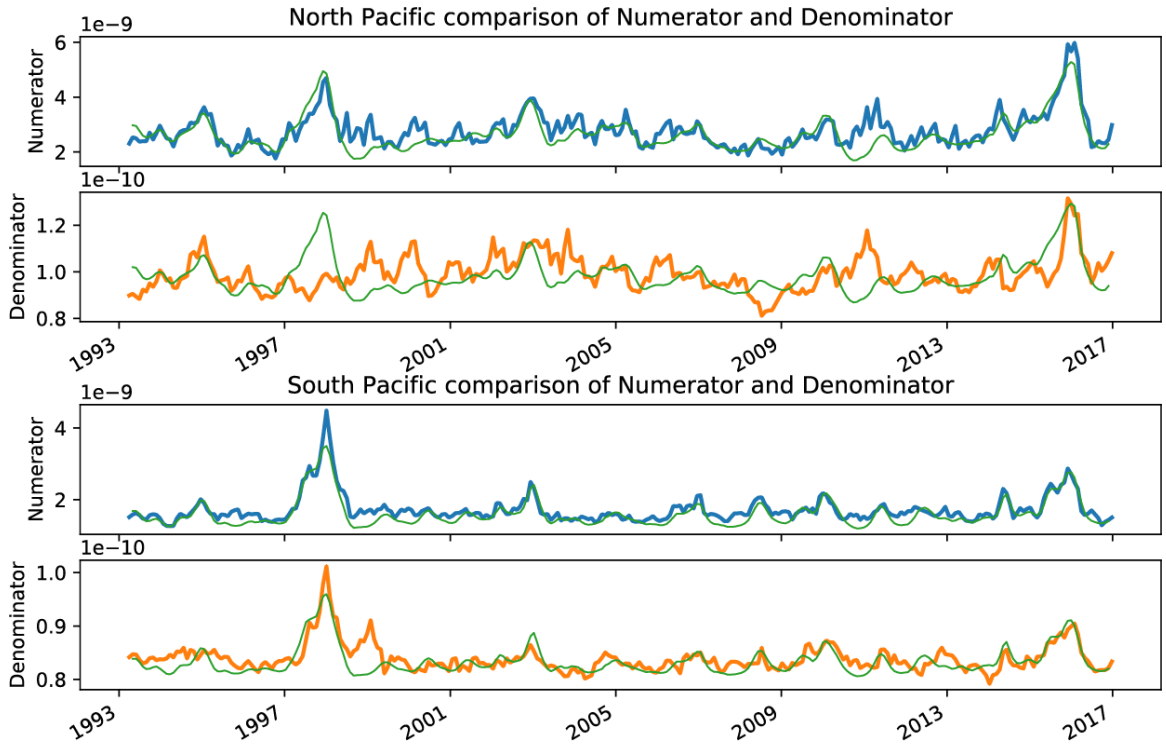

Figure B.3: Comparison of Numerator and Denominator for $K_{OC,LAT}$. Upper/Lower panel shows North/South Pacific values of Numerator(blue) and Denomniator(orange) averaged over the same box as in Figure 4.2. The scaled $K_{OC,LAT}$ (green) is shown for reference. Note the different scales for the Numerator and Denominator, underlining the dominance of the Numerator for the temporal evolution, particularly with respect to the correlation with ENSO.

$$L_{curv} = \frac{|\nabla \overline{c}|}{|\nabla^2 \overline{c}|} \tag{B.3}$$

Above c is an arbitrary tracer field and primes and overbars indicate fluctuations and mean of a Reynolds average. Physically L_{curv} can be understood as the length scale over which the local gradient of the field is representative. If $l_{mix} >> L_{curv}$ the mixing process becomes 'non-local' with respect to the averaging scale indicated by the overbars (which can be in either time, space or both). Hence we define a criterion for the validity of the Osborn-Cox method as cr:

$$1 >> cr = \frac{L_{mix}}{L_{curv}} = \frac{\sqrt{\frac{(c')^2}{2}}|\nabla^2 \overline{c}|}{|\nabla \overline{c}|^2} \tag{B.4}$$

This is equivalent to what is derived by Olbers et al. (2012) $1 >> cr = \frac{D}{\sqrt{\overline{\phi_2}}}$ (after the correction of two type errors). This criterion can be calculated as at every location and time step. In this study we exclude diffusivity values from the analysis, where $\langle cr \rangle_t > 1$.